Space Science Reviews (2022) 218:32
https://doi.org/10.1007/s11214-022-00906-2

# Observations and Modeling of Martian Auroras

**S.A. Haider[1] · K.K. Mahajan[2,3] · S.W. Bougher[4] · N.M. Schneider[5] · J. Deighan[5] · S.K. Jain[5] · J.C. Gérard[6]**

Received: 30 September 2020 / Accepted: 9 May 2022 / Published online: 24 May 2022


**Abstract**
Observations of planetary auroras form a new area of planetary exploration from space, especially for nonmagnetic planets since various kinds of auroras like Discrete, Proton and Diffuse auroras have been observed at Mars. We review the latest results of Martian auroras obtained by the instruments (1) SPICAM (Spectroscopy for the Investigation of the Characteristics of the Atmosphere of Mars) aboard Mars Express (MEX) and (2) IUVS (the Imaging Ultraviolet Spectrograph) on MAVEN (the Mars Atmosphere and Volatile Evolution mission). The MARSIS instrument (the Mars Advanced Radar for the Subsurface and Ionosphere Sounding) on MEX, in addition, exhibited strong ionizations in some electron density profiles, thus providing further evidence for the existence of Martian auroras. We review these MARSIS observations as well. In addition, we review various models of Martian auroras.

## 1 Introduction

In our solar system, the Sun is the primary source of energy, which creates as well as dictates changes in the atmospheres and ionospheres of various planets. The sun continuously emits electromagnetic and particle radiation and Fig. 1 depicts a schematic of the planetary environment of Mars exhibiting: (1) incoming and outgoing solar radiation, (2) its atmosphere, (3) its ionosphere, (4) its mini-magnetosphere and (5) lines of Interplanetary Magnetic Field (IMF). Electromagnetic radiation (EM), Solar Wind, Coronal Mass Ejections (CME), Solar Energetic Particle (SEP), Solar Interaction Region (SIR), Corotating Interaction Region (CIR) and Energetic Neutral Atom (ENA) are the incoming radiation, which interact with the atmospheric gases of Mars. The mid and far infrared are the outgoing radiation. A budget that's out of balance between incoming and outgoing solar radiation can cause the temperature of the atmosphere to increase or decrease and eventually affect the climate of Mars.

✉ S.A. Haider

1 Planetary Sciences Division, Physical Research Laboratory, Ahmedabad, India

2 CSIR, National Physical Laboratory, New Delhi, India

3 Present address: C1/121, Janak Puri, New Delhi, India

4 Climate and Space Sciences and Engineering, University of Michigan, Ann Arbor, MI, USA

5 Laboratory for Atmospheric and Space Physics, University of Colorado at Boulder, Boulder, USA

6 LPAP, Universite de Liege, Liege, Belgium

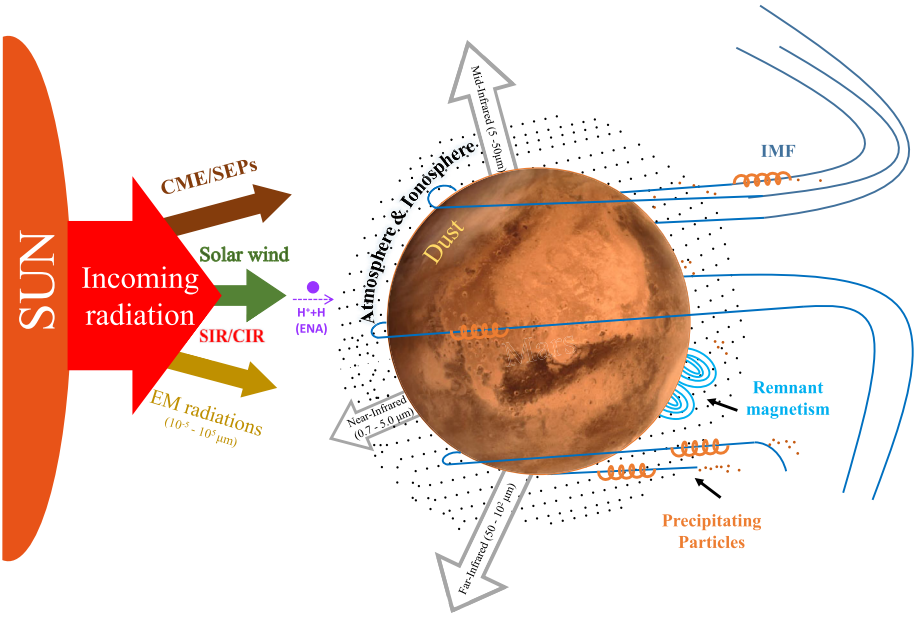


**Fig. 1** Schematic representations of incoming radiations from the sun and outgoing radiations from the Mars. The Electromagnetic (EM) and particle radiations (solar wind, CME/SEP and SIR/CIR) are emitting from the sun and contributing to the atmosphere/ionosphere of Mars. The near, mid and far infrared radiations are outgoing from the Mars. The Mars is covered by the dust as observed by Mangalyaan-1 (from Arya et al. 2015)

Mars is covered by dust as observed through Mars Color Camera (MCC) onboard Indian Mars Orbiter mission (Mangalyaan-1) (Arya et al. 2015).

Major external agents causing ionospheric disturbances are the solar X-ray flares, CMEs and SEPs. The solar EUV and X-ray radiations interact with the atmosphere of Mars and photoionize its gases (Krasnopolsky 1986; Fox 2004; Fox and Yeager 2009; Valeille et al. 2009; Haider et al. 2011; González-Galindo et al. 2013; Haider and Mahajan 2014; Bougher et al. 2017). The CMEs, SEPs and ENAs penetrate deep into the atmosphere and produce auroral emissions (Haider et al. 2009; Schneider et al. 2015, 2018; Deighan et al. 2018; Haider and Masoom 2019). The Martian aurora is also produced locally in the southern hemisphere without solar events in presence of strong crustal magnetic fields (Bertaux et al. 2005). The X-ray flares, CMEs and SEPs are emitted from the sun during disturbed condition. The solar X-ray flares are being monitored by Geostationary Operational Environment Satellite (GOES) since several decades (e.g. Bornmann et al. 1996). The SEP spectra have been observed by MAVEN in the energy range 20 keV to 200 keV (https://pds-ppi.igpp.ucla.edu).

Three kinds of auroras have been observed on Mars by the IUVS instrument aboard the MAVEN mission and these are: (1) discrete aurora, (2) proton aurora and (3) diffuse aurora (Schneider et al. 2015). The discrete auroras, first reported by Bertaux et al. (2005), are observed in the mini-magnetosphere of Mars and are formed due to precipitation of energetic electrons. The proton auroras are formed due to the precipitation of energetic protons and hydrogen atoms in the daytime atmosphere of Mars and were first reported by Deighan et al. (2018). The diffuse auroras are observed in the lower atmosphere of Mars due to

precipitation of SEP electrons or protons (Schneider et al. 2015, 2018; Haider and Masoom 2019). These auroras are not limited to the mini-magnetosphere of Mars but occur at mid-latitudes and span over all longitudes. In the sections that follow we shall review Mars' auroras, mechanisms for their formation and the modeling tools.

### 1.1 Objectives

Although several review papers on the ionosphere of Mars, and based upon the observations by Mariners 6, 7, and 9; Mars 2, 3, 4, and 6; Viking 1 and 2; Mars Global Surveyor (MGS) and MEX have appeared in the literature (e.g. Whitten and Colin 1974; Schunk and Nagy 1980; Cravens and Nagy 1983; Mahajan and Kar 1988; Kar 1996; Nagy et al. 2004; Withers 2009; Haider et al. 2011; Haider and Mahajan 2014), none of these covered the study of Mars' aurora. This happened due to two main reasons. Firstly, no spacecraft earlier to MEX successfully visited Mars with the right combination of instruments and an observing plan to detect the faint and small scale UV emissions. Secondly, until the late 2004, there was no consensus on the fact that auroral processes can also be active at Mars. In fact the first observation on the Martian aurora was reported in 2005 by Bertaux et al. (2005) from the SPICAM instrument aboard MEX. Furthermore, the richness of different types of auroras on Mars has only been realized through MAVEN/IUVS observations.

As mentioned above, the latest exploration of Mars has been executed by MAVEN which was launched on November 18, 2013 and reached Mars on September 21, 2014. The objectives of this mission were: (1) to explore the interactions of solar wind with the Mars magnetosphere and upper atmosphere, (2) to study the structure of the upper atmosphere and ionosphere and the processes controlling it and (3) to determine the escape rates from the upper atmosphere to space. The MAVEN mission carried eight science instruments and Jakosky et al. (2015) have recently reviewed these experiments. Bougher et al. (2017), from pre-MAVEN observations, reviewed the spatial and temporal variability of Mars' thermosphere and ionosphere as a benchmark for new MAVEN measurements. In this paper, we shall, for the first time, review Mars' aurora using MEX and MAVEN observations, as well as their modeling. We shall review modeled and experimental results of the various kinds of auroras that occurred in the lower and upper atmosphere of Mars, in the absence and as well as in the presence of strong crustal magnetic fields. A variety of mechanisms and theoretical models of Martian auroras will also be reviewed.

### 1.2 Applications to Future Mars Missions

Recently the spacecrafts Emirates Mars Mission (EMM), Mars global remote sensing Orbiter, Lander and small Rover (Tianwen-1) and Mars Perseverance Rover have reached Mars on 9, 10, and 18 February, 2021 respectively. The missions Rosalind Franklin Rover, Mangalyaan-2 (MOM-2) (https://www.isro.gov.in) and Martian Moons eXploration (MMX) are in the pipelines (www.digitaltrends.com). The EMM is studying the daily and seasonal weather cycles in the lower and upper atmosphere of Mars. It will also attempt to answer the scientific questions of why Mars' atmosphere is losing hydrogen and oxygen into space. The escape rates of these atoms will help to understand the formation of hot oxygen corona and ENAs in the exosphere of Mars. The ENAs are produced by charge exchange reactions between solar wind protons and hydrogen atoms (Galli et al. 2008; Milillo et al. 2009; Haider and Masoom 2019; Sakai et al. 2021). The hot oxygen corona is produced due to dissociative recombination of $O_2^+$ (Zhao and Tian 2015; Cravens et al. 2017). The $H_2O$ is confined to low altitudes where photo-dissociation and $HO_x$ chemistry produce $H_2$, which

diffuses into upper atmosphere, and gets destroyed there to produce hydrogen atoms. These hydrogen atoms then escape into space (Haberle et al. 2019; Stone et al. 2020)

Mars Perseverance Rover is a NASA mission, which via a Martian Sample Return will study the Martian astrobiology in an attempt to understand what environmental conditions existed at Mars in the past. The objective would be to have the rover collect sample of rocks, minerals, and other materials on Mars and return these to Earth. China also explored a suite of an orbiter, a Lander and a small rover on Mars. This mission can be used as a technological demonstration of the resources and the technology required for Mars Sample Returns. This mission is planned to occur in 2030. Rosalind Franklin Mars Rover is a joint mission of ESA and Russia. The objective of this mission is to search evidence of life on Mars during its course of about one year's operation. The launch window of this mission is scheduled for 20 September, 2022 and Rover will touch down the surface of Mars on 10 July, 2023. None of these missions is dedicated to atmosphere/ionosphere of Mars.

MOM-2 is an Indian Mars mission, which is currently planned to explore Mars during the years 2022–2024. The major aim of this mission is to study the interactions of solar wind with the upper atmosphere of Mars. It will also explore the structure of the upper atmosphere, ionosphere and their response to solar flares, CMEs, and SEPs during the solar maximum of solar cycle 25. In addition it will observe energetic particle flux, ENAs, aurora, magnetic field and interplanetary dust in the upper ionosphere of Mars during that epoch.

Japan is also planning to send a MMX mission to Mars' largest moon Phobos in 2024. It will land on Phobos, collect samples and observe the smaller moon Deimos. In addition' it will provide information about Mars' climate during flybys of these two moons. This spacecraft will send the samples back to Earth in 2029. The aim of this mission is to provide key information to answer the question "whether the Martian moons were captured from asteroids or these large bodies were detached from the planet".

Among the above mentioned six missions, the EMM and MOM-2 are fully devoted to studies related to solar wind interaction with the magnetosphere and ionosphere of Mars. These two missions will also study aurora, dust, magnetic field and the influence of solar flares, CMEs and SEPs on the upper atmosphere of Mars. In view of these forthcoming missions, a review paper on Mars' auroras, their observations, modelling and causative mechanisms is desirable. This review paper will serve as a benchmark, which can guide the design of future payloads for detecting visible auroras on Mars, similar to those observed on Earth.

It needs to be mentioned that visible auroras have not yet been detected on Mars. The species like $CO_2$, O and $N_2$ emit the characteristic colours of their respective line spectra at visible wavelength (Lilensten et al. 2015). The electron impact on $CO_2$ produces strong emissions at 412 nm and 434 nm in the blue colour. Atomic oxygen produces green and red colour emissions at wavelengths 557.7 nm and 630.0 nm respectively. The molecular nitrogen also produces blue colour auroral emissions at wavelength 428 nm. It is not clear whether these relevant transitions are sufficiently excited to create visible auroras or the available UV instrument is unable to distinguish these and thus needs to be redesigned.

### 1.3 Chapter Organization

The present review consists of nine chapters. The first chapter gives a general introduction on Mars' aurora. In the second chapter we review Vikings 1/2 and MAVEN measurements of neutral densities in the upper atmosphere of Mars. There are no measurements of densities in the lower atmosphere of Mars and therefore theoretical density profiles in the lower atmosphere of Mars are reported in this chapter. In chapters three, four, and five, we review the characteristics of discrete aurora, proton aurora and diffuse aurora respectively. As

mentioned earlier, these auroras have been observed by SPICAM and IUVS instruments at Mars. Chapter six describes the possible mechanisms of nighttime aurora. In chapter seven we review, in brief, two plasma and three auroral emission models, which have been used in the modeling of Martian auroras. These models are (1) Hybrid model, (2) Magneto-Hydro-Dynamics (MHD) Model, (3) Monte Carlo Method, (4) Analytical Yield Spectrum (AYS) approach, and (5) Boltzmann Kinetic Transport Model. Chapter eight discusses briefly Mars' auroras and compares the field lines configuration for diffuse and discrete auroras on Earth and Mars. These auroras have been observed on Mars and Earth in very different magnetic field lines structures. Finally chapter nine summarizes and concludes the present review.

## 2 Atmosphere of Mars

Kuiper (1952) were the first to report $CO_2$ abundance of $4.4 \times 10^5$ Dobson at Mars. Later Spinrad et al. (1963) discovered the presence of water vapor in the Martian atmosphere with column abundance of 10 μm. Soon after Kaplan et al. (1964) derived Martian surface pressure $\sim 25 \pm 15$ mbar from $CO_2$ abundance of $55 \pm 20 \times 10^5$ Dobson. These calculations were strongly supported by determination of the total pressure $\sim$ 4–6 mbar from Mariner 4 (Kliore et al. 1965). Kliore et al. further reported that $\sim$ 90% of the Martian atmosphere is formed from $80 \times 10^5$ Dobson of $CO_2$, which produces surface pressure of $\sim$ 6 mbar. The CO was first detected by Kaplan et al. (1969) who deduced CO abundance of $5.6 \times 10^3$ Dobson. Young and Young (1977) also observed similar values of $5.6 \pm 0.5 \times 10^3$ Dobson. The densities of atomic hydrogen and oxygen were observed $\sim 3 \times 10^4$ cm$^{-3}$ (Anderson and Hord 1971) and $\sim 5 \times 10^8$ cm$^{-3}$ (Strickland et al. 1972), respectively. Barker (1972) and Carleton and Traub (1972) estimated $O_2$ abundance as $9.0 \pm 0.6 \times 10^3$ and $10.4 \pm 1.0 \times 10^3$ Dobson respectively.

In addition to above constituents, Methane has also been measured in the Martian atmosphere. Mumma et al. (2009) were the first to report methane abundance of $\sim$ 45 ppbv from Infrared Telescope during the summer of 2003 at Terra Sabae, Nilli Fossae and Syrtis Major. The seasonal and latitudinal variability of methane was observed by Planetary Fourier Spectrometer (PFS) and Thermal Emission Spectrometer (TES) onboard MEX and MGS respectively (Formisano et al. 2004; Marzo et al. 2008). At Curiosity Gale Crater landing site (4.5°S, 137°E), the PFS observed an increase of methane from $\sim$ 15 ppbv in fall to $\sim$ 30 ppbv in winter whereas TES trend was opposite (Fonti and Marzo 2010): $\sim$ 30 ppbv in fall and $\sim$ 5 ppbv in winter. However, Tunable Laser Spectrometer (TLS) on Curiosity rover did not detect atmospheric methane at Mars' Gale Crater (Webster et al. 2015). These measurements cover a span of 20 months. During this period, methane concentration climbed up to 7 ppbv. Before and after the spike, the measured concentration was at or below 0.7 ppbv. The atmosphere of Mars can be broadly divided into upper and lower atmosphere (e.g. Smith et al. 2017). We describe these two atmospheres in the sections that follow.

### 2.1 Upper Atmosphere of Mars

Mars' atmosphere above 100 km is designated as the upper atmosphere where molecular diffusion dominates (McElroy et al. 1976). First direct measurement of the upper atmosphere of Mars was made by neutral mass spectrometer on board Viking Landers 1/2 (Nier and McElroy 1977). Later, an accelerometer (e.g. Keating et al. 1998; Bougher et al. 2017) and radio occultation experiment (e.g. Hinson et al. 1999) on MGS provided large datasets of

atmospheric density at various locations. These observations confirmed that the atmosphere of Mars contains $CO_2$, $N_2$, Ar, CO, $O_2$, and NO with individual contribution to the total air density of about 95.5%, 2.7%, 1.5%, 0.4–1.4%, 0.17%, 0.008% respectively. The Viking Landers also carried a Retarding Potential Analyzer (RPA), which provided information on the major ion densities and plasma temperatures in the ionosphere up to an altitude of about 300 km (Hanson et al. 1977). On the surface, atmospheric pressure at Mars is about 6 mbar while temperature is 220 °K (Seiff and Kirk 1977). The atmosphere of Mars is quite dusty (e.g. Kahre et al. 2017). Data from Mars Exploration Rover showed that the size of the suspended dust particles is about 1.5 μm within the atmosphere (Lemmon et al. 2015).

The Neutral Gas Ion Mass Spectrometer (NGIMS) aboard MAVEN recently observed neutral composition profiles for the daytime as well as for the nighttime atmosphere of Mars (Mahaffy et al. 2015; Elrod et al. 2017). In Fig. 2 we have plotted sample profiles of $CO_2$, Ar, $N_2$, CO, O, and He as observed by MAVEN on 10, 14, and 17 September, 2017, when the spacecraft was crossing from inbound (left panel plot) to outbound (right panel plot) orbits (https://pds-ppi.igpp.ucla.edu/search/view/?f=yes&id=pds://PPI/maven.insitu.calibrated). On 10 September 2017, MAVEN observed effect of a strong solar X-ray flare on Mars' thermosphere (Elrod et al. 2018). The neutral density profiles on 14 and 17 September 2017 shown in the figure were observed in the absence of the flare and thus during solar quiet conditions. MAVEN did not measure the neutral densities at altitudes below 150 km except during nine Deep Dip periods (e.g. Bougher et al. 2015b; Zurek et al. 2017; Stone et al. 2018). The neutral densities are nearly the same during inbound and outbound crossings of Mars atmosphere (However, Elrod et al. (2018) have reported that the outbound data of NGIMS are less reliable due to instrument limitation). These densities are decreasing exponentially with height, except for Helium as expected.

### 2.2 Lower Atmosphere of Mars

Mars' atmosphere below 100 km is designated as the lower-middle atmosphere (Smith et al. 2017). Here gases exist in a mixed state and eddy diffusion dominates. The lower atmosphere of Mars is characterized by strong coupling between pressure, temperature, neutral density and winds. MGS and MEX have observed temperature, pressure, and total density in the lower atmosphere of Mars with radio occultation experiment (Bougher et al. 2001; Hinson et al. 1999; Peter et al. 2014). Using stellar occultation at UV wavelengths, the vertical profiles of $CO_2$, $O_3$ and dust/clouds/aerosols were observed from SPICAM and IUVS instruments onboard MEX and MAVEN respectively (Montmessin et al. 2006; Lebonnois et al. 2006; Quémerais et al. 2006; Montmessin and Lefèvre 2013; Gröller et al. 2015, 2018). Recently Fedorova et al. (2018) studied the water vapor vertical distribution in the middle atmosphere of Mars during 2007 Global Dust Storm (GDS) using solar occultation measurements by the SPICAM spectrometer. They found that the $H_2O$ density increased by an order of magnitude between altitude 60–80 km in the presence of the dust storm. However, during "no dust storm conditions", Gröller et al. 2018) observed $CO_2$, $O_2$ and $O_3$ number densities and temperature profiles from IUVS instrument between altitude 20 km and 160 km at high latitude region from 80°S to 75°N. These profiles indicate strong longitudinal variability, which seems to be dominated by zonal waves. The Nadir and Occultation for Mars Discovery (NOMAD) and Atmospheric Chemistry Suite (ACS) spectrometers onboard ExoMars Trace Gas Orbiter (TGO) have observed mixing ratios of $H_2O$ and HDO simultaneously up to an altitude $\sim$ 80 km in the ultraviolet, visible and infrared wavelength channels (Vandaele et al. 2018; Korablev et al. 2018). The mixing ratio profiles of $H_2O$ and HDO have been reported in the presence and absence of 2018 GDS by Vandaele et al. (2019), who have found that the mixing ratios increase during the GDS due to atmospheric warming.

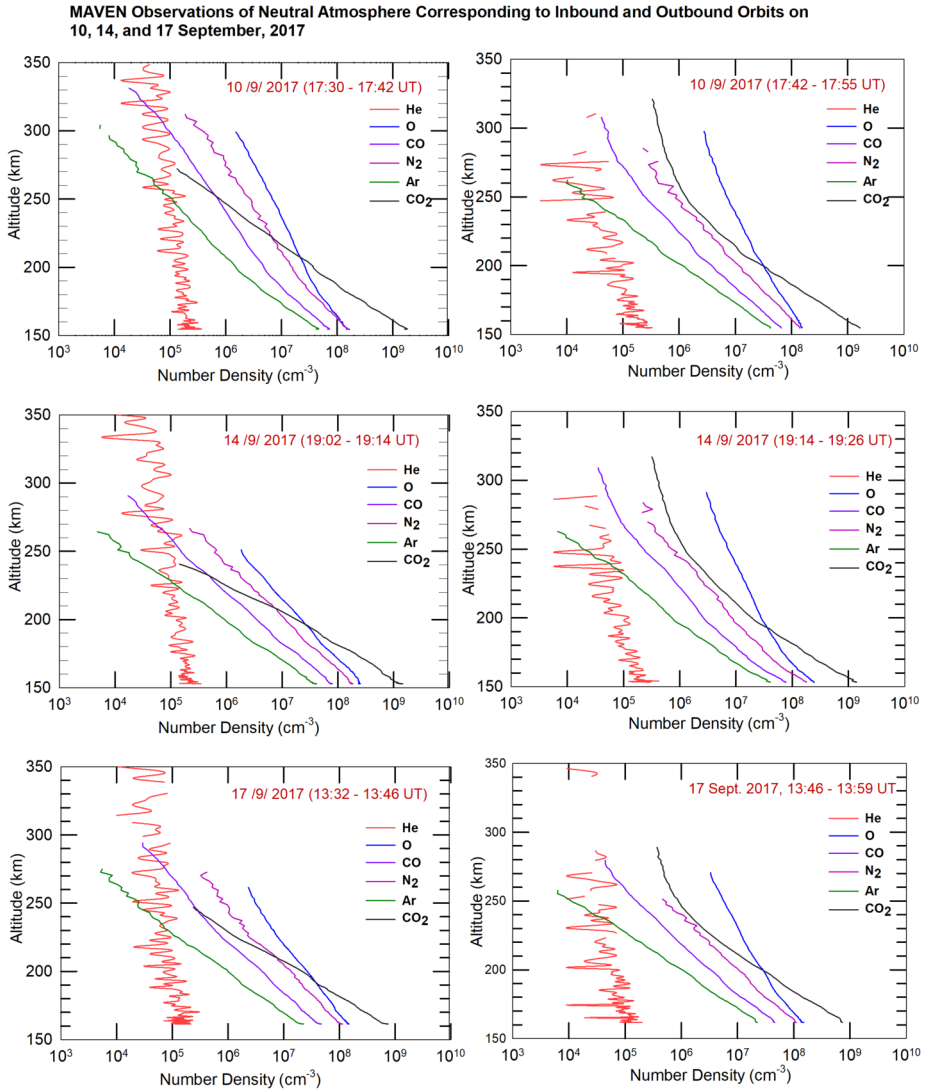


**Fig. 2** MAVEN observations of neutral densities in the upper atmosphere of Mars corresponding to inbound and outbound orbits on 10, 14, and 17 September, 2017 (https://pds-ppi.igpp.ucla.edu/search/view/?f=yes&id=pds://PPI/maven.insitu.calibrated)

## 2.3 Atmospheric Modeling

The photochemical models have predicted concentrations of $O_2$, $O_3$, $CO_2$, CO and other neutral species in the lower atmosphere of Mars (Belton and Hunten 1996; Parkinson and Hunten 1972; Rodrigo et al. 1990; Krasnopolsky 2003). Molina-Cuberos et al. (2002), Haider et al. (2011) and Haider and Mahajan (2014) have reported neutral model atmosphere of 12 gases ($CO_2$, $N_2$, Ar, $O_2$, CO, $H_2$, $H_2O$, O, $O_3$, NO, $NO_2$, and $HNO_3$) in the lower atmosphere of Mars. The density profiles of these gases are plotted in Fig. 3.

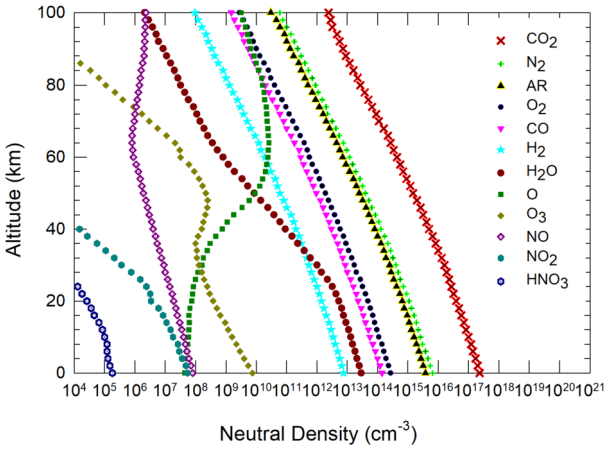


**Fig. 3** Neutral number density of $CO_2$, $N_2$, Ar, $O_2$, CO, $H_2O$, $H_2$, O, $O_3$, NO, $NO_2$, and $HNO_3$ in the troposphere of Mars (from Molina-Cuberos et al. 2002; Haider et al. 2011)

Mars Climate Database (MCD) provides meteorological parameters like air density, temperature, wind and mixing ratios using General Circulation Model (GCM) at different altitude, latitude and longitude in the Martian atmosphere (Millour et al. 2014) (website http://www-mars.lmd.jussieu.fr). This model has been developed for low, medium and high dust storm conditions also. The solar EUV, X-rays and particle radiations are highly variable and therefore the atmosphere of Mars also changes in response to these variations. The MCD model includes the effect of such variations. To include the effects of dust storms, warm and cold scenarios of Mars' atmosphere have been provided in this model: warm for their presence and cold for their absence. The climatology scenario is also provided in the model for minimum, medium and maximum solar activity conditions.

The Mars Global Ionosphere-Thermosphere Model (MGITM) also provides fundamental physical parameters like wind, gravity/planetary waves, thermal structure, compositional and dynamical structures of Mars atmosphere from ground to the exosphere (0–250 km) (Bougher et al. 2015a). In this model lower, middle and upper atmospheric processes are included and it is based on the formulations used in the Mars Thermosphere General Circulation Model (MTGCM) (Bougher et al. 2017) and the legacy NASA Ames Mars Global Circulation Model (MGCM) (e.g. Haberle et al. 1999). The MGITM model also captures dust storm, solar cycle, seasonal and diurnal variability in the upper atmosphere of Mars. The upper atmospheric measurements of temperature and densities made by Viking and MGS were compared with the MGITM neutral temperature and neutral – ion densities (Bougher et al. 2015a). In addition, the simulated lower atmospheric temperatures were also compared with the Mars Reconnaissance Orbiter and Mars Climate Sounder observations. MGITM has also been used to support and interpret MAVEN observations (Bougher et al. 2015b; Fang et al. 2019).

Recently Liu et al. (2018) have reported that the density of $CO_2$ increased in the upper atmosphere of Mars up to $\sim 200\%$ in response to dust increases in the lower atmosphere. These dust enhancements occurred during the period from 20 December 2016 to 30 May 2017 at Ls $\sim 320°$. This study is consistent with the earlier findings when the whole atmosphere of Mars expanded and rose up to $\sim 160$ km due to the influence of dust (Withers and Pratt 2013). In Fig. 4 we show $CO_2$ density profile obtained from MAVEN during the thermospheric warming associated with the planet-wide dust storm of 2018 (Elrod et al. 2020).

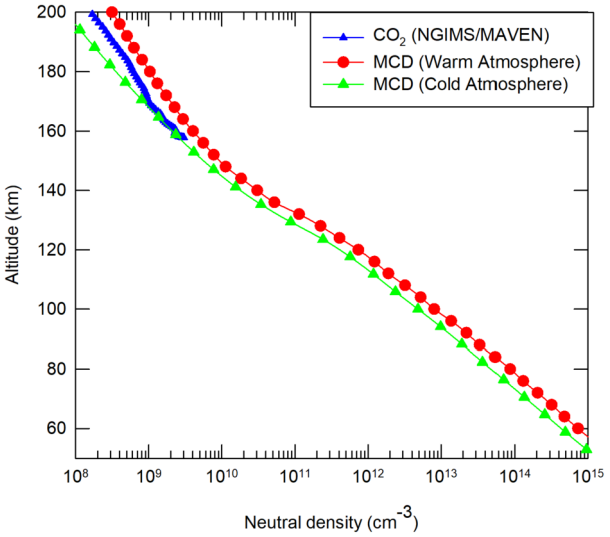


**Fig. 4** Altitude profiles of air densities estimated from MCD in the cold and warm atmosphere of Mars. The density of $CO_2$ during thermospheric warming observed by NGIMS/MAVEN during the global dust storm of 2018 is also plotted (from Millour et al. 2014; Elrod et al. 2020)

In this figure we have also plotted air density from MCD for cold and warm scenarios of Mars' atmosphere, calculated for the global dust storm of 2007, which occurred during the Martian Year (MY) 28. It can be noted that in the warm scenario the air density is larger than the cold scenario by a factor of $\sim$ 2–3.

## 3 Discrete Aurora on Mars

The magnetic field measurements from MGS have confirmed that Mars does not have a dipole magnetic field. However, it has mini-magnetospheres of intense crustal magnetic fields in the southern hemisphere (Acuña et al. 1998). The magnetic fields as high as 400 nT at 108–113 km altitude in the northern hemisphere and 1500 nT at 120–200 km altitude in the southern mini-magnetosphere were observed by MGS (Mitchell et al. 2001; Haider et al. 2010). The early Mars missions Mariners 6, 7 and 9 carried UV spectrometers but these missions did not prioritize the nighttime observations. The Viking 1/2, MGS, and Mars Odyssey did not carry UV instruments. Therefore, aurora was not observed during any of these missions.

### 3.1 SPICAM Observations of Discrete Aurora

The first limb observation of Mars' aurora was detected on 11 August 2004 during the orbit # 716 by the SPICAM UV spectrometer onboard MEX in the nighttime atmosphere at Solar Zenith Angle (SZA) 117.5° (Bertaux et al. 2005). It was unlike auroras observed at Earth and at other magnetic planets, which generally occur near the magnetic poles. It was a discrete aurora, which was produced in the mini-magnetosphere due to precipitating electrons along the magnetic field lines, connecting the surface to the solar wind (Mitchell et al. 2001; Krymskii et al. 2002). This aurora was observed at an apparent tangent altitude of 19 km, where the local time was nearly 21 hour and the longitude and latitude were 198.4° and 46.3°S respectively (Bertaux et al. 2005). Since discrete aurora is very spatially confined, their detections are not necessarily at the limb, so line-of-sight ambiguity hampers determination of accurate altitude and location.

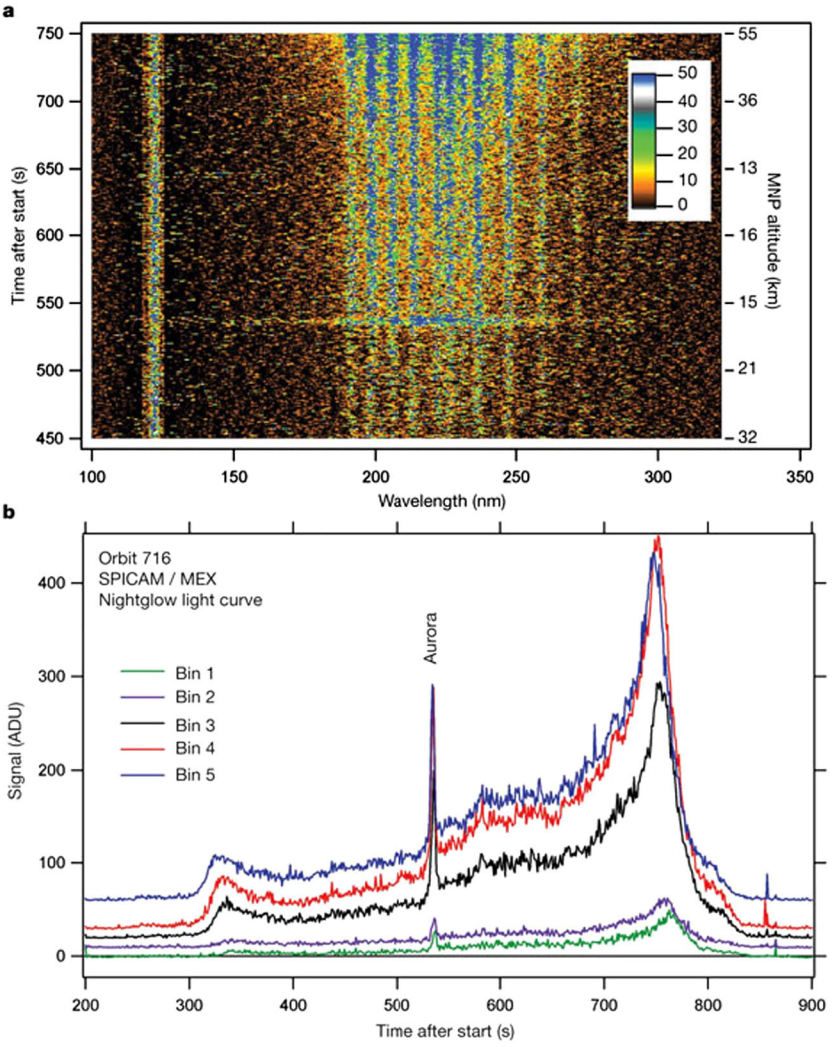


**Fig. 5** (**a**) Spectra recorded during the grazing limb observation between 450 to 750 seconds. Altitudes of the Mars Nearest Point (MNP) of the line of sight are indicated at the right. It contains H Lyman $\alpha$ emission at 121.6 nm and well structured band (190–270 nm) of NO. The intensity in ADU (Analogue Digital Units) per pixel is colour-coded. (**b**) Auroral peak is sharp and different from NO spectrum. Signal intensity in ADU for five bins (each averaged from 181–298 nm) as a function of time between 200 and 900 seconds are plotted in this figure (from Bertaux et al. 2005)

Figure 5a represents the nighttime limb observations of H Lyman $\alpha$ (121.6 nm) and NO bands (181–298 nm) carried out by SPICAM from 450 to 750 seconds at wavelength range 10 to 350 Å. In Fig. 5b the integrated auroral spectra over wavelength range of NO bands (181–298 nm) are shown for five spatial bins between 533 and 540 s. This layer is confined in the altitude range 60–80 km and is more intense at large southern latitudes (around time 750 s). These measurements were carried out in the mini-magnetosphere, where the field lines are nearly open and are vertical (Lundin et al. 2006; Mitchell et al. 2007). Leblanc et al. (2006) simulated emission rate of this aurora due to electron impact ionization. They

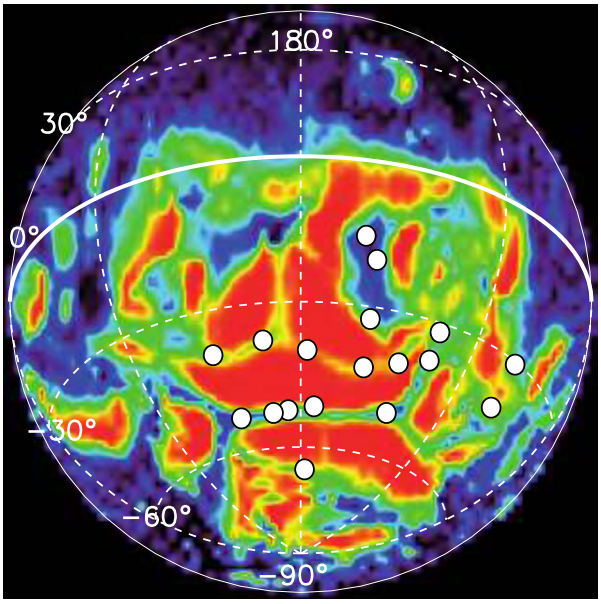


**Fig. 6** Locations of UV auroral detections by SPICAM (white dots) overlaid on a map of the statistical probability to find a closed magnetic field line at ∼ 400 km. The color scale ranges from 0% (dark blue) to 100% (red). SPICAM auroral detections were located in regions separating closed and open or semi-open magnetic field lines (from Gérard et al. 2015; Soret et al. 2016)

argued that the measured emissions by SPICAM UV spectrometer have been produced due to electrons of few tens of eV rather than by the electrons of above 100 eV.

Gérard et al. (2015) analyzed the database of the SPICAM nadir measurements between late January 2004 and March 2014 in the southern hemisphere. They searched for signatures of CO Cameron and $CO_2^+$ UV doublet auroral emissions. From a total of 113 nightside orbits with SPICAM pointing to the nadir in the region of residual magnetic field, only 9 night side orbits showed definitive auroral signatures, some with multiple detections along the orbital track, leading to a total of 18 detections. All events were located in the vicinity of the statistical boundary between open and closed field lines forming cusp structures (Fig. 6). The UV aurora was sometimes located pole ward or equator ward in the region of enhanced downward electron energy flux and separated by several tens of seconds. The auroral brightness did not show any proportionality with the electron flux at the spacecraft altitude. The mean latitudinal extent of the auroral arcs was 44 km and the absence of recurrence between successive orbits suggested that discrete aurorae are short-lived. They concluded that the Mars UV aurora is a localized and transient feature, mostly occurring in regions of residual crustal magnetic field.

The above observations indicating that Mars' aurora is a time dependent feature seem consistent with the scenario of acceleration of electrons by transient parallel electric field along semi-open magnetic field lines. The altitude distribution of these emissions was investigated and modeled by Soret et al. (2016) who measured three auroral limb profiles. Following correction for the distance from the tangent point, they found a mean peak altitude of $137 \pm 27$ km. They compared these values to the results of Monte Carlo model simulations indicating that the characteristic electron energy was about 100 eV, in good agreement with the mean energies typically measured with ASPERA-3. They found that the brightness of the measured nadir intensities of the Cameron and $CO_2^+$ UVD bands was less than that calculated using the measured ASPERA energy spectra. We think that this difference is possibly a consequence of the inclination and curvature of the magnetic field lines.

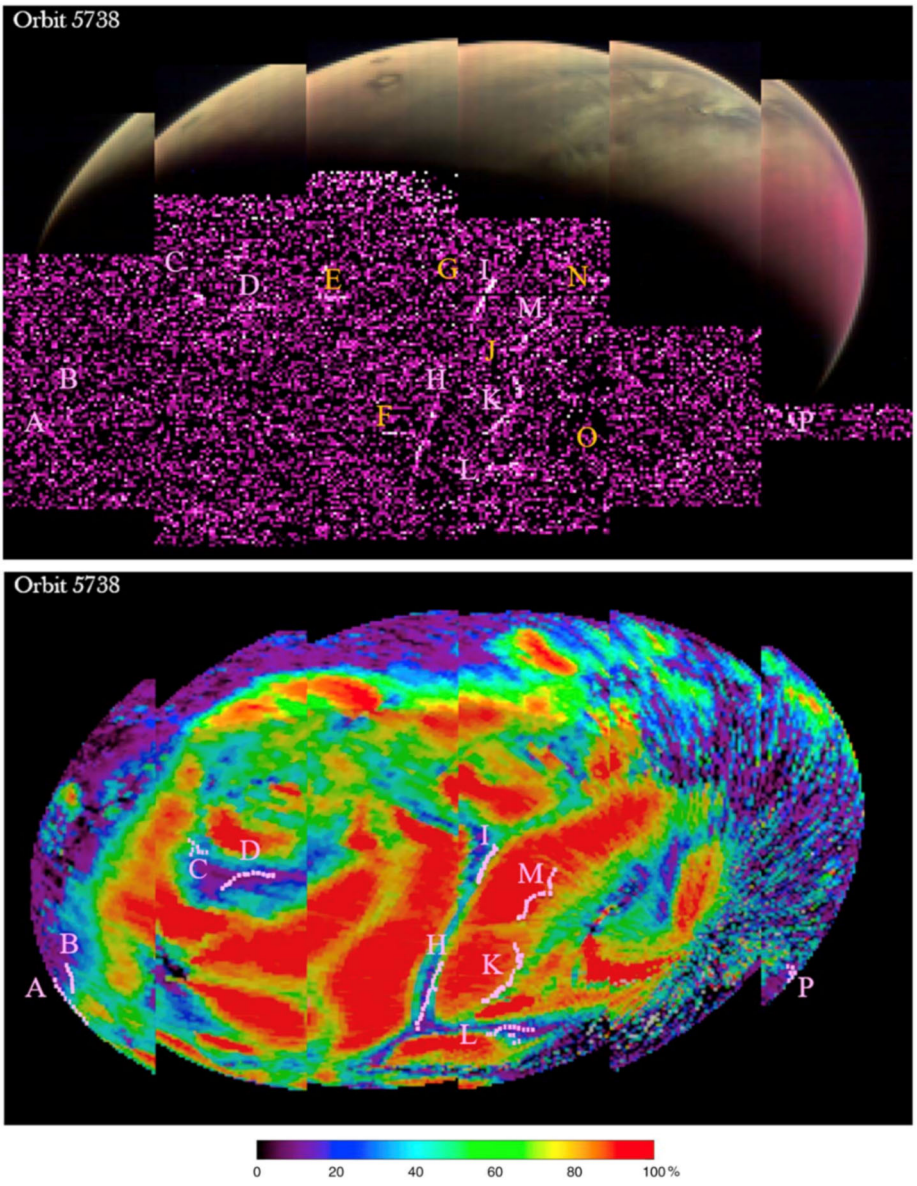


**Fig. 7** Top: Apoapse image of Mars orbit 5738 shows the daylight side middle UV colors maped up to visible colors. Bottom: Apoapse image of Mars orbit 5738 shows the nightside maped. The letters indicate the locations of confirmed emissions and the instrumental artifact (from Schneider et al. 2018). These observations are over plotted on Mars' crustal magnetic field topology (Brain et al. 2007)

### 3.2 IUVS Observations of Discrete Aurora

Discrete aurora was also observed by IUVS instrument onboard MAVEN with greater sensitivity and better spectral resolution than SPICAM. Figure 7 shows an apoapse image of discrete aurora on Mars in the orbit number 5738 during the space weather event which oc-

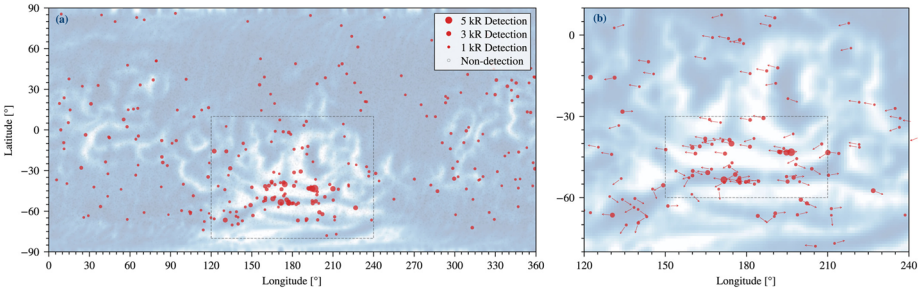


**Fig. 8** (**a**) In the left panel non-detection locations map of discrete auroras are shown. (**b**) Detection locations map of discrete auroras are shown in the right panel with red dots (from Schneider et al. 2021)

curred between 13 and 15 September 2017 (Schneider et al. 2018). In this figure top panel shows the day lit side with the middle ultraviolet colors mapped up to visible colors. Note that North is to the left side. The bottom portion of the figure shows the nightside imaged at high gains, using the black-purple-white color bars to indicate the intensity of CO Cameron band. Auroral emissions B, C, D, H, I and L appear in the dark region of the map. The A and P emissions were inconclusive in terms of aurora identification because they were too close to the limb (Schneider et al. 2018). Auroral emissions K and M lie very close to the statistically open field line region. The geographic locations of these auroral emissions are consistent with the criteria for discrete aurora as observed by SPICAM. It should be noted that all of the horizontal linear features (E, F, G, J, N and O) have been proved to be instrument artifacts. This is likely due to occasional cosmic ray showers, which affect a single slit position and detector read out, which appears exactly horizontal in this coordinate system. The rest of the features are all consistent with the auroral emission matching with CO Cameron band emission. The features identified as artifacts in the top panel are omitted from the bottom panel. The features in the top panel with confirmed auroral spectra are shown in purple with their identification letters. Schneider et al. (2018) used the map of Brain et al. (2007) that shows open and closed magnetic field lines based on MGS measurements at 400 km altitude. They transformed the magnetic field map into the observational coordinate system. The red color indicates closed field lines and dark blue color represents open field lines.

Until now the IUVS instrument has detected discrete aurora in 278 scans during 196 orbits over six years (Schneider et al. 2021). These events are highly correlated with the crustal magnetic fields in the southern hemisphere of Mars. In Figs. 8a and 8b non-detection and detection locations of discrete auroras are shown respectively. These events occurred primarily in the evening hours, when By component of the IMF field is negative. Under these conditions auroral events probably occur during the nighttime and may last for hours. Near the strongest fields, the occurrence rate of discrete auroras is $\sim 25\%$ of observations. These auroras are also distributed globally in about 1% of the observations in the regions of weak or no crustal fields. In many events strong electron precipitation is measured by MAVEN close in time to the UV emission (Soret et al. 2021). This association may not always be true because the electron measurements were made *in situ*, while the UV emissions are measured remotely.

Figure 9 shows the dependence of auroral occurrence frequency on radial magnetic field strengths. Schneider et al. (2021) observed discrete aurora forty times stronger during the highest magnetic field regions than at the rest of the planet, though such regions are rare. In Fig. 10 several spectral features in MUV wavelength range (180–340 nm) are identified

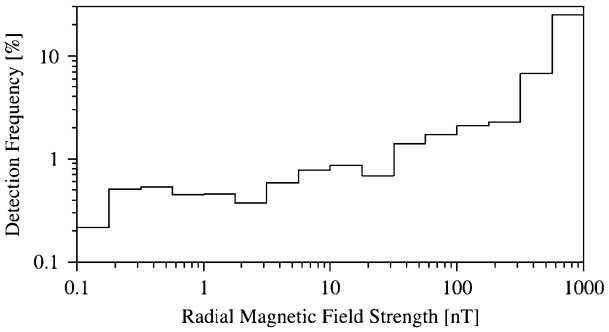


**Fig. 9** The detection frequency is shown vs. radial magnetic field strength. The histograms use logarithmically spaced bins with four bins per decade. Auroral events are forty times more likely to occur in the highest field regions than most of the rest of the planet, though such regions are rare (from Schneider et al. 2021)

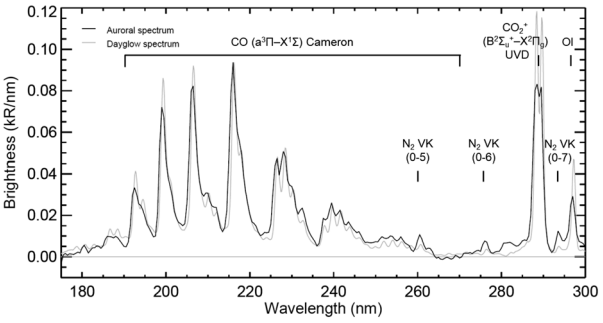


**Fig. 10** The averaged spectrum of the MUV IUVS auroral detections (black line). A MAVENIUVS dayglow spectrum (Gérard et al. 2019), whose intensities have been normalized to the strongest CO Cameron emission band, is plotted in grey for comparison (from Soret et al. 2021)

(1) CO ($a^3\pi - X^1\Sigma$) Cameron bands between 190–270 nm, (2) the $CO_2^+$ ($B^2\Sigma_u^+ - X^2\pi_g$) UVD at 288–289 nm and (3) OI at 297.2 nm. For the first time $N_2$ Vegard-Kaplan bands 0–5, 0–6, and 0–7 at wavelengths 260.4 nm, 276.1 nm and 293.7 nm have been detected in the discrete aurora (Soret et al. 2021). The presence of oxygen 297.2 nm emissions suggest that the oxygen green line emission at wavelength 557.7 nm should also be detectable from a visible spectrometer and should be visible to astronauts. Attempts to detect it from TGO (NOMAD/UVIS) have failed so far (Soret et al. 2021).

### 3.3 MARSIS/ASPERA Observations During Discrete Aurora

MARSIS is a low to high frequency (0.1 MHz to 5.5 MHz) ionospheric sounding radar aboard MEX, which has been sounding the planet since mid 2005. It is working in two different operational modes. One of these is the Active Ionospheric Sounding (AIS) (Picardi et al. 2004; Gurnett et al. 2005), which, basically, is a topside sounding mode to measure the topside electron density profile. This profile can then be used to obtain the Total Electron Content (TEC) of the topside ionosphere. The other operational mode is the subsurface mode, in which the radar sounds the surface and subsurface of the planet to identify and to measure the material below it. In the subsurface mode, TEC is derived as a by-product from the analysis of signal distortion caused by the dispersive ionosphere (Safaeinili et al. 2007; Leblanc et al. 2008; Mouginot et al. 2008; Cartacci et al. 2013; Sánchez-Cano et al. 2015). In the AIS mode MARSIS measures reflections from normal ionosphere in nadir direction (called *vertical echoes*) and ionization bulges in the oblique directions (called *oblique echoes*) (Duru et al. 2006; Andrews et al. 2014; Diéval et al. 2018; Venkateswara Rao et al. 2019). The peak frequencies of these echoes are generally the same. However, in a few

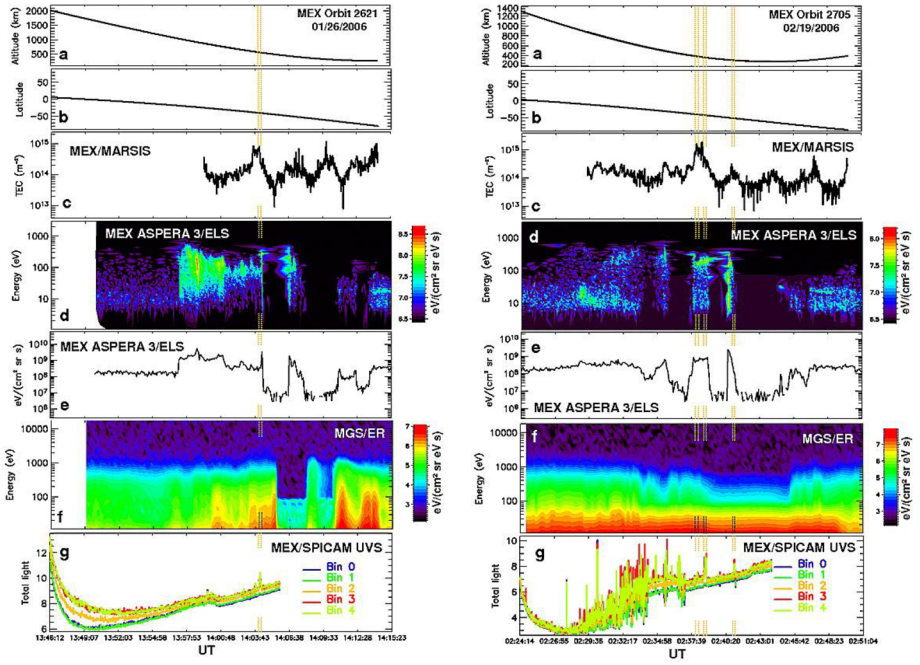


**Fig. 11** Time series of the measurements during orbit 2621 (left) and 2705 (right). Shown is the MEX (**a**) altitude and (**b**) latitude, (**c**) MARSIS TEC, (**d**) MEX/ASPERA-3/ELS electron measurement in $\mathrm{eV}/(\mathrm{cm}^2\,\mathrm{ster}\,\mathrm{eV}\,\mathrm{s})$, (**e**) MEX/ASPERA-3/ELS energy flux, (**f**) MGS/ER electron energy flux in $\mathrm{eV}/(\mathrm{cm}^2\,\mathrm{ster}\,\mathrm{eV}\,\mathrm{s})$, and (**g**) SPICAM UVS observation respectively (from Leblanc et al. 2008)

cases peak frequencies of oblique echoes were much larger than those of vertical echoes (Venkateswara Rao et al. 2019).

The objective of Analyzer of Space Plasma and Energetic Atoms (ASPERA-3) experiment is to study the solar wind – atmosphere interaction and to characterize the plasma and neutral gas environment within the Martian space through the use of ENA imaging and by measuring local ion and electron plasma. This instrument carries a comprehensive plasma package consisting of: (1) Ion Mass Spectrometer (IMA), (2) Electron Spectrometer (ELS) and (3) Neutral Particle Detector (NPD) covering energy ranges 0.01–30 keV, 0.01–20 keV and 0.1–10 keV respectively for these measurements.

Figure 11 represents the various measurements made by SPICAM UVS (Fig. 11g), MGS/ER (Fig. 11f), ASPERA-3/ELS (Figs. 11d and 11e), MARSIS (Fig. 11c), MEX altitude (Fig. 11a) and latitude (Fig. 11b) during the orbits 2621 and 2705 on 26 January and 19 February respectively. The dotted vertical lines in Fig. 11g indicate the time of auroral emissions at 1404 UT and 0238 UT during the orbit 2621 and 2705 respectively. These observations were carried out in the nighttime above the most intense crustal magnetic field locations recorded by MGS. Leblanc et al. (2008) showed a good correlation between the auroral emissions observed by SPICAM with electron flux observed by ASPERA-3 as well as with TEC observed by MARSIS in subsurface mode. They reported that TEC increased significantly when the high electron flux was precipitating into the Martian atmosphere. During auroral event, the electron flux increased by an order of magnitude while it decreased by two orders of magnitude before and after this event. They also observed a high peak in TEC during the SPICAM observations of aurora. This observation suggests that the peak

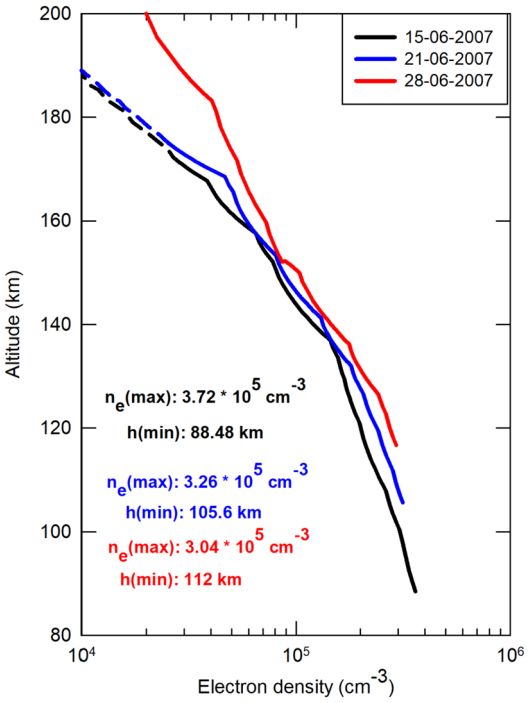


**Fig. 12** Dispersion corrected electron density profiles of MARSIS oblique echoes observed on 15, 21, and 28 June 2007. The dashed black and blue lines are due to interpolation of the electron density profiles between the density at the spacecraft and that of the lowest sounding echo (from Venkateswara Rao et al. 2019)

electron density increased significantly in the auroral ionosphere of Mars during this event. However, no correlation was demonstrated between the SPICAM auroral detections and the occurrence of solar energetic particle events inferred from the MGS/ER data set (Gérard et al. 2015).

The precipitating electron flux observed by ASPERA-3 represents a non-Maxwellian distribution similar to that observed as V-shaped potential structure in the Earth's auroral zone (Brain et al. 2006; Lundin et al. 2006, 2011; Ip 2012; Haider and Mahajan 2014; Bisikalo et al. 2017). The auroral electrons are precipitating downward into this potential well, which is maintained by the strong electric and magnetic fields. In this region the horizontal components of magnetic field are small compared to the vertical components. The auroral events are mostly observed during the disturbed solar wind conditions and after emission of CME/SEP from the sun (Schneider et al. 2018; Haider and Masoom 2019).

Figure 12 represents three enhanced electron density profiles observed by MARSIS in AIS mode on 15, 21, and 28 June, 2007 during orbit # 4426, 4447 and 4469 at Ls = 258°, 262° and 266° respectively (Venkateswara Rao et al. 2019). These profiles were observed in MY 28, when a global dust storm was encircling around Mars. In this figure the observed peak electron densities are $3.75 \times 10^5$ $cm^{-3}$, $3.26 \times 10^5$ $cm^{-3}$ and $3.04 \times 10^5$ $cm^{-3}$ at altitudes $88.48 \pm 6.9$, $105.60 \pm 5.2$ and $112 \pm 5.5$ km respectively (Venkateswara Rao et al. 2019). These observations were carried out at SZA $\sim 55°$ in the mini-magnetosphere of Mars between latitude 54°S to 55°S and longitude 177°E to 182°E. Note that the altitudes of the electron density peaks in these three cases are lower than that of the normal ionospheric peak altitude of 134 km (Němec et al. 2011). The peak density of the first case is in fact the highest ever observed in the Martian ionosphere and the observation of such enhanced ionization at an altitude of $88.48 \pm 6.9$ km is unusual and needs some explanation.

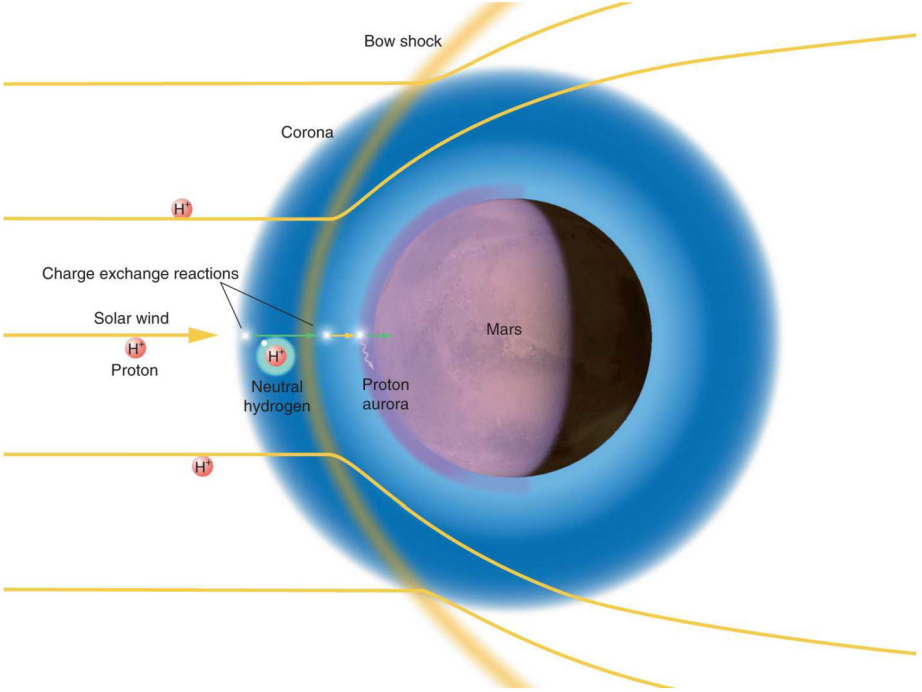


**Fig. 13** Mechanisms for Martian proton aurorae originating from solar wind charge exchange. Upsteam solar wind protons ($H^+$) are typically deflected by the Martian bow shock (yellow stream lines), but some charge exchange with neutral hydrogen in the corona (blue), becoming energetic neutral particles (shown as a proton surrounded by a shell (cyan) containing an electron (white dot)). These neutral particles freely pass through the bow shock while retaining the original kinetic energy and direction of the solar wind (green arrow) and deposit energy in the planet's thermosphere. A fraction of this energy is emitted from the energetic hydrogen as Ly $\alpha$ photons (from Deighan et al. 2018)

The solar wind/SEP electron precipitation that yields auroral photon emission can cause ionization bulges measurable by ionospheric sounding. This process of aurora is not modeled. Recently, Venkateswara Rao et al. (2019) proposed that the enhanced ionization in the dust storm may occur due to a strong convective motion of plasma in presence of electric and magnetic fields. However, they didn't interpret the echoes as aurora.

## 4 Proton Aurora on Mars

Mars has observed the hydrogen corona extending up to several thousands of kilometer (Chaufray et al. 2007). The solar wind protons interact with this corona through charge exchange and thereby produce a beam of ENA at solar wind speeds (Kallio and Janhunen 2001; Kallio and Barabash 2001; Gunell et al. 2006; Halekas et al. 2015). Figure 13 represents the mechanism of Martian proton aurora originating from solar wind charge exchange (Deighan et al. 2018; Hughes et al. 2019). In this process fast hydrogen atoms are produced due to charge exchange between solar wind protons ($H^+$) and hydrogen corona. These energetic hydrogen atoms have the same energy as protons and these atoms move in the same direction as protons just before the collisions. The fast hydrogen atoms penetrate deep in the Martian

**Table 1** Characteristics of the Proton Aurorae Observations (Ritter et al. 2018)

| Orbit # | Date | Ls (deg) | Time (hh:mm) | TP latitude (deg) | TP Longitude (deg) | TP SZA (deg) | Intensity (kR) |
|---|---|---|---|---|---|---|---|
| 1357/2 | 6/2/2005 | 156 | 17:16 | 55.4 | 198.8 | 49.3 | $0.7 \pm 0.2$ |
| 1426/1 | 26/2/2005 | 166 | 01:02 | 71.7 | 300.9 | 74.5 | $1.1 \pm 0.3$ |
| 2231/2 | 9/10/2005 | 303 | 10:33 | 1.7 | 120.1 | 23.0 | $0.9 \pm 0.2$ |
| 2329/2 | 5/11/2005 | 319 | 20:40 | 58.3 | 199.1 | 55.0 | $0.9 \pm 0.2$ |
| 4354/1 | 26/5/2007 | 245 | 20:44 | 25.3 | 345.5 | 48.8 | $1.4 \pm 0.2$ |
| 4419/1 | 14/6/2007 | 257 | 01:19 | 59.6 | 85.4 | 46.6 | $1.8 \pm 0.5$ |

atmosphere and deposit their energy in the lower thermosphere at altitudes $\sim$ 110–130 km resulting in ionization, dissociation, heating, excitation and auroral emission. The proton aurora is produced by Lyman-$\alpha$ (121.6 nm) due to emission of fast (excited) hydrogen atoms from the upper ($^2$p) state to the ground state ($^1$s) (Shematovich et al. 2011; Gérard et al. 2019).

Ritter et al. (2018) suggested that the main driver of these events could be CMEs or CIRs, which enhance solar wind density and flux that can reach the Martian environment and create aurora. The CMEs are ejected into the interplanetary space after the eruption of solar flares from the sun. In CIRs fast and slow solar wind plasmas are emitted from persistent coronal holes over multiple solar rotations of the sun. The fast CMEs can drive multiple shocks. A large shock can reach Mars faster than the slower shock and create dense auroral ionosphere on Mars. The fast shock also compresses the E peak to altitudes as low as 100 km, while the normal peak occurs at 110 km during solar quiet conditions (Haider et al. 2012).

### 4.1 SPICAM Observations of Proton Aurora

Recently Ritter et al. (2018) have observed six events of proton auroras in the daytime atmosphere of Mars from SPICAM UV spectrometer aboard MEX during the period July 2004 to May 2011. The characteristics of these auroras are given in Table 1. Figures 14a to 14f show six limb profiles of proton auroras. Ingress and egress scan profiles are plotted by red and blue colors respectively. The horizontal bars indicate uncertainty in the SPICAM observations. The ingress profile of orbit 2231/2 represents a weak aurora. The ingress profile did not measure the aurora during orbit 4419/1. The egress profile 4354/1 does not represent any auroral signature. The Lyman-$\alpha$ intensity profile shows a clear peak of 3 to 6 kR during the auroral event. When this peak disappeared, so did the aurora. Figure 14g shows a global map of the magnetic field on Mars at about 400 km (Mitchell et al. 2001; Haider et al. 2010). In this figure, locations of SPICAM proton auroras and SPICAM discrete auroras are shown by white and black stars respectively (Gérard et al. 2015; Soret et al. 2016). Figure 14h shows that the SPICAM proton auroras (shown by red color) were observed during declining and minimum phase of solar cycle 24.

Ritter et al. (2018) identified that the CMEs/CIRs arrived at Mars during the time of these auroral events (https://cdaw.gsfc.nasa.gov/CME_list and https://www.helcats-fp7.eu/catalogues/wpu_arrcat.html). These auroras have been observed in northern hemisphere of Mars where the crustal magnetic fields are weak as well as in the southern hemisphere where fields are strong. During the auroral events the limb emission intensity peaks at about 120 to 150 km due to precipitation of solar wind proton/hydrogen atoms ($H^+$-H). These

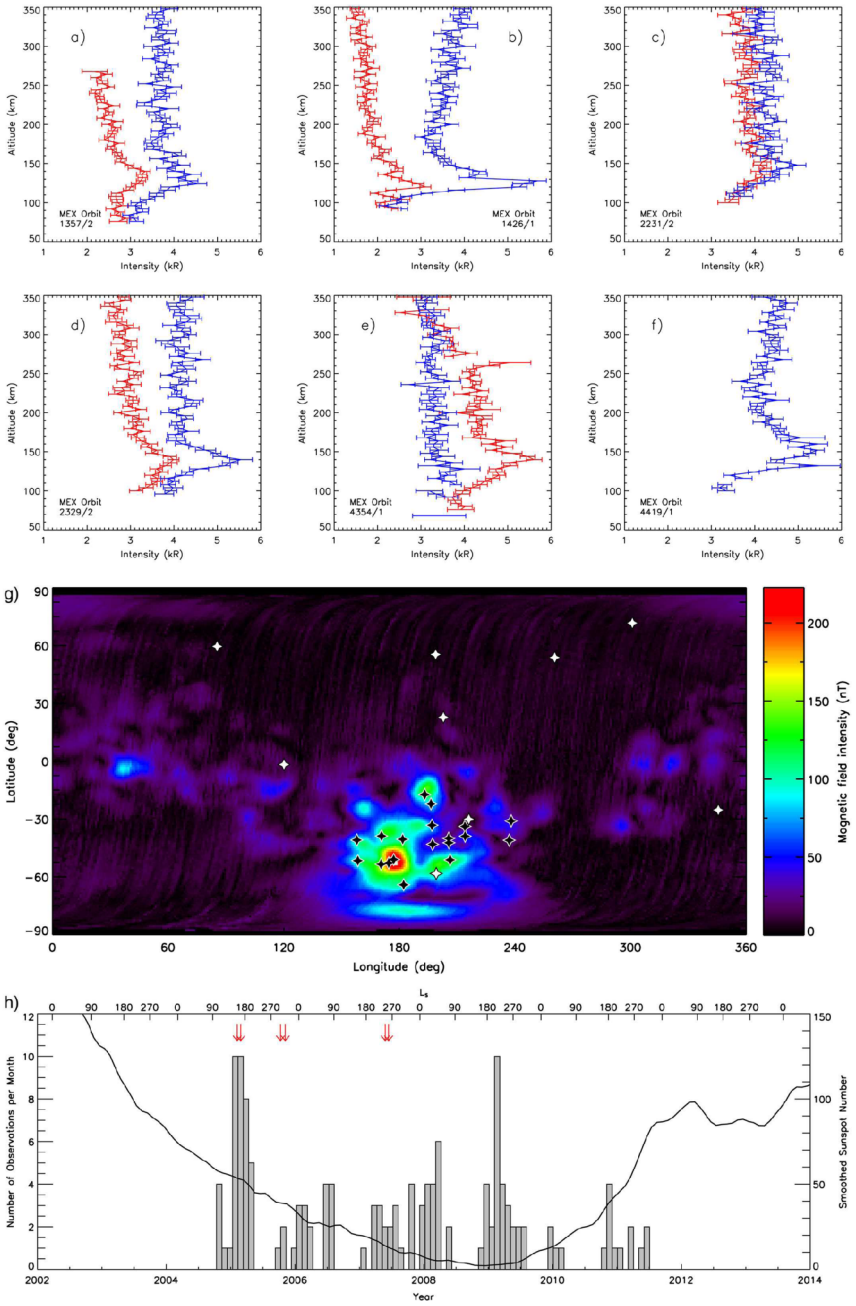


**Fig. 14** (**a**–**f**) represent the Lyman $\alpha$ limb profiles of the six orbits where Mars' aurora was observed. Ingress observations are drawn in red and egress observations are shown by blue, (**g**) The SPICAM proton (white) and SPICAM discrete aurora observations (black) are displayed on a map that shows the statistical Martian magnetic field intensity at 400 km altitude, (**h**) The histogram shows the distribution of all SPICAM limb observations selected for this study with respect to solar cycle and Martian season (Ls). The solid line represents the smoothed monthly sunspot number and the red arrows indicate the six auroral observation dates (from Ritter et al. 2018)

observations were carried out when the spacecraft was located between altitude 300 km to 700 km at latitudinal separations from 18° to 35° between the ingress and egress scans.

### 4.2 IUVS Observations of Proton Aurora

The limb observation of proton aurora was observed by IUVS instrument onboard MAVEN during the daytime atmosphere of Mars (Deighan et al. 2018) and subsequently identified in earlier observations of SPICAM on MEX (Ritter et al. 2018). Both observations showed similar shapes of the Lyman-$\alpha$ limb profile enhancement and comparable peak intensities (Gérard et al. 2019). The IUVS measures the airglow emissions using far UV (110–190 nm) and mid-UV (180–340 nm) channels. In Fig. 15a we demonstrate the Lyman $\alpha$ profiles of Martian proton aurora in the dayside atmosphere of Mars for orbits # 985 and 986 on 3 and 4 April, 2015 at 07:33 LT and 12:04 LT respectively. The brightest peak of this aurora occurred at SZA $\leq 40°$ (see Fig. 15b). These auroras disappeared near the terminator. In these observations the UV dayglow emissions due to carbon dioxide ionizations and its dissociation into CO and Oxygen bands (135.6 nm and 130.4 nm) are also seen. The emission intensities represent a broad peak at $\sim$ 130 km. In the orbit # 985 the Lyman $\alpha$ represents nearly a flat profile due to multiple scattering. After about 4.5 hour the Lyman $\alpha$ profile developed a strong peak of proton aurora in orbit # 986.

The proton aurora is created via electron stripping and charge exchange between solar wind protons and hydrogen corona. This aurora is strongly enhanced during southern summer when loss of water is maximum, which increases hydrogen corona on Mars. The hydrogen corona originates from the photo-dissociation of water vapor produced $H_2$, which then diffuses into the upper atmosphere, where it is destroyed into H and then escapes to space (Fox 2015; Haberie et al. 2017; Jakosky et al. 2018; Stone et al. 2020). The photo-dissociation is maximum during the southern summer when Mars is closest to the Sun. In MY34, dust events boosted the escape rate of H atoms by a factor of 5 to 10 during the southern summer (Chaffin et al. 2021). The charge exchange between solar wind protons and hydrogen corona produce ENAs, which pass unimpeded through the bow shock and subsequently undergo additional charge exchanges and collisions with neutrals in the lower atmosphere to create proton aurora (Deighan et al. 2018; Hughes et al. 2019). Therefore, proton aurora can serve as a proxy for water loss from Mars.

MAVEN also carried a Solar Wind Ion Analyzer (SWIA) instrument to measure the ion flux with energies from 5 eV to 25 keV. Figure 16 shows time variation of dayside proton flux and mean IUVS Lyman $\alpha$ intensity enhancement at periapsis altitude during March and April, 2015. Three peaks of proton fluxes of $2.8 \times 10^6$ cm$^{-2}$ s$^{-1}$, $1.65 \times 10^6$ cm$^{-2}$ s$^{-1}$ and $0.78 \times 10^6$ cm$^{-2}$ s$^{-1}$ have been observed on 8 March 2015, 1 and 3 April 2015 during orbits # 850, 975 and 986 respectively (Deighan et al. 2018). These peaks are produced by the ENAs associated with the penetrating protons observed by the SWIA instrument. Halekas et al. (2015) also studied the energy and flux of penetrating protons into the atmosphere of Mars. They observed maximum proton flux $\sim 3.0 \times 10^5$ cm$^{-2}$ s$^{-1}$, $2.8 \times 10^6$ cm$^{-2}$ s$^{-1}$ and $3.2 \times 10^5$ cm$^{-2}$ s$^{-1}$ on 27 February, 8 and 24 March 2015, respectively at periapsis altitude during the daytime.

### 4.3 ENAs Precipitation

The hydrogen ENAs are produced in the vicinity of Mars when the solar wind protons undergo charge exchange with atoms from the exosphere. Due to neutrality, ENAs are decoupled from electromagnetic fields and propagate freely. Because of their energy which is

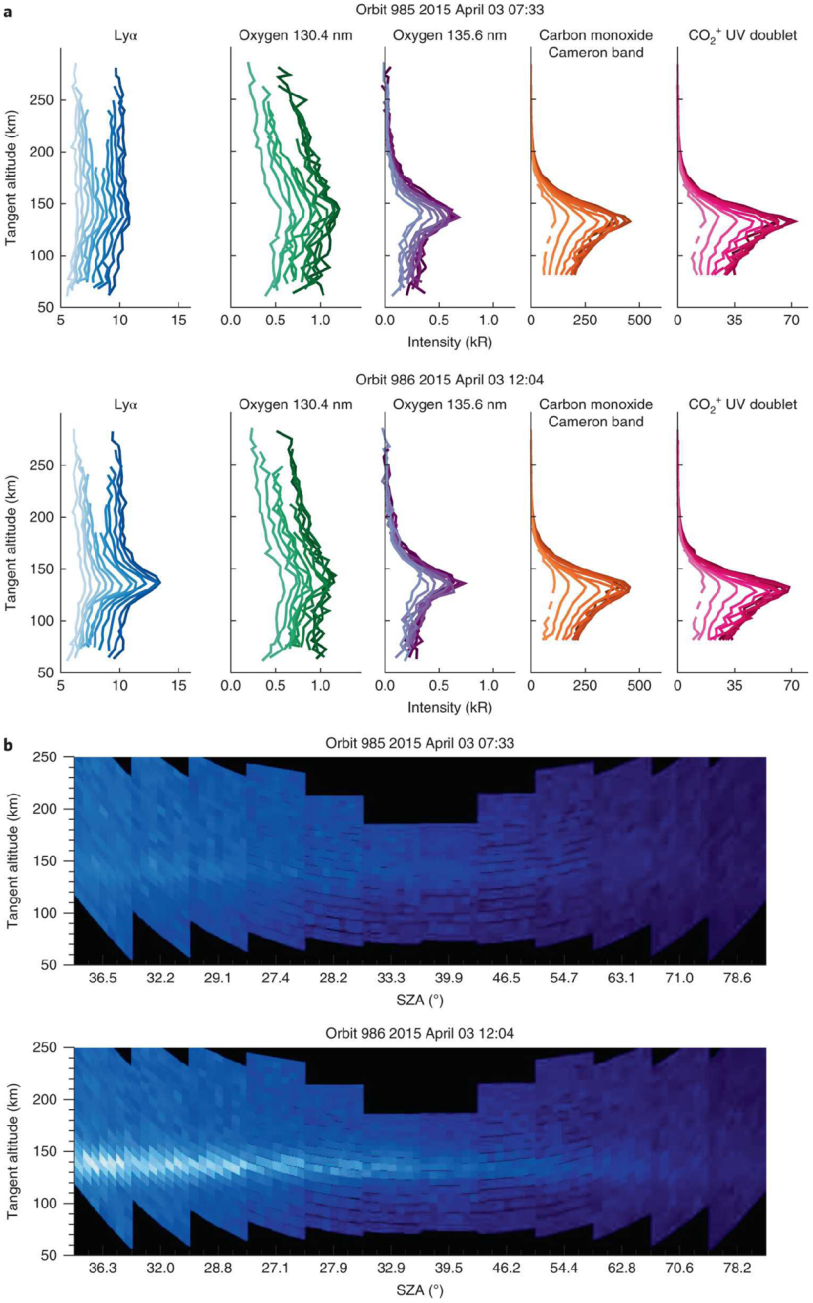


**Fig. 15** (**a**) IUVS observed brightness profiles for Ly $\alpha$ and several $CO_2$ ionization and dissociation products on MAVEN orbits 985 and 986. Each emission plot contains profiles from 12 limb scans with shading from dark to nights indicating chronological order of acquisition. (**b**) The same Ly $\alpha$ brightness in a synthetic image format showing the illumination of 12 limb scans ordered from left to right. Each scan has 21 integrations (vertical) with 7 spatial samples along the length of 10.6° IUVS airglow slit (horizontal). For both orbits, $CO_2$ absorption of Ly $\alpha$ becomes important for tangent altitudes of less than 120 km (from Deighan et al. 2018)

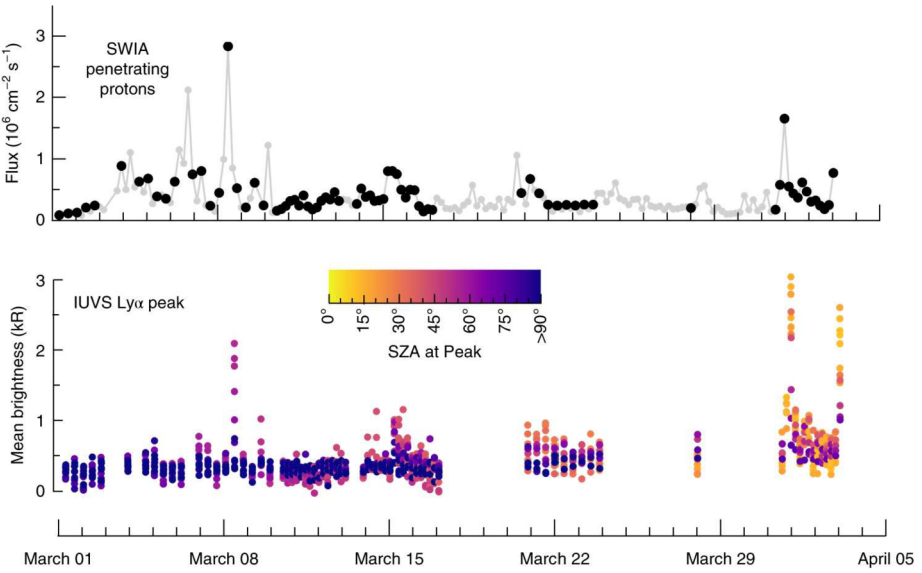


**Fig. 16** SWIA fluxes are single valued per orbit based on the dayside portion of periapse data. SWIA data points have a larger black symbol when a joint IUVS observations set is available. IUVS data contain values for each of the 12 limb scans per orbit, representing the mean brightness from 110 km to 160 km where peaks occur. Each sample is colored according to the SZA of the tangent point at the peak. The background fluorescent source has been subtracted using the mode of the brightness above 160 km (from Deighan et al. 2018)

$\leq$ 1 keV, the gravitational effect is negligible. ENAs can thus reach low altitudes and precipitate into the atmosphere. There are very few observations of Martian ENAs because ASPERA-3 is the only experiment at Mars capable for performing such measurements (Barabash et al. 2006; Futaana et al. 2006a,b,c; Galli et al. 2006a,b; Grigoriev et al. 2007). ENAs are produced in the magnetosheath of Mars. The modeling studies have focused on ENA production rates both upstream of the bow shock and in the magnetosheath (Kallio and Janhunen 2001; Kallio and Barabash 2001; Haider et al. 2002; Galli et al. 2008; Diéval et al. 2012; Haider and Masoom 2019). According to these simulations 1–3% of the solar wind protons are charge exchanged into ENAs upstream of the bowshock for nominal solar wind conditions (Kallio et al. 1997). In this region the fast hydrogen atoms have the same energy, which moves in the same direction, as protons just before the collisions. In this process the solar wind protons turn into fast hydrogen atoms at high altitudes. The combined atoms ($H^+$-H) penetrate deeper into the Martian atmosphere and lose their energy at low altitudes after collision with atmospheric gases.

Figures 17a and 17b represent the precipitating proton flux and energy flux with respect to SZA respectively, at a fixed altitude of 207 km (Kallio and Janhunen 2001). In these figures, the variations of fluxes are shown by dotted-dashed curve in the $+E_{sw}$ hemisphere. The flux in $-E_{sw}$ hemisphere is shown with a dashed curve, while the average flux in both hemispheres is shown by solid curve. The solar wind flux, when it can hit the atmosphere directly, is shown as dotted curve. A sketch of the hemisphere is also indicated at the corner of this figure. Figures 18a and 18b represent the precipitating hydrogen flux and energy flux with respect to SZA respectively, at a fixed altitude of 207 km (Kallio and Barabash 2001). The two curves represent the solar wind proton ENAs produced upstream of the bow shock (dot-

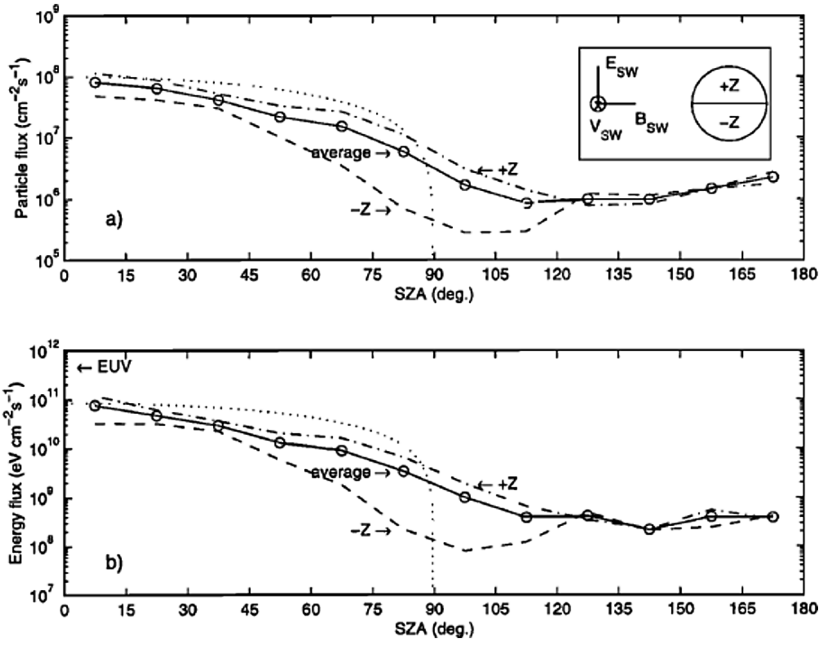


**Fig. 17** (**a**) Particle and (**b**) energy flux of precipitating $H^+$ ions into the Martian atmosphere at different SZA. The solid lines with open circles show the average flux on the atmosphere. The dash-dotted lines show the flux to the $+Z$ ($Z > 0$) hemisphere, and the dashed line shows the flux to the $-Z$ ($Z < 0$) hemisphere. The dotted lines in Fig. 13a and 13b represent the flux $\sim 1 \times 10^8$ cos (SZA) cm$^{-2}$ s$^{-1}$ and $\sim 856 \times 10^8$ cos (SZA) eV cm$^{-2}$ s$^{-1}$ respectively, which corresponds to total solar EUV flux in the wavelength range from 15 Å to 1026 Å. The small figure on the top right corner in Fig. 13a illustrates the $+Z$ ($Z > 0$) and $-Z$ ($Z < 0$) hemispheres with respect to the direction of the convective electric field in the solar wind ($E_{sw}$) (from Kallio and Janhunen 2001)

ted curve) and the total amount of ENAs (produced upstream and downstream) (solid line). These calculations are made from Hybrid model (Kallio and Janhunen 2001; Kallio and Barabash 2001). This model predicts that there is no precipitating hydrogen ENAs beyond SZA $\sim 100°$, in contrast to proton precipitation which also exists even during the nighttime. Therefore the precipitating protons can be an ionization source in the daytime and as well as in the nighttime atmosphere. But hydrogen ENAs do not precipitate in the nighttime atmosphere. It is found that the precipitating ENAs energy flux is two orders of magnitude smaller than the proton energy flux. The precipitating $H^+$-H particles deposit their energy via collision with atmospheric gases at an altitude $\sim 120$ km (Haider et al. 2002; Bisikalo et al. 2018; Gérard et al. 2019). The Hybrid simulation indicates that the precipitating $H^+$-H flux is the highest at the sub-solar point and decreases towards the nightside of Mars.

### 4.4 Electron and Proton Precipitation

Electron fluxes with typical magnetosheath energy distribution are frequently observed within the Induced Magnetosphere Boundary (IMB) (e.g. Soobiah et al. 2006; Halekas et al. 2015; Dubinin et al. 2017). The crustal and induced magnetic fields together play a very important role in the morphology of electron and proton entry into the atmosphere of Mars. It is known that Mars contains an induced magnetosphere (Yeroshenko et al. 1990;

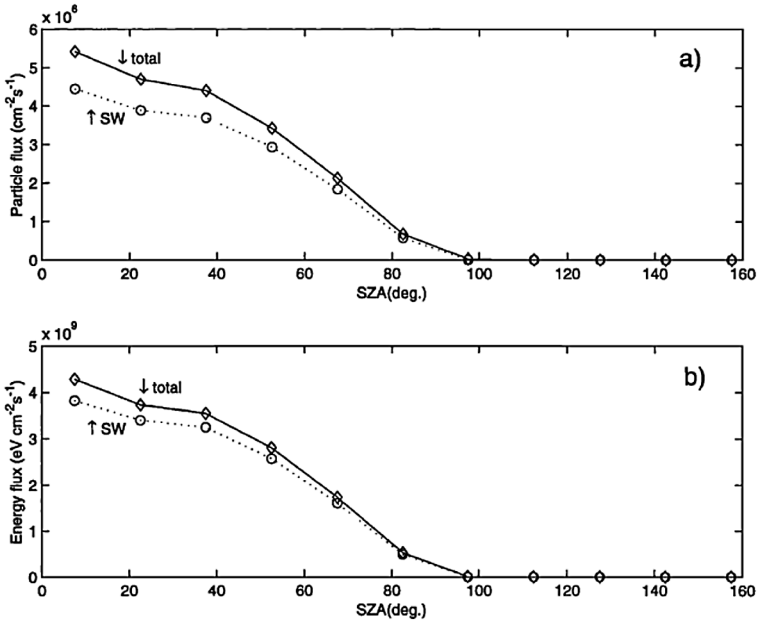


**Fig. 18** (**a**) The particle and (**b**) the energy flux of precipitating hydrogen atoms for different SZA. The flux (SW) of fast hydrogen atoms formed in the solar wind upstream of the bow shock is shown by dotted lines. The flux (total) that also includes the hydrogen atoms formed downstream of the bow shock is shown by solid lines (from Kallio and Barabash 2001)

Mitchell et al. 2007; Nagy et al. 2004; Ramstad et al. 2020). The IMF field line piles up around the planet to form a magnetic barrier on the dayside and then drape around the planet and finally stretch due to mass loading and form a magnetotail (see Fig. 19). The magnetic field measurements onboard Phobos 2 and MGS have confirmed that the Martian magnetotail is mainly an induced one. However, the possibility of existence of a weak intrinsic magnetic field is not ruled out (Verigin et al. 1991; Brain et al. 2003; Haider et al. 2013; DiBraccio et al. 2018).

The strong crustal magnetic fields provide a shielding effect to the solar wind plasma. The merging of the radial fields with IMF forms cusp-like structures that facilitate the entry of electrons (Mauk and Bagenal 2012). When such merging occurs, the electrons can follow the open field lines of the cusps and travel down to the atmosphere (Brain et al. 2006; Matsunaga et al. 2015). The nightside ionosphere of Mars can have two main sources of plasma. The first being magnetic field geometry topology (Lillis et al. 2013; Xu et al. 2016) resulting in impact ionization from precipitating electrons of solar wind origin (Verigin et al. 1991; Haider et al. 1992; Fox et al. 1993; Haider 1997; Lillis et al. 2011; Haider et al. 2013). The second source is thought to be day-to night plasma transport across the terminator (Fränz et al. 2010; Chaufray et al. 2014; Cui et al. 2015). Viking 1/2, Mars 4/5 and MEX have observed a broad peak in the nighttime ionosphere of Mars between altitude 140 km and 160 km at SZA 101° to 125° (Savich and Samovol 1976; Vasiliev et al. 1975; Zhang et al. 1990; Withers et al. 2012). Fowler et al. (2015) found that in the weak crustal field region ($B < 20$ nT) the occurrence rate of the nightside ionosphere decreased with increasing SZA up to $\sim 125°$. They suggested that dayside plasma transport plays a crucial role for ionospheric formation in this region. For strong crustal field regions ($B > 20$ nT) they did not

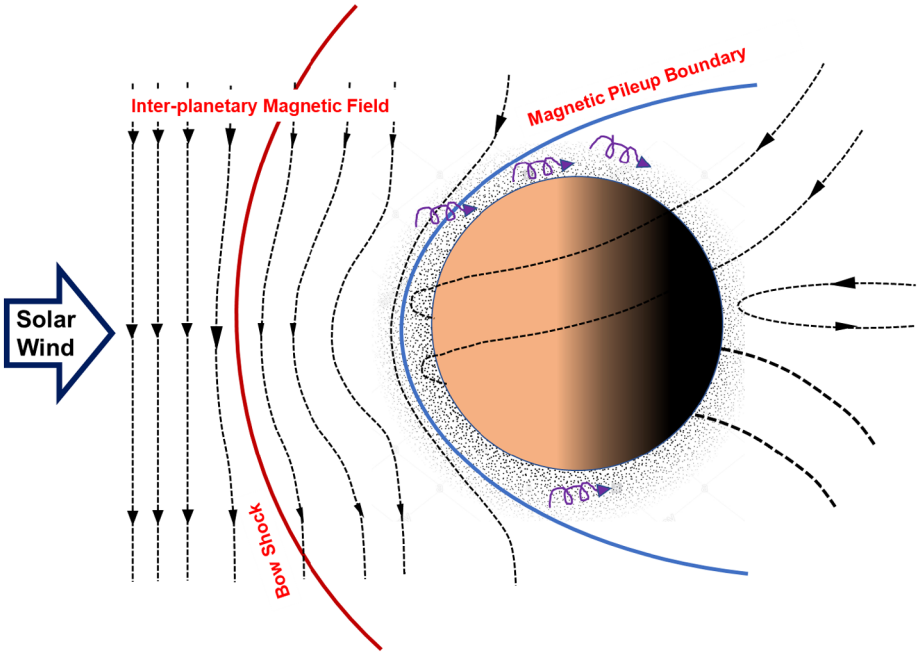


**Fig. 19** The schematic representations of horizontal plasma transport from dayside to nightside ionosphere across the terminator region

find any SZA dependence. The nightside occurrence rate was more than 4 times greater for near vertical aligned magnetic fields when compared with the horizontally aligned magnetic fields, suggesting the precipitating electrons could be a key ionization source for this region.

The solar wind protons have been observed at altitudes as low as 270 km in the Martian ionosphere. The low altitude protons were first reported by Lundin et al. (2004). Dubinin et al. (2008) reported that the solar wind protons penetrate deeper into the dawn side atmosphere than on the dusk side atmosphere. Diéval et al. (2012) analyzed this event further and suggested that the finite gyro radius effect may cause the observed proton precipitation into the ionosphere of Mars. It should be noted that these protons and electrons have low energy (few 100 eV) and thus can always reach into the upper atmosphere of Mars (Bisikalo et al. 2018). The discrete aurora, proton aurora and diffuse auroras are produced at Mars for a few hours during disturbed conditions of the sun when the high energy (1 keV–100 keV) accelerated protons and electrons associated with ENAs, and CMEs or SEPs precipitate into the atmosphere of Mars.

## 5 Diffuse Aurora on Mars

Schneider et al. (2015) observed diffuse auroral emission of $CO_2^+$ ($B^2\Sigma_u^+ - X^2\pi_g$) Ultraviolet Doublet (UVD) band at 289 nm band from IUVS instrument in the nighttime atmosphere of Mars due to the precipitation of SEP electrons at 1 microbar altitude. This aurora is neither connected to the magnetic field nor restricted to any fixed location (in terms of latitude and longitude). It is thus related to SEP impact on the Mars' atmosphere. Recently Gérard et al. (2017) have used incident flux of $\sim 1$ mWm$^{-2}$ at the top of the atmosphere

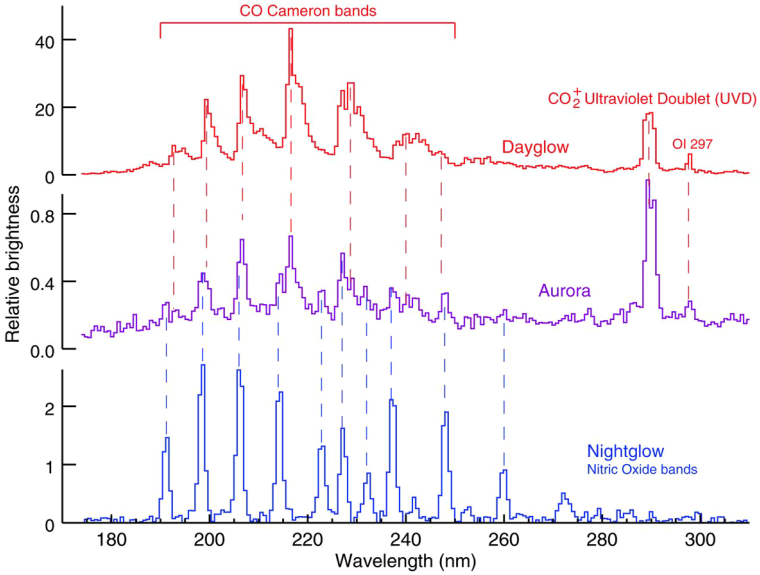


**Fig. 20** The top spectrum shows three dayglow emission features from the ionization and dissociation products of $CO_2$ created by solar EUV radiation. The bottom spectrum shows nightglow NO emission. Dotted lines from peaks in the top and bottom spectra show that the middle spectrum from the nightside is a combination of features seen in dayglow and nightglow indicating that particle precipitation (auroral event) is responsible there for creating the spectral features of dayglow on the nightside. The difference at 289 nm is most pronounced as the nitric oxide and Cameron bands have considerable overlap. Spectra were obtained during orbit # 114 (top), 437 (middle) and 387 (bottom). OI refer to emission from neutral oxygen (from Schneider et al. 2015)

and calculated limb intensity profiles of $CO_2^+$ UVD band for comparison with IUVS observations. They found that electrons of 100 keV can produce the observed peak limb intensity of diffuse aurora. Later Haider and Masoom (2019) used Hybrid model and AYS approach based on Monte Carlo simulation to study the auroral ionosphere of diffuse aurora due to precipitation of $H^+$-H fluxes and SEP electrons of energies of 25 keV to 100 keV in the nighttime ionosphere of Mars.

Figure 20 represents relative brightness of three types of mid-UV (180–340 nm) spectra observed by IUVS instrument at Mars (Schneider et al. 2015). The auroral emissions are not observed at far UV wavelength range (110–190 nm). The top spectrum shows the three dayglow emission features from the ionization of $CO_2^+$ UVD and dissociation products of $CO_2$ into CO Cameron and OI 297 bands. These spectra are created by solar EUV radiation. The bottom spectrum shows a nightglow feature of NO. The middle spectrum shows a nighttime auroral feature of $CO_2^+$ UVD, which are more pronounced than the nightglow spectrum of NO. The auroral emissions are $\sim 20$ times weaker than the dayglow emission. The diffuse aurora on Mars occurred on a global scale spanning over all longitudes in the northern hemisphere for the period from 17 to 21 December 2014 for the 17 periapse passes of orbits # 418 to 444. These observations were carried out in the nighttime at latitudes from 35°N to 70°N with the local time varying from 00:30 to 05:00 (Schneider et al. 2015).

Recently Schneider et al. (2018) have also observed 25 times brighter diffuse aurora in the nighttime from IUVS instrument onboard MAVEN during the space weather events that occurred in September, 2017. Figure 21 shows nightside image taken at the start and at the peak of the space weather event. In the left image Mars' disk shows a uniform background

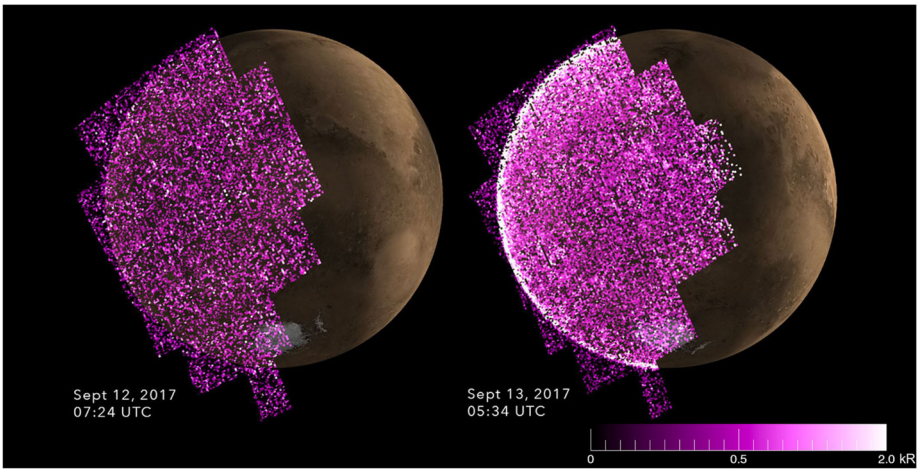


**Fig. 21** Mid-ultraviolet images of Mars' aurora during nighttime: left image at the start of the space weather event on 12 September 2017 at 07:24 UTC and right image at the peak of the space weather event on 13 September 2017 at 05:34 UTC. The purple-to-white brightness scale displays the auroral emission intensity from 0 to 2.0 kilo Raleigh (from Schneider et al. 2018)

consistent with the instrument noise and the limb shows a faint but significant brightening. The right side image, taken at the peak of the space weather event, shows a pronounced auroral emission during the entire nightside of Mars. The left side image was taken on 12 September, 2017 at 07:24 UTC during orbit # 5726. The right image was taken on 13 September, 2017 at 05:34 UTC during orbit # 5731. Both diffuse auroras observed by Schneider et al. (2015, 2018) are consistent with high energy particle precipitation.

### 5.1 Emission Intensity of Diffuse Aurora

Figure 22 represents a geographic distribution of auroral intensities of $CO_2^+$ UVD emissions superposed on a map of Mars. These auroras were observed during the 5 day period of SEP enhancements in December 2014. The observed nighttime auroral emissions had a spatial coverage from 35°N to 70°N. These observations were limited to the northern hemisphere. There is no correlation between the geographic location of the aurora and its brightness. Schneider et al. (2015) argued that local time seems to play an important role in controlling the diffuse auroral emissions. They have reported that while the diffuse aurora occurred in the midnight (00:30 hour) at low latitudes ($\sim$ 35°N), these occurred near the evening terminator ($\sim$ 17:00 hours) at high latitudes ($\sim$ 70°N).

Figure 23 represents observed vertical limb intensity profiles of nighttime diffuse aurora and dayglow emissions. The red curve denotes the $CO_2^+$ UVD dayglow emissions near the terminator. The purple curve indicates the $CO_2^+$ UVD limb intensity of diffuse aurora at the nightside terminator region. The modeled profile of diffuse aurora is also plotted in this figure from Schneider et al. (2015). The dayglow emissions are produced due to solar EUV absorption by the atmospheric gases in the altitude range 120 km and 150 km. The nighttime aurora is produced due to precipitation of SEP electrons, which excite auroral emission at an altitude around 70 km. The black curves represent the model profiles. The dashed lines show the estimated limb intensity profiles due to precipitation of monoenergetic electrons with energies 0.1 keV to 100 keV. As mentioned above the dayglow limb emission intensity

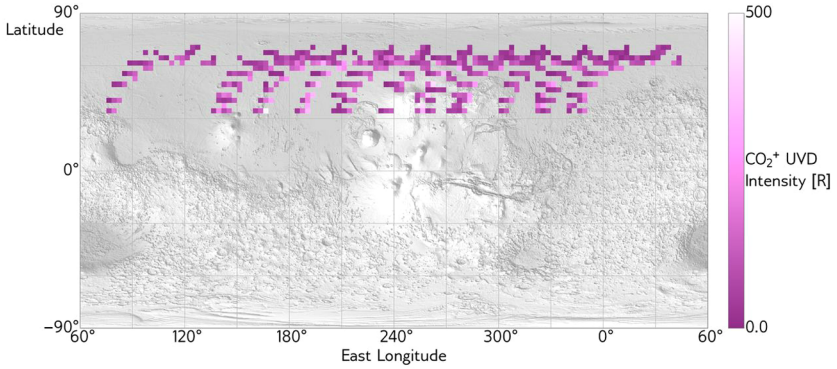


**Fig. 22** The $CO_2^+$ UVD emission brightnesses superposed on a map of Mars. The extent of emission was limited by the regions observed rather than the occurrence of auroras. All observations were obtained along the same nightside orbit path evident in the pattern of parallel arcs stopping up to the right Geographic coverage was obtained by the rotation of the planet underneath on subsequent orbits with longitudes shifting $\sim 66°$ westward every orbit. It is possible that a large fraction of the nightside exhibited auroral emission during this orbit (from Schneider et al. 2015)

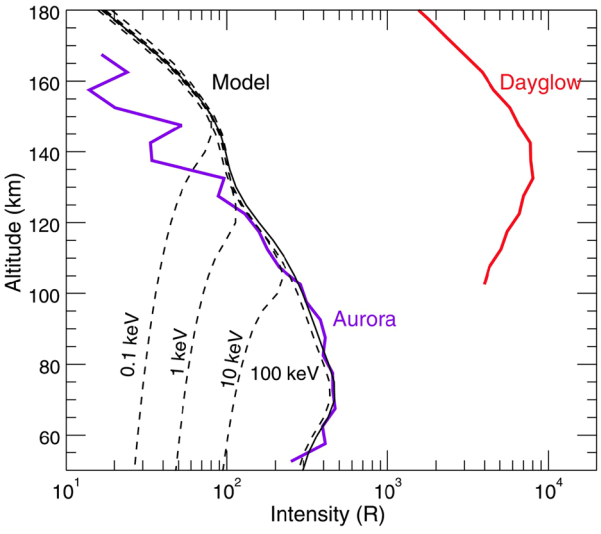


**Fig. 23** The red curve denotes the $CO_2^+$ UVD in the daylight near the terminator, the purple curve indicates the $CO_2^+$ UVD during auroras on the nightside. Whereas the photons that excite UVD emission on the dayside are absorbed at altitudes between 120 and 150 km. The energetic electrons that excite auroral emission penetrate nearly 60 km lower. The black curve shows the model emission profiles based on the SEP and SWEA data. Dashed lines show truncated energy distributions to illustrate how the maximum energy controls the depth of penetration (from Schneider et al. 2015)

of $CO_2^+$ UVD band is larger than the nighttime limb intensity of diffuse aurora by a factor of $\sim 20$. Both these emissions exhibit a broad peak at different altitudes.

## 5.2 Effects of CME and Magnetic Storms on Mars

During solar flares, high energy particles and plasma masses are emitted from the active region of the sun into the interplanetary space. These energetic streams produce violent disturbances in the Martian ionosphere. In this section we will review magnetic storm and ionospheric disturbances due to the impact of solar flares and CME/SEP on the atmosphere of Mars. Effects of solar X-ray flares on the ionosphere of Mars have been reported by several authors. For example, Nielsen et al. (2007) by using MARSIS ionospheric measurements,

reported a strong enhancement in the peak electron density from $1 \times 10^5$ to $3 \times 10^5$ $cm^{-3}$ at 08:39 UT on 15 September 2005. Mendillo et al. (2006) reported two electron density profiles, which increased about 200% due to solar X-ray flares on 15 April and 26 April 2001 at 13:50 UT and 13:10 UT respectively. Mahajan et al. (2009) reported effects of seven X-ray flares in the E and F1 regions of the Martian ionosphere. Fallows et al. (2015) examined all the electron density profiles observed by MGS and reported effects of 32 flares in the ionosphere of Mars. Based on MAVEN observations Elrod et al. (2018) reported heating of the upper atmosphere of Mars due to X-8.2 class flare on September 10, 2017. Recently Thirupathaiah et al. (2019) have studied the characteristics of all the flare effected electron density profiles (i.e. variations of electron density with respect to X-ray flux, SZA, solar longitude and latitude) obtained from radio occultation instrument onboard MGS during the period 24 December 1998 to 9 June 2005.

Venus-like diffuse aurora is observed/modeled in the northern hemisphere of Mars, which has neither a global magnetic field nor any crustal magnetic field (Fox 1992; Schneider et al. 2015; Haider and Masoom 2019). The effects of magnetic storms have also been detected in the Martian ionosphere at mid-to high northern latitudes. Haider et al. (2009, 2012) reported that the physical processes of magnetic storms are different on Earth and on Mars. During the magnetic storm on Earth the magnetosphere is compressed by shock waves driven by CME and the aurora is formed due to precipitation of high energy particles into the ionosphere. Mars does not have a dipole magnetosphere. However, magnetosheath is observed at about 435 km on the sunlit hemisphere of Mars during quiet conditions (Mitchell et al. 2000). During the magnetic storms at Mars the interplanetary shocks compress the magnetosheath to lower altitudes due to the impact of violent eruption of CMEs from the sun (Crider et al. 2005; Kallio et al. 2010; Lee et al. 2018). Using three dimensional kinetic solar wind model (Hakamada-Akasofu-Fry Version 2/HAFV.2) of Fry et al. (2003), Haider et al. (2012) confirmed the effect of magnetic storms on the Martian ionosphere, about 38 hours after the eruption of solar X-ray flare that occurred on 13 May 2005.

Vennerstrom (2011) examined seven years of MGS observations during solar maximum and early declining phase of solar cycle 24 to investigate the durations of magnetic storm events. They have reported that the magnetic storms can affect Mars' environment 20 to 40 hours after the eruption of CME from the sun. Morgan et al. (2014) reported a powerful CME impact on the Mars' ionosphere for the period 5 to 11 June, 2011. During this period the solar wind compressed the ionospheric plasma to lower altitudes mainly due to the enhancement in solar wind dynamic pressure. Luhmann et al. (2017) have also studied the effects of Martian magnetic storm on magnetic topology of Mars and the subsequent ionospheric changes. They used three dimensional global multispecies Magnetohydrodynamics (MHD) BATS-US-R model to reproduce the observed enhancement in the global ion escape rate reported by Jakosky et al. (2015) from MAVEN observations during CME event of March 2015. This model demonstrated how a combination of greatly enhanced solar wind pressure, magnetic field and convection electric field during a magnetic storm, can result in a strong solar wind-ionosphere coupling with important consequences in the upper atmosphere of Mars.

### 5.3 Observations of X-Ray Flares from MAVEN

Solar X-ray flares and CMEs driven shocks are considered to be the primary drivers of SEP events (Burlaga et al. 1991; Gopalaswamy et al. 2005). Figure 24a–b represents a time series of solar X-ray fluxes observed by GOES-15 (http://ngdc.noaa.gov/stp/satellite/goes/dataaccess.html) and LPW-EUVM instrument on board MAVEN (http://pds.nasa.gov) during the period 15–23 December, 2014. GOES 15 observes X-ray flux at wavelength band

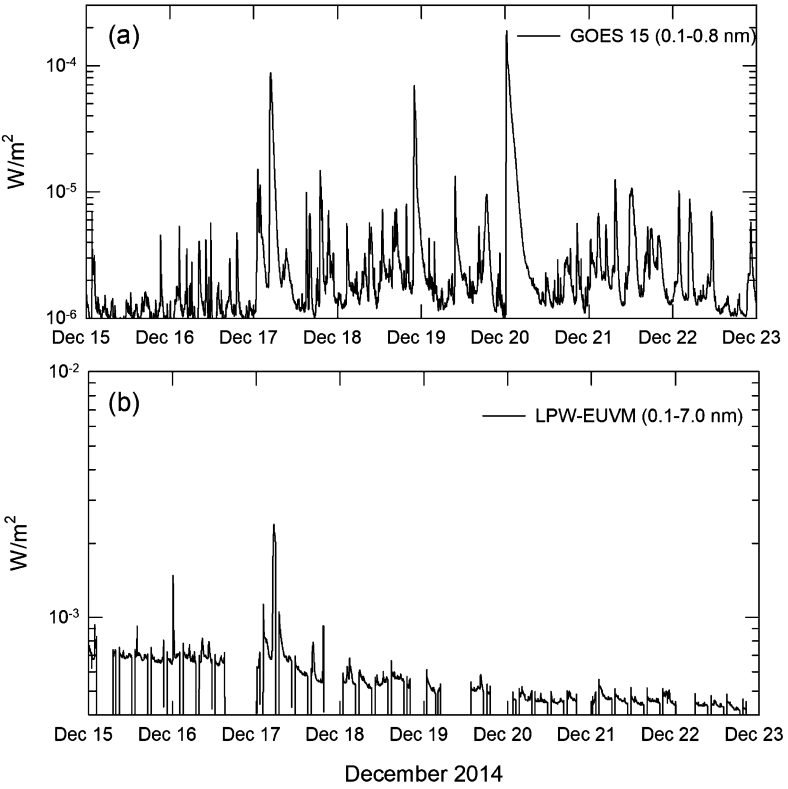


**Fig. 24** A time series of solar X-ray fluxes during December 15–23, 2014: (**a**) observed by GOES 15 (http://ngdc.noaa.gov/stp/satellite/goes/dataaccess.html) and (**b**) LPW-EUVM onboard MAVEN (http://pds.nasa.gov) instruments

0.1–0.8 nm while EUVM measures X-ray flux at wavelength band 0.1–7 nm. GOES 15 detected two M-class flares one on 17 and the other on 19 December 2014. It also detected one X-class flare on 20 December, 2014. Two most intense X-class flares were observed by EUVM on 16 and 17 December, 2014. The flare of 17 December, 2014 which peaked at about 04:42 UT was observed by both instruments. Figure 24b indicates some data gaps in EUVM observations before 17 and 20 December, 2014. These gaps are because the experiment was in safe mode and therefore no observations were carried out at that time. The diffuse auroras on Mars have been observed for a period of 5 days from 17 to 21 December 2014. The EUVM instrument onboard MAVEN observed two most intense X-class flares on 16 and 17 December 2014 at Mars before the occurrence of diffuse aurora. We would like to mention that flares do not cause aurora but that flares and SEP may have a common cause for auroral events.

### 5.4 Observations of SEPs from MAVEN

A SEP event occurred at Mars in December 2014 after the emission of a strong solar X-ray flare. Figure 25a–d shows a time series of SEP electron fluxes between energies 25 keV and 100 keV as observed by SEP instrument onboard MAVEN from 15 to 23 December, 2014 (Haider and Masoom 2019). These observations were carried out during 48 periapse

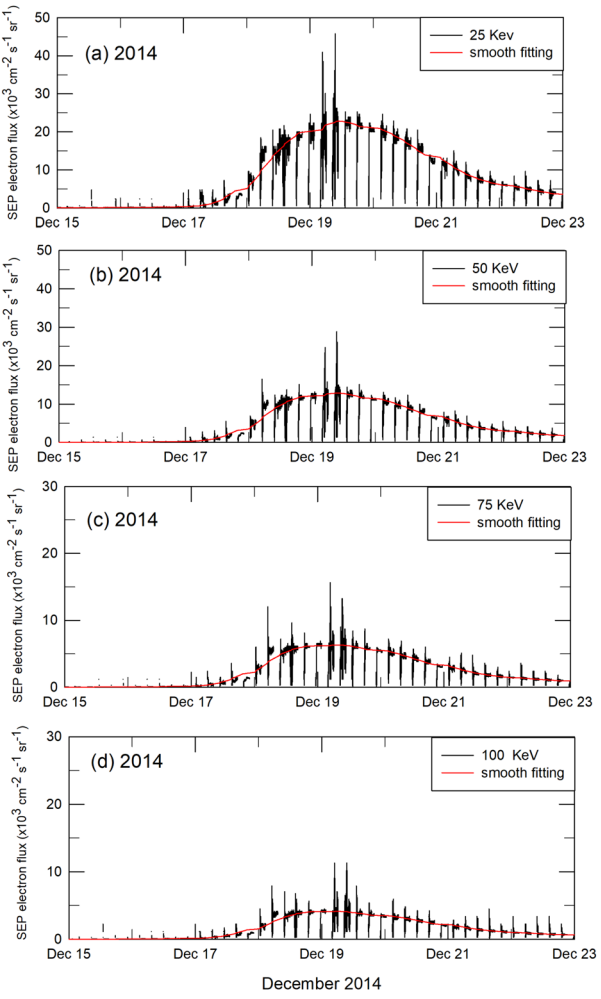


**Fig. 25** A time series of SEP electron fluxes at energies 25 keV (**a**), 50 keV (**b**), 75 keV (**c**) and 100 keV (**d**) as observed by SEP instrument onboard MAVEN during 15–23 December, 2014 (from Haider and Masoom 2019)

passes between orbits # 408 and 456. The data gap occurring in this figure is because we have plotted SEP electron fluxes at periapse passes only. These data sets are plotted without averaging over the orbit (thus all the data of a periapse pass are plotted for each orbit). The solid line represents smooth fitting obtained from 'Smooth Data Moving Average Filter' method (https://mathworks.com/help/curvefit/smooth.html/). The SEP instrument observes electron fluxes in forward and backward directions. We have plotted only the forward electron fluxes in Fig. 25a–d. The large enhancements in SEP electron spectra can be noted between 17 and 21 December, 2014 when diffuse auroras were observed by IUVS instrument. These spectra observed maximum electron fluxes $\sim 2.4 \times 10^4$, $1.3 \times 10^4$, $7.0 \times 10^3$ and $5.1 \times 10^3$ cm$^{-2}$ s$^{-1}$ sr$^{-1}$ at energies 25 keV, 50 keV, 75 keV and 100 keV respectively. The SEP peak electron fluxes were seen to decrease with increasing energy.

Figure 26 represents a time series of orbit-averaged solar wind plasma parameters obtained from SWIA and magnetometer instruments onboard MAVEN during SEP activity between 15 and 23 December, 2014 (Lee et al. 2017; Haider and Masoom 2019). The IMF fields changed at about 22:40 UT on 17 December, 2014 from anti-sunward to sunward

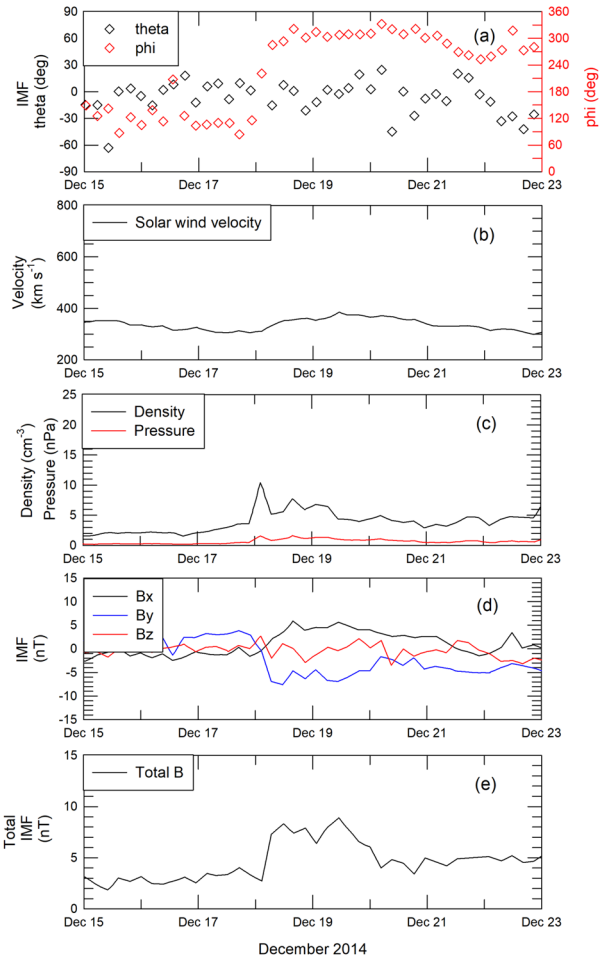


**Fig. 26** The orbit average solar wind plasma parameters between 15 and 23 December, 2014. First top panel: (**a**) IMF field directions, theta and phi in degrees; Second panel: (**b**) solar wind velocity in km/s; Third panel: (**c**) density and pressure in $cm^{-3}$ and nPa respectively; Fourth panel: (**d**) IMF field components $B_x$, $B_y$ and $B_z$; Fifth panel: (**e**) Total IMF field (from Haider and Masoom 2019)

directions at $\varphi = 120°$ to $\varphi = 300°$ respectively. Around the same time magnetic field components also rotated from $-B_x$, $+B_y$ to $+B_x$, $-B_y$. The angle (theta) is nearly zero when the magnetic fields are rotating from $x$ to $y$ components. This observation confirms that the heliospheric current sheets (HCS) were crossing at that time. After the HCS crossings SWIA observed a peak density of $\sim 15$ $cm^{-3}$ and peak pressure of 2.5 nPa at about 02:00 UT on 18 December, 2014. The total IMF field and solar wind speed also increased up to $\sim 9$ nT and $\sim 390$ km/s respectively between December 18 to 21, 2014. After this SEP event, the solar wind plasma and IMF values returned to their background levels.

The MAVEN has also observed SEP electrons (20–200 keV) arriving at Mars on 10 September 2017 3 h after the emission of a X8.2 class flare (Lee et al. 2018; Luhmann et al. 2018). During this event MAVEN/EUVM observed several additional X-class flares, which were not visible from Earth based satellite such as GOES or SDO (Chamberlin et al. 2018). The SEP electron fluxes produced by these flares, penetrated into the induced magnetic barrier and then precipitated into the Martian atmosphere, thereby driving heating, dissociation, and ionization rate (Ramstad et al. 2018). Xu et al. (2018) investigated magnetic topology response to the 2017 September ICME event. They observed the deepest IMF penetration over

northern hemisphere down to altitude as low as 200 km due to enhanced solar wind dynamic pressure during the periapsis passage. This event caused global diffuse aurora in the nighttime of Mars (Schneider et al. 2018). Harada et al. (2018) investigated Martian nightside ionosphere during the September 2017 SEP event from MEX/MARSIS instrument together with the MAVEN dayside observation. They concluded that this was a very high solar dynamic pressure event. Sánchez-Cano et al. (2019) observed a blackout in MEX/MARSIS and Mars Reconnaissance Orbiter (MRO)/Shallow Radar (SHARAD) signals during this event, probably caused by a signal absorbing transient ionization layer formed at lower altitudes.

## 6 Mechanisms of Nighttime Aurora

Since Mars has no dipole magnetic field, the physical processes of Mars' aurora are different from Earth's aurora. Fox (1992) argued that Mars should have Venus-like aurora because both planets have induced magnetosphere with similar composition of atmospheric gases. Auroral particles have shown important effects on the atmosphere beside the excitation of the auroral spectrum. These include the enhanced heating rates and the production of strong ionization. Auroral ionization is responsible for increasing electron density, electrical and thermal conductivity in the Mars' atmosphere. There are several acceleration mechanisms, which participate in the production of auroras. Brain and Halekas (2012) reported that the electrons are partly accelerated downward into the Martian atmosphere by quasi-stationary field aligned potential. A variety of additional mechanisms may also be contributing to aurora, including the day to night transport of ionospheric particles, wave reconnection and particle acceleration in the magnetotail current sheet.

### 6.1 Day to Night Transport of Photoelectrons

Figure 27a illustrates the transport of dayside photoelectrons into the nightside ionosphere across the terminator and formation of discrete aurora in the mini-magnetosphere of Mars. In this region IMF field lines are mostly connected between dayside and nightside ionosphere of Mars (Weber et al. 2020). Leblanc et al. (2006, 2008) reported peak electron energy range of discrete aurora from 40 eV to 350 eV. They argued that auroral emissions are produced, most probably, by electrons with energy distribution peaking at few tens of eV rather than by those electrons peaking above 100 eV. Based on 3-D MHD modeling of the magnetic field draping around Mars, Liemohn et al. (2007) also reported that, most likely, electrons which produced the observed UV aurora emission were non-accelerated magnetosheath electrons rather than photoelectrons.

### 6.2 Inverted 'V' Potential Structures

Most of the observations presented in Sect. 3 are consistent with the existence of quasi-static field aligned potentials above the cusp regions on the Martian nightside (Fig. 27b). This process is similar to terrestrial auroral particle acceleration, where peaked 'inverted – V' particle energy distributions are reminiscent of charged particles observed in the field-aligned current regions at Earth (Lundin et al. 2006; Dubinin et al. 2008; Marklund 2009; Fillingim et al. 2012; Ip 2012; Xu et al. 2020). In order to sustain this mechanism on Mars, strong parallel electric field is required for the drop in field aligned potential above the ionosphere. Dubinin et al. (2008) calculated parallel electric fields for different potential drop structures on Mars. They found that the potential drop increases with ionospheric electric

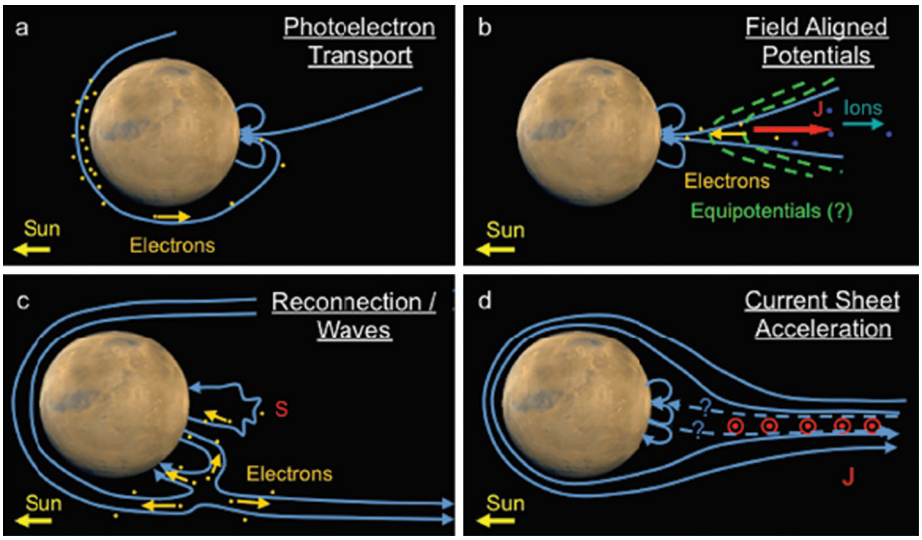


**Fig. 27** Schematic representations of various mechanisms for the formation of the nighttime aurora at Mars: (**a**) Formation of discrete aurora in the mini-magnetosphere of Mars due to transport of photoelectrons from dayside to nightside atmosphere across the terminator, (**b**) Inverted 'V' potential structure can be created above the cusp region on the Mars nightside aurora in presence of strong electric fields, (**c**) The magnetic reconnection process is proposed in the magnetotail of Mars for high energy electron precipitation in the nighttime atmosphere of Mars, and (**d**) The current sheet of Mars' magnetotail is also thought to provide access for the accelerated electrons to the nightside aurora (from Brain and Halekas 2012)

field. The auroral electric field increased up to a few mV/m for a larger potential structure of $\sim$ 100 km. The electric and magnetic field strengths are very low in the ionosphere of Mars, in comparison to Earth's ionosphere. Therefore, relatively small potential drops can appear in the presence of strong crustal fields when the magnetosphere and ionosphere are decoupled by a zone with strong parallel electric field. Ip (2012) also proposed a 'V' shaped potential structures, where electrons are precipitating downward and conic ions were escaping upward in the presence of strong crustal magnetic fields. He suggested that only those ions which are created in the crustal fields and connected to IMF field lines would be able to escape. The ions which are created in the magnetic flux tubes of close field lines will be trapped in a bouncing motion. Recently Xu et al. (2020) have also identified V electron events from late February to March 2019, when MAVEN observed aurora near periapsis over Mars' southern strong crustal fields. During this event the field aligned potentials increased up to $\sim$ 440 volt from electron observations. They have calculated maximum upward current density $\sim$ 2.5 $\mu A/m^2$, where inverted V electron acceleration events occurred.

### 6.3 Magnetic Reconnection and Waves

It should be noted that field aligned potential drops are not the only mechanisms for particle acceleration in the nighttime aurora. The magnetic reconnection is also reported to contribute to the nightside aurora (Eastwood et al. 2008; Brain and Halekas 2012; Luhmann et al. 2017). This process occurs when IMF field lines are coupled with crustal field lines and the new field lines are connected to Mars and open to space. The MAVEN observations and simulations have indicated that Martian magnetotail is twisted due to magnetic

reconnection (Brain et al. 2015; Dong et al. 2015). In this process high convection electric field $E = -\text{VXB}$ is produced at the magnetosphere – ionosphere boundary (Luhmann et al. 2017). Figure 27c taken from Brain and Halekas (2012) shows a schematic of mechanism for the electron entry into the nightside ionosphere of Mars due to wave acceleration in the magnetic reconnection region. This mechanism produces electron conic pitch angle distribution, which provides a source of energy for electrons passing from the reconnection diffusion region (Ulusen et al. 2011).

### 6.4 Current Sheet of Mars' Magnetotail

The configuration and stability of the Mars' magnetotail current sheet depends on the ratio of plasma pressure to magnetic field pressure ($\beta$) and Mach number (M). Artemyev et al. (2017) have analyzed more than 200 current sheet crossings in Mars' magnetotail to study these parameters and compared them with the Earth's magnetotail parameters. They found that Mars' magnetotail current sheet occupies much wider range of these parameters than Earth's magnetotail current sheet. It is not clear whether or how the observed current sheets provide access for accelerated electrons to the nightside aurora at Mars. Therefore, the solar wind parameters observed by MAVEN in the current sheet makes this region very important for detailed investigations of how various dynamical processes (magnetic reconnection, particle acceleration etc.) depend on current sheet location and configuration. Figure 27d represents an intriguing mechanism of acceleration for electrons in the current sheet on Mars' nightside atmosphere. All the four mechanisms shown in Fig. 27a–d can occur on Mars and contribute to the occurrence of nightside auroras.

## 7 Modeling Experiments of Martian Aurora

As mentioned before, several mechanisms are contributing to Martian auroras, including day-night transport of SEP and CME electrons, ENAs precipitation, waves and reconnection and particle acceleration in the magnetotail current sheet. The understanding of these mechanisms requires a balanced effort in theoretical modeling and analysis of the observations. The theoretical models based on fundamental principles in conjunction with data obtained from recent Mars missions are important to improve our understanding of physical, chemical and dynamical processes of the aurora. To help in strengthening this area of research, we review various models of Martian aurora. This will help to distinguish between the different mechanisms, constrains the variation in auroral acceleration and brightness at different wavelengths, correlate auroral activity with external conditions, and determine the importance of auroral processes for atmospheric electrodynamics and atmospheric escape. In the following, we review the various plasma and auroral emission models that are currently used in the simulation of observed Martian auroral features. Plasma models provide the external conditions (e.g. precipitating electron, proton and ENA fluxes; acceleration mechanisms, etc) that drive auroral emission models. Both are important for this review.

### 7.1 Plasma Models

The basic capabilities and limitations of different types of plasma models, including those commonly utilized for Mars studies, along with the electromagnetic equations solved, are thoroughly reviewed in Ledvina et al. (2008). In the following we give a brief review of these plasma models.

### 7.1.1 Hybrid Model

The hybrid model has been used by several investigators (Kallio and Janhunen 2001; Kallio and Barabash 2001; Haider et al. 2002, 2013; Haider and Masoom 2019). In this model $H^+$ ions are accelerated up to energies 10 keV in the presence of electric and magnetic fields as given below:

$$\frac{d\boldsymbol{V}_i}{dt} = \frac{q_i}{m_i}(E + V_i X B) + \frac{F_i}{m_i} \tag{1}$$

where $\boldsymbol{V}_i$, $m_i$, and $q_i$ are velocity, mass, and charge of an $i_{\text{th}}$ ion respectively. $\boldsymbol{F}$ is a Lorentz force. In this model magnetic field $\boldsymbol{B}$ is calculated by Faraday's law. The electric field $\boldsymbol{E}$ is calculated from electron momentum equation as follows:

$$E = -u_e X B - \frac{\nabla p_e}{e n_e} \tag{2}$$

where $\boldsymbol{u}_e$ is the bulk velocity with pressure gradient $\nabla p_e = K_B T_e \nabla n_e$, $T_e$ is the electron temperature, $K_B$ is a Boltzmann constant, and $n_e$ is the electron density. The term $\boldsymbol{u}_e$ is calculated from the current density $\boldsymbol{J}$ as follows

$$u_e = \frac{\sum_i q_i n_i u_i}{e n_e} - \frac{J}{e n_e} \tag{3}$$

In Eq. (3) the electric current density J is derived from the Ampère law. Under quasi-neutrality condition the electron density $n_e$ is equal to the total density of positive ions $n_e = \frac{\sum_i q_i n_i}{e}$.

Since Mars has no dipole magnetic field (Acuña et al. 1998), the interplanetary shock compresses the magnetosheath of Mars during the auroral events. In the magnetosheath, the planetary neutrals are mainly H atoms of the hydrogen corona. In this region, ENAs are produced by charge exchange between solar wind protons and hydrogen corona. An ENA is the product of $H^+$ and H (Galli et al. 2008) and can be represented as $H^+$-H.

In the Hybrid-model atmospheric effects of ENAs precipitation are included by Monte Carlo simulation (Kallio and Barabash 2001; Kallio and Janhunen 2001). Haider and Masoom (2019) modeled limb intensity profiles of diffuse aurora due to precipitation of ENAs and SEP monoenergetic electrons (25 keV, 50 keV, 75 keV and 100 keV) for the nightside ionosphere of Mars. Figure 28 represents the comparison between observed and modeled profiles of limb intensities of $CO_2^+$ UVD in the nighttime ionosphere of Mars. This result shows that the SEP electrons of 100 keV are enough to produce the observed peak limb intensity at about 75 km, the altitude where MAVEN observed nighttime auroral emissions. However, the observed SEP flux cannot reproduce complete profile of the observed UV emission. In the upper ionosphere the observed limb intensity is produced due to ENA precipitation into the nighttime ionosphere.

It should be noted that Kallio and Janhunen (2001) developed the Hybrid model for the three gases $CO_2^+$, $N_2^+$, and $O^+$ only. The production rates of $O_2^+$ and $CO^+$ play a very important role in the chemistry of auroral ionosphere. Therefore, this model should be extended to other ions also. However, there are several advantages of this model, which are: (1) It is a three dimensional model which is useful for solar wind interaction with Mars, (2) It includes kinetic effects of plasma, wave particle interaction and plasma instabilities, and (3) It is a self consistent model in which plasma is traveling in the presence of electric and magnetic fields in accordance with Maxwells equation.

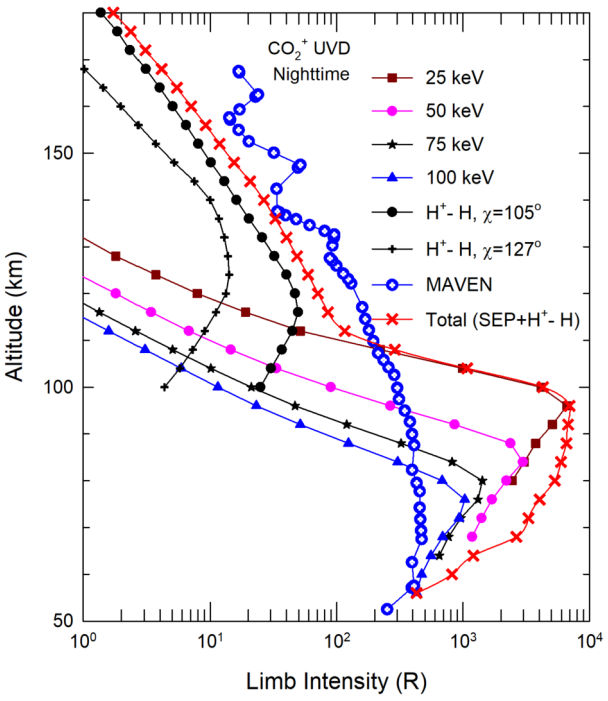


**Fig. 28** The limb intensities of $CO_2^+$ UVD due to impact of $H^+$-H at SZA 105° and 127° and SEP electron impact at energies 25 keV, 50 keV, 75 keV and 100 keV in the nighttime ionosphere of Mars. The estimated results are compared with the observed profile of $CO_2^+$ UVD obtained from MAVEN when diffuse aurora occurred on Mars (from Haider and Masoom 2019)

### 7.1.2 MHD Model

The MHD model has been developed to study solar wind-Mars interaction, auroras, magnetic storms and ion escape from Mars (Liemohn et al. 2007; Brain et al. 2010; Andrews et al. 2016; Ma et al. 2004, 2017; Regoli et al. 2018; Luhmann et al. 2017). The different forms of MHD have been reported viz. *ideal* MHD, *multispecies* MHD, *Hall* MHD, and *multi fluid* MHD models. The *ideal* MHD model can be understood by continuity, momentum and energy equations as well as Faraday's law as given below:

*Continuity Equation*

$$\frac{\partial \rho}{\partial t} + \nabla.(\rho u) = P - \rho L \tag{4}$$

*Momentum Equation*

$$\rho\left(\frac{\partial}{\partial t} + u.\nabla\right)u = J \times B - \nabla.p \tag{5}$$

*Energy Equation*

$$\frac{\partial \varepsilon}{\partial t} + \nabla.(\varepsilon u) = -\rho \nabla.u \tag{6}$$

*Faraday's Law*

$$\frac{\partial B}{\partial t} = -\nabla \times E \tag{7}$$

where $\boldsymbol{u}$ is bulk plasma velocity, $\boldsymbol{\rho}$ is plasma density, $\boldsymbol{p}$ is pressure, $\boldsymbol{\epsilon}$ is energy, $\boldsymbol{E}$ is electric field, $\boldsymbol{B}$ is magnetic field and $\boldsymbol{J}$ is current density. The production and loss term of Eq. (4) is generally taken equal to zero in MHD simulation. The different forms of MHD models have been used by using different forms of Ohm's Law. In ideal MHD model, ideal Ohm's law ($\mathbf{E} = -\mathbf{u} \times \mathbf{B}$) is used. Hall MHD includes Hall term ($\sim \mathbf{J} \times \mathbf{B}$) in Ohm's law. In multispecies MHD model several ion species are considered. BATS-R-US MHD model is a multispecies version (Luhmann et al. 2017). In *multi fluid* MHD model plasma is modeled as a fluid. MHD model is also developed into one, two and three dimensions to study the dynamics of the auroral ionosphere of Mars. All MHD models assume a Maxwellian velocity distribution function. Recently the response of ICMEs at Mars was observed by MAVEN during March 2015 (Jakosky et al. 2015). Using BATS-R-US (MHD) model Luhmann et al. (2017) studied the effect of magnetic storm due to ICME impact on Mars. They found that solar wind pressure, magnetic field and electric field combine produced strong magnetospheric coupling with important consequences in the upper atmosphere and ionosphere energization. Due to limitation of computational resources, the simplest *ideal* form of MHD model is used to study the auroral phenomena caused by energetic particle precipitation from the cusp region into the nightside atmosphere of Mars (Mauk and Bagenal 2012; Luhmann et al. 2017).

## 7.2 Auroral Emission Models

### 7.2.1 Monte Carlo Model

In the Monte Carlo model a random number between 0 and 1 is generated to determine whether a collision takes place or not. If not, the amount of energy lost through Coulomb losses to the ambient electrons is calculated from Butler-Buckingham formula (Dalgarno et al. 1963) and is added to the accumulated energy loss. If the collision with atmospheric gases occurs, a further decision is made whether the collision is elastic or inelastic. The one dimensional Monte Carlo model is used by several investigators to study the electron excitation, ionization and airglow processes in the planetary atmospheres (Ip 1998; Singhal and Bhardwaj 1991; Bhardwaj and Michael 1999; Bhardwaj and Jain 2009). This method is also used to solve the Boltzman transport equation for the dayglow and auroral emissions integrated along the line of sight and compares well with the limb profiles observed by SPICAM and IUVS instruments onboard MEX and MAVEN respectively (Shematovich et al. 2008; Gérard et al. 2015, 2017; Bisikalo et al. 2017, 2018).

A three dimensional Monte Carlo model is used for the formation of aurora due to ENAs ($H^+$-H) precipitation into the atmosphere of Mars (Kallio and Barabash 2001; Kallio and Janhunen 2001; Haider et al. 2002, 2013; Haider and Masoom 2019). This model includes 6 elastic and 24 inelastic collision processes (ionization, electron stripping, charge exchange, Lyman-$\alpha$, and Balmer-$\alpha$) between energy 10 eV and 10 keV for the impact ionizations of $H^+$-H with atmospheric gases (Haider et al. 2002). The energy losses and the number of collisions are recorded into different matrices which give production rates at different altitudes and SZA (Haider et al. 2002; Haider and Masoom 2019). Deighan et al. (2018) modeled limb intensity profiles of proton aurora observed by IUVS instrument onboard MAVEN due to precipitation of ENA flux ($1–3 \times 10^6$ cm$^{-2}$ s$^{-1}$) in the dayside atmosphere of Mars. Figure 29 represents altitude profiles of limb intensities of proton aurora compared with model and IUVS observations carried out on 8 March, 1 and 3 April 2015 at SZA 66°, 66° and 62° during orbits # 850, 975 and 986 respectively.

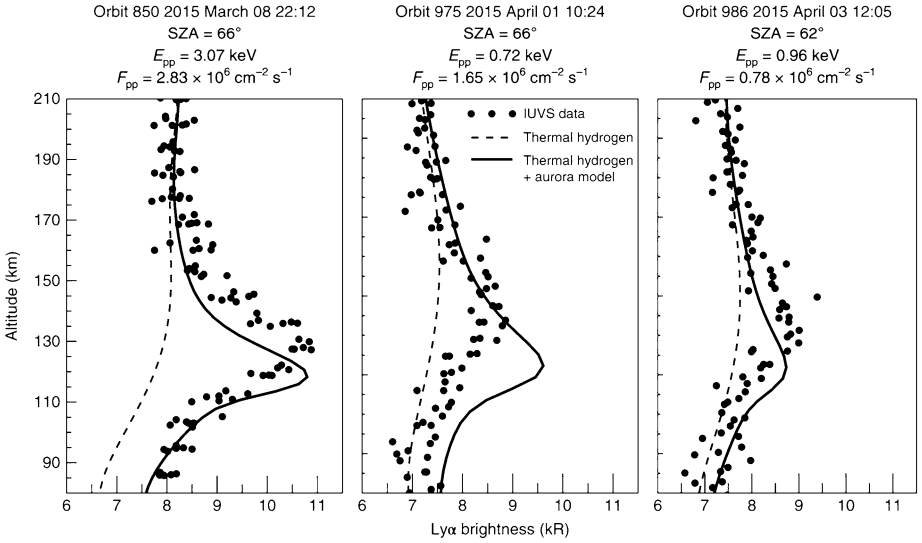


**Fig. 29** Observed and modeled Ly $\alpha$ brightness. Symbols indicate limb observations made by the IUVS, dashed lines are estimated fluorescent scattering by thermal hydrogen using nearby orbits that lack a peak and solid lines are aurora model output guided by SWIA measured penetrating proton characteristics. The SZA of the limb scan as well as the proton energy and proton flux at the top of each plot are given (from Deighan et al. 2018)

### 7.2.2 AYS Approach

The AYS approach is based on the Monte Carlo method. In this technique electrons of different incident energies $E_o$ are introduced at the top of the atmosphere (Singhal et al. 1980; Haider and Singhal 1983; Bhardwaj et al. 1995; Haider et al. 2013). These electrons are precipitating down into the Martian atmosphere along the IMF lines at some pitch angle. The IMF field lines are draped through the atmosphere of Mars in the absence of dipole magnetosphere. The primary incident electrons produce secondary and tertiary electrons of energy $E$ at position $r$ and $Z$ after the collision with the atmospheric gases. The $r$ and $Z$ are the radial and longitudinal distances where $r = (x^2 + y^2)^{0.5}$. It is assumed that the secondary electrons of energy E are ejected isotropically. In this way two, three and four dimensional yield spectrum viz. $U(E, E_o)$, $U(E, Z, E_o)$ and $U(E, r, Z, E_o)$ are developed to study the electron energy degradation processes in planetary atmospheres. The two dimensional yield spectrum $U(E, E_o)$ is used where the magnetic field is uniform and horizontal in direction (Haider and Singhal 1983; Bhardwaj et al. 1990; Seth et al. 2002; Haider et al. 2006, 2010; Haider and Mahajan 2014; Thirupathaiah et al. 2019). In this case, the electrons lose their energy at the location where they are produced and the vertical transport of the electrons is inhibited. The three dimensional yield spectrum $U(E, Z, E_o)$ is used where the magnetic field is in vertical direction and the electrons do not lose their energy locally (Singhal and Haider 1984; Haider 1997; Haider et al. 2002; Haider et al. 2010, 2013). The four dimensional yield spectrum $U(E, r, Z, E_o)$ is used where the motion and spatial extent of auroral electron precipitations are considered along the magnetic field lines (Haider and Singhal 1983, 1986; Bhardwaj et al. 1996; Haider and Bhardwaj 2005; Haider and Masoom 2019). The yield spectra calculate the yield of any state in the mixture of gases. In three and four dimensional yield spectrum model, the functions for $Z < 0$ and $Z > 0$ represent the up-

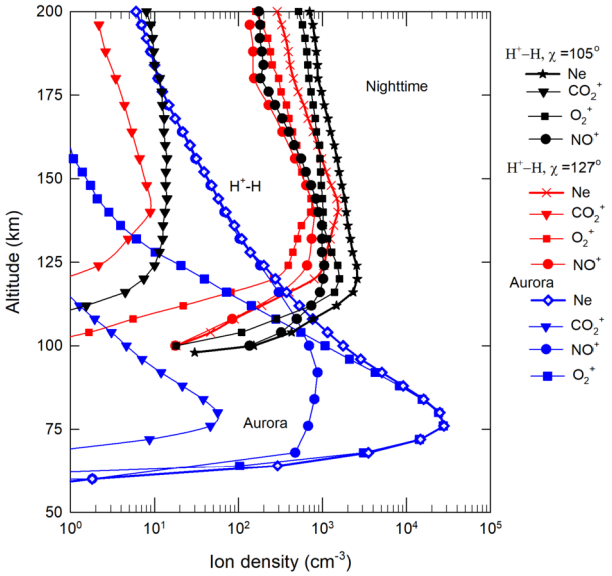


**Fig. 30** The ion densities of $CO_2^+$, $O_2^+$ and $NO^+$ due to impact of SEP electrons of 100 keV and $H^+$-H impact at SZA 105° and 127° in the nighttime ionosphere of Mars. The electron density (Ne) due to impact of $H^+$-H and SEP electrons of 100 keV are also plotted in this figure (from Haider and Masoom 2019)

ward and downward precipitating SEP electrons respectively. Recently Haider and Masoom (2019) have used four dimensional yield spectra (for $Z > 0$) to study the diffuse aurora on Mars (see Fig. 28). This method depends on elastic and inelastic cross-sections, model atmosphere, and solar EUV flux. The results using this model are uncertain by a factor of $\sim 2$ depending on the values used for the cross sections (Haider et al. 2002; Kallio et al. 2010).

The time dependent continuity and momentum equations are given in the MHD model (see Sect. 7.1.2 and Eq. (4)). This equation can be solved separately for ionospheric densities (Shinagawa and Cravens 1989; Fox et al. 1993; Fox and Yeager 2009; Schunk and Nagy 2009; Haider et al. 2010, 2013; Pandya and Haider 2014; Haider and Masoom 2019). The production can be obtained from chemical reactions, photoionization, photoelectron impact ionization rate or collisional ionization due to precipitation of auroral electrons, SEP electrons or ENAs particle ($H^+$-H) into the Martian atmosphere. The loss rate is due to chemistry of various reactions. The differential equations can be solved by the finite difference method using lower and upper boundary conditions. At lower boundary chemistry plays the major role and we can take initially a minimum value of electron density for iteration at lower height. At upper boundary plasma is under diffusive equilibrium and diffusion flux is nearly constant with height. In the Martian ionosphere, the chemical life time $\tau_c = L^{-1}$ is much smaller up to 200 km than the molecular diffusion time constant $\tau_m = H_i^2/D_i$, where $H_i$ is the plasma scale height and $D_i$ is the plasma diffusion. Thus, the plasma diffusion can be neglected below this altitude. For the steady state condition, $\frac{\partial n_i}{\partial t} = 0$, then $p_i = \rho_i L_i$. Under the equilibrium conditions the sum of the positive ion densities is equal to the electron density ($\Sigma\rho_i = \rho_e$).

Figure 30 represents a comparison of ion as well as the electron densities ($CO_2^+$, $O_2^+$, $NO^+$, and $N_e$) in the upper and middle ionosphere of Mars resulting due to precipitation of $H^+$-H and SEP electrons respectively. These comparisons were done for SZA $\sim$ 105° and SZA $\sim$ 127° to represent two nighttime conditions. Haider and Masoom (2019) found that the $H^+$-H impact ionizations do not provide as substantial source of ionization in the upper ionosphere as SEP electrons provide in the middle ionosphere. In these calculations Hybrid model, AYS approach and couple continuity equations have been used. The peak densities

of $O_2^+$, $NO^+$ and $CO_2^+$ are estimated to be $1 \times 10^3$ cm$^{-3}$, $8 \times 10^2$ cm$^{-3}$ and $1 \times 10^1$ cm$^{-3}$ at altitudes 140 km, 135 km and 138 km respectively due to $H^+$-H impact ionizations at SZA 127°. At SZA 105°, the peak altitudes of these ions are lowered by 10–15 km and their peak densities were increased by a factor of $\sim 2$. The peak electron densities are estimated to be $\sim 3.3 \times 10^3$ and $1.2 \times 10^3$ at SZA 105° and 127° respectively due to $H^+$-H impact ionizations. The peak densities of $O_2^+$, $NO^+$ and $CO_2^+$ due to precipitation of auroral electrons of 100 keV were estimated to be $3 \times 10^4$ cm$^{-3}$, $10^3$ cm$^{-3}$ and 65 cm$^{-3}$ at altitudes 75 km, 90 km and 80 km respectively.

### 7.2.3 Boltzmann Kinetic Transport Model

The photoelectron and auroral electron lose their excess kinetic energy after collision with the atmospheric gases. Their kinetics and transport are described by Boltzmann transport equation:

$$u\frac{\partial f_e}{\partial r} + s\frac{\partial f_e}{\partial u} = Q_{e,p}(u) + Q_{e,s}(u) = \sum_m J(f_e, f_m) \tag{8}$$

where $\boldsymbol{s}$ is the acceleration due to gravity, $\boldsymbol{f}_e(\boldsymbol{r}, \boldsymbol{u})$ and $\boldsymbol{f}_m(\boldsymbol{r}, \boldsymbol{u})$ are the velocity distributions of electrons and species respectively. In Eq. (8) the first and second terms represent the radial and velocity distributions of the electrons. The left side of the kinetic equation describes the transport of the electrons in planetary gravitational field $\boldsymbol{s}$. In the right side of the kinetic equation the terms $Q_{e,p}$ $(\boldsymbol{u})$ and $Q_{e,s}$ $(\boldsymbol{u})$ represent productions due to photoionization and secondary electrons respectively. The term $J(f_e, f_m)$ represents scattering due to electron collisions with the atmospheric gases $\boldsymbol{m}$ (= O, $CO_2$, $N_2$ and CO). Shematovich et al. (1994, 2008) used the Direct Simulation Monte Carlo (DSMC) method to solve the Boltzmann kinetic equation. Recently this model has been used to calculate the auroral emission intensities of hydrogen Lyman-$\alpha$ (121.6 nm), $CO_2^+$ UVD at 288.3 and 289.3 nm and the Fox-Duffendack-Barker (FDB) bands, CO Cameron and Fourth Positive bands, OI 130.4 and 297.2 nm and CI 156.1 nm and 165.7 nm multiplets (Soret et al. 2016; Gérard et al. 2017, 2019; Bisikalo et al. 2017; Shematovich et al. 2019).

The Boltzmann kinetic transport model is solved by the DSMC method using the stochastic approximation (Shematovich et al. 2008). In this method various elastic and inelastic cross sections are also used due to collisional processes. The values of cross sections used by various investigators are not consistent with each other and a factor of 2–3 variations can be seen among the values used. Therefore the result using the Boltzmann kinetic transport model are uncertain by a factor of $\sim 2$, depending upon whether the various cross sections were obtained from the models or from the observations. This model is used by Shematovich et al. (2008) and Gérard et al. (2017) to compare the auroral emissions observed by SPICAM and IUVS instruments onboard MEX and MAVEN in the nightside and dayside atmosphere of Mars respectively. In Table 2 we have given a summary of models used for Mars' auroras (It should be noted that these theoretical models can be used for any research problems including auroras. Therefore, we do not conclude which model is good or bad. However, based on author's conclusions in their papers, we have categorized the performances of various auroral models).

## 8 Discussion

The first observation of aurora at Mars was carried out in August 2004 by SPICAM instrument onboard MEX in the nighttime ionosphere of Mars in the crustal magnetic field region

**Table 2** Summary of models used for Mars' auroras

| Types of Aurora | Models used | Agreement between models and observations |
|---|---|---|
| Discrete Aurora | Boltzmann-Kinetic Transport, Monte Carlo, MHD | Reasonable[a,b,c,d] |
| Proton Aurora | Monte Carlo, Boltzmann-Kinetic Transport | Reasonable[e,f] |
| Diffuse Aurora | Monte Carlo, AYS, Hybrid | Good[g,h] |

[a]Soret et al. (2016) [b]Luhmann et al. (2017) [c]Shematovich et al. (2011) [d]Leblanc et al. (2006) [e]Deighan et al. (2018) [f]Gérard et al. (2019) [g]Haider and Masoom (2019) [h]Gérard et al. (2019)

(Bertaux et al. 2005). Later additional auroral events have been reported by Leblanc et al. (2008), Gérard et al. (2015) and Soret et al. (2016) in the mini-magnetosphere of Mars.

Recently MAVEN has observed three types of auroras: (1) discrete aurora (Schneider et al. 2018), (2) Proton aurora (Deighan et al. 2018), and (3) diffuse aurora by the IUVS instrument (Schneider et al. 2015, 2018). We have reviewed in the preceding sections experimental results of these auroras. A variety of physical and chemical processes and theoretical models of Martian auroras were also reviewed. These auroras are also found in the Earth's atmosphere. The discrete aurora is observed within the Earth's auroral ovals around magnetic poles. This aurora is powered by the combination of parallel electric field and plasma waves that accelerate the precipitating particles into the atmosphere of Earth. A second type of aurora is observed equator ward of the auroral zone (Lui et al. 1973). It occurs in a much wider spatial range. It is produced from the particles scattered into the Earth's atmosphere. The third type of aurora is known as 'polar rain' aurora, which occurs in the pole ward of the auroral oval due to solar wind particle precipitation but without local acceleration. Normally, diffuse auroras are fainter than the discrete aurora. It should be noted that these terrestrial auroras are confined to the polar region with an emission peak in the upper atmosphere (Schneider et al. 2015).

By contrast, the discrete auroras on Mars are observed in the regions of mini-magnetospheres due to precipitation of electrons of few keV, which were most likely accelerated by parallel electric fields similar to those observed on the Earth's discrete aurora. The diffuse aurora occurs on Mars at low altitude $\sim 70$ km (Schneider et al. 2015). In Fig. 31 we have shown a comparison of field lines configuration for diffuse and discrete auroras on Earth and Mars. This figure represents the very different magnetic field lines structures on Mars and on Earth. The discrete aurora on Earth occurs at a high latitude region of closed field lines connected to the planet on both ends. A similar region also occurs at Mars in the mini-magnetosphere to produce discrete aurora. Both auroras are powered by electrons accelerated at the sun and not locally at the planet. These electrons collide with the Earth's atmosphere along the open field lines in the auroral oval. The magnetic field lines of Mars are open or draped which allow ENAs and SEP electrons to precipitate into the atmosphere during solar storms. These particles are 100 times more energetic than those producing discrete auroras (Schneider et al. 2015). The IMF field lines are mostly open and cover much of the planet. Therefore diffuse aurora on Mars occurs everywhere on the planet.

## 9 Summary and Conclusions

In this paper we have reviewed three types of auroras that were observed by instruments onboard MEX and MAVEN as follows:

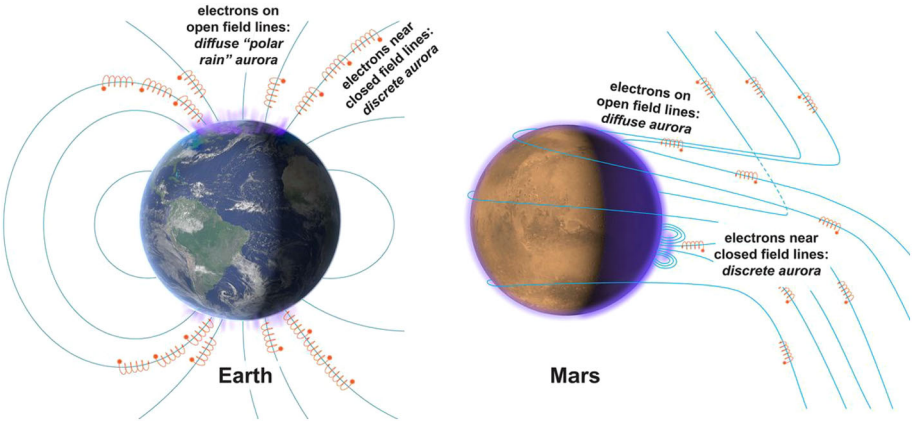


**Fig. 31** Comparison of magnetic field geometry for diffuse and discrete auroras on Earth and Mars: Mars lacks of global dipole magnetic field due to cooling of its core. Fields surrounding Mars are the combination of small structures locked in the crust billions of years ago (lower right) and solar wind field lines draped around the planet (from Schneider et al. 2015)

- The discrete aurora: By MEX at wavelengths 181.0 nm and 298.0 nm during the nighttime due to electron precipitation at energy $< 1$ keV in the southern mini-magnetosphere. Also by MAVEN at wavelength 289.0 nm due to electron precipitation in the nighttime southern hemisphere during space weather events of September 2017.
- The proton aurora: By MEX and MAVEN during the daytime at wavelength 121.6 nm due to precipitation of ENAs.
- The diffuse aurora: By MAVEN at wavelengths 288.3 nm and 289.6 nm due to high energy electron precipitation at $\sim 100$ keV during the CME/SEP event of December 2014.

These observations are strongly related to the sensitivity of the instruments used to observe them and were carried out in the northern and southern hemispheres of Mars in the absence as well as in the presence of strong crustal magnetic fields (Bertaux et al. 2005; Brain et al. 2010; Schneider et al. 2015, 2018). Several investigators have modeled these experimental results of auroras (Leblanc et al. 2008; Haider et al. 2009; Schneider et al. 2015; Gérard et al. 2015; Soret et al. 2016; Luhmann et al. 2017; Deighan et al. 2018; Haider and Masoom 2019) and therefore, we have also reviewed these modeling results. It needs to be mentioned that the auroras observed on Mars were not seen by naked eyes. The visible auroras are yet to be observed at Mars. Although it is not very clear why the visible auroras are not detected on Mars, we think this could be due to the following reasons: (1) The relevant transitions are not sufficiently excited to create visible aurora or (2) The available instruments are not sensitive enough to distinguish the visible emissions from the UV emissions and a new experiment needs to be designed for such emissions. The present review paper emphasis the need to design a future payload for detecting the visible aurora on Mars similar to that observed on Earth.

Six missions including EMM, Mars Perseverance Rover, Rosalind Franklin Rover, Mars global remote sensing Orbiter, Lander and Rover, MOM-2 and MMX are in the pipelines to explore Mars. Among six missions the objectives of EMM and MOM-2 are to address key science questions on Mars' upper atmosphere, aurora, ionosphere, magnetic field, hot oxygen corona, solar wind interaction and escape to outer space. The present review covering topics associated with the auroral activity on Mars will be very helpful for planning of future

Mars missions. We have also reviewed five important theoretical plasma and emission models of the Martian aurora which are: (1) Hybrid Model, (2) MHD Model, (3) Monte Carlo Method, (4) AYS Approach, and (5) Boltzmann Kinetic Transport Model. These models have some advantage and disadvantage in their applications and results and these aspects have also been discussed.

**Acknowledgements** One of the authors S. A. Haider is thankful to DST/SERB for providing him J. C. Bose National fellowship. He also likes to thank ISRO for giving him "ISRO Merit Award 2017" and honoring him with the Visiting Scientist Position at PRL. K. K. Mahajan is thankful to the Indian National Science Academy for awarding lifetime Emeritus Scientist position. J. C. Gérard acknowledges partial support from the PRODEX Program managed by the European Space Agency with help of the Belgian Federal Science Policy Office (BELSPO). The contributions by N. M. Schneider, J. Deighan and S. K. Jain and S. W. Bougher were supported by NASA through the MAVEN Project.

## References

M.H. Acuña et al., Magnetic field and plasma observations at Mars: initial results of the Mars Global Surveyor mission. Science **279**, 1676–1680 (1998). https://doi.org/10.1126/science.279.5357.1676

D.E. Anderson, C.W. Hord, Mariner 6 and 7 ultraviolet spectrometer experiment: analysis of hydrogen Lyman-alpha data. J. Geophys. Res. **76**, 6666–6673 (1971). https://doi.org/10.1029/JA076i028p06666

D.J. Andrews et al., Oblique reflections in the Mars Express MARSIS data set: stable density structures in the Martian ionosphere. J. Geophys. Res. **119**, 3944–3960 (2014). https://doi.org/10.1002/2013JA019697

D.J. Andrews et al., Plasma observations during Mars atmospheric "Plume" event of March-April 2012. J. Geophys. Res. **121**, 3139–3154 (2016). https://doi.org/10.1002/2015JA022023

A.V. Artemyev et al., Mars magnetotail: nature's current sheet laboratory. J. Geophys. Res. **122**, 5404–5417 (2017). https://doi.org/10.1002/2017JA024048

A.S. Arya et al., Mars Colour Camera: the characterization/calibration and data analysis from Earth imaging phase. Curr. Sci. **109**, 1076–1086 (2015). https://doi.org/10.18520/v109/i6/1076-1086

S. Barabash et al., The Analyzer of Space Plasmas and Energetic Atoms (ASPERA-3) for the Mars Express mission. Space Sci. Rev. **126**, 113–164 (2006). https://doi.org/10.1007/s11214-006-9124-8

E.S. Barker, Detection of molecular oxygen in the Martian atmosphere. Nature **238**, 447–448 (1972). https://doi.org/10.1038/238447a0

M.J.S. Belton, D.M. Hunten, Water vapor in the atmosphere of Mars. Astrophys. J. **146**, 307–308 (1996)

J.L. Bertaux, F. Leblanc, O. Witasse, E. Quemerais, J. Lilensten, S.A. Stern, B. Sandel, O. Korablev, Discovery of an aurora on Mars. Nature **435**, 790–794 (2005). https://doi.org/10.1038/nature03603

A. Bhardwaj, S.K. Jain, Monte Carlo model of electron energy degradation in a $CO_2$ atmosphere. J. Geophys. Res. **114**, 1–14 (2009). https://doi.org/10.1029/2009JA014298

A. Bhardwaj, M. Michael, On the excitation of Io's atmosphere by the photoelectrons: application of the analytical yield spectrum of $SO_2$. Geophys. Res. Lett. **26**, 393–396 (1999)

A. Bhardwaj, S.A. Haider, R.P. Singhal, Auroral and photoelectron fluxes in cometary ionospheres. Icarus **85**, 216–228 (1990)

A. Bhardwaj, S.A. Haider, R.P. Singhal, Consequences of cometary aurora on the carbon chemistry at comet P/Halley. Adv. Space Res. **16**(2), 31–36 (1995)

A. Bhardwaj, S.A. Haider, R.P. Singhal, Production and emissions of atomic carbon and oxygen in the inner coma of comet Halley: role of electron impact. Icarus **120**, 412–430 (1996)

D.V. Bisikalo, V.I. Shematovich, J.C. Gérard, B. Hubert, Influence of crustal magnetic field on the Mars aurora electron flux and UV brightness. Icarus **282**, 127–135 (2017)

D.V. Bisikalo, V.I. Shematovich, J.C. Gérard, B. Hubert, Monte Carlo simulations of the interaction of fast proton and hydrogen atoms with the Martian atmosphere and comparison with in situ measurements. J. Geophys. Res. Space Phys. **123**(7), 5850–5861 (2018)

P.L. Bornmann, D. Speich, J. Hirman, V.J. Pizzo, R. Grubb, C. Balch, G. Heckman, The GOES solar X-ray imager: overview and operational goals. Proc. SPIE **2812**, 309–319 (1996). https://doi.org/10.1117/12.254078

S.W. Bougher, S. Engel, D.P. Hinson, J.M. Forbes, Mars Global Surveyor radio science electron density: neutral atmosphere implications. Geophys. Res. Lett. **28**, 3091–3094 (2001). https://doi.org/10.1029/2001GL012884

S.W. Bougher, D. Pawlowski, J.M. Bell, S. Nelli, T. McDunn, J.R. Murphy, M. Chizek, A. Ridley, Mars Global Thermosphere-Ionosphere model: solar cycle, seasonal and diurnal variations of the Mars upper atmosphere. J. Geophys. Res. **120**, 311–342 (2015a). https://doi.org/10.1002/2014/JE004715

S.W. Bougher et al., Early MAVEN deep dip campaign reveals thermosphere and ionosphere variability. Science **350**, 459 (2015b). https://doi.org/10.1126/science.aad0459

S.W. Bougher, D. Brain, J. Fox, G. Francisco, C. Simon-Wedlund, P. Withers, Upper neutral atmosphere and ionosphere, in *The Atmosphere and Climate of Mars*, ed. by R. Haberle, R. Clancy, F. Forget, M. Smith, R. Zurek (Cambridge University Press, Cambridge, 2017), pp. 433–463. https://doi.org/10.1017/9781139060172.014

D.A. Brain, J.S. Halekas, Aurora in the Martian mini-magnetospheres, in *Auroral Phenomenology and Magnetospheric Processes: Earth and Other Planets*. Geophysical Monograph Series, vol. 197 (2012), pp. 123–132. https://doi.org/10.1029/2011GM001201

D.A. Brain, F. Bagenal, M.H. Acuña, J.E.P. Connerney, Martian magnetic morphology: contributions from the solar wind and crust. J. Geophys. Res. **108**, A12 (2003). https://doi.org/10.1029/2002JA009482

D.A. Brain, J.S. Halekas, L.M. Peticolas, R.P. Lin, J.G. Luhmann, D.L. Mitchell, G.T. Delory, S.W. Bougher, M.H. Acuña, H. Rème, On the origin of aurorae on Mars. Geophys. Res. Lett. **33**, L01201 (2006). https://doi.org/10.1029/2005GL024782

D.A. Brain, R.J. Lillis, D.L. Mitchell, J.S. Halekas, R.P. Lin, Electron pitch angle distributions as indicators of magnetic field topology near Mars. J. Geophys. Res. **112**, A09201 (2007). https://doi.org/10.1029/2007JA012435

D.A. Brain et al., A comparison of global models for the solar wind interaction with Mars. Icarus **206**, 139–151 (2010). https://doi.org/10.1016/j.icarus.2009.06.030

D.A. Brain et al., The spatial distribution of planetary ion fluxes near Mars observed by MAVEN. Geophys. Res. Lett. **42**, 9142–9148 (2015). https://doi.org/10.1002/2015GL065293

L.F. Burlaga, F.B. McDonald, N.F. Ness, A.J. Lazarus, Cosmic ray modulation: Voyager 2 observations, 1987-1988. J. Geophys. Res. **96**, 3789–3799 (1991)

N.P. Carleton, W.A. Traub, Detection of molecular oxygen on Mars. Science **177**, 988–992 (1972). https://doi.org/10.1126/science.177.4053.988

M. Cartacci, E. Amata, A. Cichetti, R. Noschese, S. Giuppi, B. Langlasis et al., Mars ionosphere total electron content analysis from MARSIS subsurface data. Icarus **223**(1), 423–437 (2013)

M.S. Chaffin et al., Martian water loss to space enhanced by regional dust storms. Nat. Astron. **5**, 1036–1042 (2021)

P.C. Chamberlin et al., Solar ultraviolet irradiance observations of the solar flares during the intense September 2017 storm period. Space Weather **16**, 1470–1487 (2018). https://doi.org/10.1029/2018SW00186

J.Y. Chaufray, R. Modolo, F. Leblanc, G. Chanteur, R.E. Johnson, J.G. Luhmann, Mars solar wind interaction: formation of the Martian corona and atmospheric loss to space. J. Geophys. Res. **112**, E09009 (2007). https://doi.org/10.1029/2007JE002915

J.-Y. Chaufray, F. Gonzalez-Galindo, F. Forget, M. Lopez-Valverde, F. Leblanc, R. Modolo, S. Hess, M. Yagi, P.-L. Blelly, O. Witasse, Three-dimensional Martian ionosphere model: II. Effect of transport processes due to pressure gradients. J. Geophys. Res. **119**, 1614–1636 (2014). https://doi.org/10.1002/2013JE004551

T.E. Cravens, A.F. Nagy, Aeronomy of inner planets. Rev. Geophys. **21**, 263–273 (1983). https://doi.org/10.1029/RG021i002p00263

T.E. Cravens, A. Rahmati, J.L. Fox, R. Lillis, S. Bougher, J. Luhmann, S. Sakai, J. Deighan, Y. Lee, M. Combi, B. Jakosky, Hot oxygen escape from Mars: simple scaling with solar EUV irradiance. J. Geophys. Res. **122**, 1102–1116 (2017). https://doi.org/10.1002/2016JA023461

D.H. Crider, J. Espley, D.A. Brain, D.L. Mitchell, J.E.P. Connerney, M.H. Acuña, Mars Global Surveyor observations of the Halloween 2003 solar superstorm's encounter with Mars. J. Geophys. Res. **110**, A09S21 (2005). https://doi.org/10.1029/2004JA010881

J. Cui, M. Galand, R.V. Yelle, Y. Wei, S.-J. Zhang, Day-to-night transport in the Martian ionosphere: implications from total electron content measurements. J. Geophys. Res. **120**, 2333–2346 (2015). https://doi.org/10.1002/2014JA020788

A. Dalgarno, M.B. McElroy, R.J. Moffett, Electron temperatures in the ionosphere. Planet. Space Sci. **11**, 463–484 (1963)

J. Deighan et al., Discovery of a proton aurora at Mars. Nat. Astron. **2**, 802–807 (2018)

G.A. DiBraccio et al., The twisted configuration of the Martian magnetotail: MAVEN observations. Geophys. Res. Lett. **45**, 4559–4568 (2018). https://doi.org/10.1029/2018GL077251

C. Diéval, E. Kallio, S. Barabash, G. Stenberg, H. Nilsson, Y. Futaana, M. Holmström, A. Fedorov, R.A. Frahm, R. Jarvinen, D.A. Brain, A case study of proton precipitation at Mars: Mars Express observations and hybrid simulations. J. Geophys. Res. **117**, A06222 (2012). https://doi.org/10.1029/2012JA017537

C. Diéval, A.J. Kopf, J.A. Wild, Shapes of magnetically controlled electron density structures in the dayside Martian ionosphere. J. Geophys. Res. **123**, 3919–3942 (2018). https://doi.org/10.1002/2017JA025140
C. Dong, Y. Ma, S.W. Bougher, G. Toth, A.F. Nagy et al., Multi-fluid MHD study of the solar wind interaction with Mars upper atmosphere during the 2015 March 8th ICME event. Geophys. Res. Lett. **42**, 9103–9112 (2015). https://doi.org/10.1002/2015GL065944
E. Dubinin, G. Chanteur, M. Fraenz, J. Woch, Field aligned currents and parallel electric field potential drops at Mars. Scaling from the Earth' s aurora. Planet. Space Sci. **56**, 868–872 (2008). https://doi.org/10.1016/J.pss.2007.01.019
E. Dubinin et al., The effect of solar wind variations on the escape of oxygen ions from Mars through different channels: MAVEN observations. J. Geophys. Res. **122**, 11,285–11,301 (2017). https://doi.org/10.1002/2017JA024741
F. Duru et al., Magnetically controlled structures in the ionosphere of Mars. J. Geophys. Res. **111**, A12204 (2006). https://doi.org/10.1029/2006JA011975
J.P. Eastwood, D.A. Brain, J.S. Halekas, J.F. Drake, T.D. Phan, M. Øieroset, D.L. Mitchell, R.P. Lin, M. Acuña, Evidence for collisionless magnetic reconnection at Mars. Geophys. Res. Lett. **35**, L02106 (2008). https://doi.org/10.1029/2007GL032289
M.K. Elrod et al., He bulge revealed: He and $CO_2$ diurnal and seasonal variations in the upper atmosphere of Mars as detected by MAVEN NGIMS. J. Geophys. Res. **122**, 2564–2573 (2017). https://doi.org/10.1002/2016JA023482
M.K. Elrod, S.M. Curry, E.M.B. Thiemann, S.K. Jain, September 2017 solar flare event: rapid heating of the Martian neutral exosphere from the X-class flare as observed by MAVEN. Geophys. Res. Lett. **45**, 8803–8810 (2018). https://doi.org/10.1029/2018GL077729
M.K. Elrod, S.W. Bougher, K. Roeten, R. Sharrar, J. Murphy, Structural and compositional changes in the upper atmosphere revealed to the PEDE-2018 dust event on Mars as observed by MAVEN/NGIMS. Geophys. Res. Lett. **47**, e2019GL084378 (2020)
K. Fallows, P. Withers, G. Gonzalez, Response of the Mars ionosphere to solar flares: analysis of MGS radio occultation data. J. Geophys. Res. **120**, 9805–9825 (2015). https://doi.org/10.1002/2015JA021108
X. Fang, D. Pawlowski, Y. Ma, S.W. Bougher et al., Mars upper atmospheric responses to the 10 September 2017 solar flare: a global time-dependent simulation. Geophys. Res. Lett. **46**, 9334–9343 (2019). https://doi.org/10.1029/2019GL084515
A. Fedorova, J.-L. Bertaux, D. Betsis, F. Montmessin, O. Korablev, L. Maltagliati, J. Clarke, Water vapor in the middle atmosphere of Mars during the 2007 global dust storm. Icarus **300**, 440–457 (2018). https://doi.org/10.1016/j.icarus.2017.09.025
M.O. Fillingim et al., On wind driven electrojets at magnetic cusps in the nightside ionosphere of Mars. Earth Planets Space **64**, 93–103 (2012). https://doi.org/10.5047/eps.2011.04.010
S. Fonti, G.A. Marzo, Mapping the methane on Mars. Astron. Astrophys. **512**, A51 (2010). https://doi.org/10.1051/0004-6361/200913178
V. Formisano, S. Atreya, T. Encrenaz, N. Ignatiev, M. Giuranna, Detection of methane in the atmosphere of Mars. Science **306**, 1758–1761 (2004). https://doi.org/10.1126/science.1101732
C.M. Fowler et al., The first in situ electron temperature and density measurements of the Martian nightside ionosphere. Geophys. Res. Lett. **42**, 8854–8861 (2015). https://doi.org/10.1002/2015GL065267
J.L. Fox, Chemistry of the nightside ionosphere of Venus. Planet. Space Sci. **40**, 1663–1681 (1992). https://doi.org/10.1016/0032-0633(92)90124-7
J.L. Fox, Response of the Martian thermosphere/ionosphere to enhanced fluxes of solar soft X-rays. J. Geophys. Res. **109**, A11310 (2004). https://doi.org/10.1029/2004JA010380
J.L. Fox, The chemistry of protonated species in the Martian ionosphere. Icarus **252**, 366–392 (2015). https://doi.org/10.1016/j.icarus.2015.01.010
J.L. Fox, K.E. Yeager, MGS electron density profiles: analysis of the peak magnitudes. Icarus **200**, 468–479 (2009). https://doi.org/10.1016/j.icarus.2008.12.002
J.L. Fox, J.F. Brannon, H.S. Porter, Upper limits to the nightside ionosphere of Mars. Geophys. Res. Lett. **20**, 1391 (1993)
M. Fränz, E. Dubinin, E. Nielsen, J. Woch, S. Barabash, R. Lundin, A. Fedorov, Transterminator ion flow in the Martian ionosphere. Planet. Space Sci. **58**, 1442–1454 (2010). https://doi.org/10.1016/j.pss.2010.06.009
C.D. Fry, M. Dryer, W. Sun, Z. Smith, C.S. Deehr, S.I. Akasofu, Forecasting solar wind structures and shock arrival times using an ensemble of models. J. Geophys. Res. **108**, 1070 (2003). https://doi.org/10.1029/2002JA009474
Y. Futaana et al., First ENA observations at Mars: ENA emissions from the Martian upper atmosphere. Icarus **182**, 424–430 (2006a). https://doi.org/10.1016/j.icarus.2005.09.019
Y. Futaana et al., First ENA observations at Mars: subsolar ENA jet. Icarus **182**, 413–423 (2006b). https://doi.org/10.1016/j.icarus.2005.08.024

Y. Futaana et al., Global response of Martian plasma environment to an interplanetary structure: from ENA and plasma observations at Mars. Space Sci. Rev. **126**, 315–332 (2006c). https://doi.org/10.1007/s11214-006-9026-9
A. Galli et al., Direct measurements of energetic neutral hydrogen in the interplanetary medium. Astrophys. J. **644**, 1317 (2006a). https://doi.org/10.1086/503765
A. Galli et al., The hydrogen exospheric density profile measured with ASPERA-3/NPD. Space Sci. Rev. **126**, 447–467 (2006b). https://doi.org/10.1007/s11214-006-9089-7
A. Galli et al., Tailward flow of energetic neutral atoms observed at Mars. J. Geophys. Res. **113**, E1202 (2008). https://doi.org/10.1029/2008JE003139
J.C. Gérard, L. Soret, L. Libert, R. Lundin, A. Stiepen, A. Radioti, J.L. Bertaux, Concurrent observations of ultraviolet aurora and energetic electron precipitation with Mars Express. J. Geophys. Res. **120**, 6749–6765 (2015)
J.C. Gérard, L. Soret, V.I. Shematovich, D.V. Bisikalso, S.W. Bougher, The Mars diffuse aurora: a model of ultraviolet and visible emissions. Icarus **288**, 284–294 (2017)
J.C. Gérard, B. Hubert, B. Ritter, V.I. Shematovich, D.V. Bisikalo, Lyman $\alpha$ emission in the Martian proton aurora: line profile and role of horizontal induced magnetic field. Icarus **321**, 266–271 (2019)
F. González-Galindo, J.-Y. Chaufray, M.A. López-Valverde, G. Gilli, F. Forget, F. Leblanc, R. Modolo, S. Hess, M. Yagi, Three-dimensional Martian ionosphere model: I. The photochemical ionosphere below 180 km. J. Geophys. Res. **118**, 2105–2123 (2013). https://doi.org/10.1002/jgre.20150
N. Gopalaswamy, S. Yashiro, Y. Liu, G. Michalek, A. Vourlidas, M.L. Kaiser, R.A. Howard, Coronal mass ejections and other extreme characteristics of the 2003 October-November solar eruptions. J. Geophys. Res. **110**, A09S15 (2005). https://doi.org/10.1029/2004JA010958
A. Grigoriev, Y. Futaana, S. Barabash, A. Fedorov, Observations of the Martian subsolar ENA jet oscillations, in *The Mars Plasma Environment*, vol. 299 (2007). https://doi.org/10.1007/978-0-387-70943-7_11
H. Gröller, R. Yelle, T. Koskinen, F. Montmessin, G. Lacombe, N. Schneider, J. Deighan et al., Probing the Martian atmosphere with MAVEN/IUVS stellar occultations. Geophys. Res. Lett. **42**(21), 9064–9070 (2015). https://doi.org/10.1002/2015GL065294
H. Gröller, F. Montmessin, R. Yelle, F. Lefèvre, F. Forget, N. Schneider, T. Koskinen, J. Deighan, S. Jain, MAVEN/IUVS stellar occultation measurements of Mars atmospheric structure and composition. J. Geophys. Res., Planets **123**(6), 1449–1483 (2018). https://doi.org/10.1029/2017JE005466
H. Gunell et al., First ENA observations at Mars: charge exchange ENAs produced in the magnetosheath. Icarus **182**, 431–438 (2006). https://doi.org/10.1016/j.icarus.2005.10.027
D.A. Gurnett et al., Radar soundings of the ionosphere of Mars. Science **310**, 1929–1933 (2005). https://doi.org/10.1126/science.1121868
R.M. Haberle, J. Manoj, J. Murphy, J. Barnes, J. Schofield, G. Wilson, M. Valverde, General circulation model simulations of the Mars Pathfinder atmospheric structure investigation/meteorology data. J. Geophys. Res., Planets **104**(E4), 8957–8974 (1999)
R.M. Haberle, K. Zahnle, N.G. Barlow, K.E. Steakley, Impact degassing of $H_2$ on early Mars and its effect on the climate system. Geophys. Res. Lett. **46**(22), 13355–13362 (2019)
S.A. Haider, Chemistry on the nightside ionosphere of Mars. J. Geophys. Res. **102**, 407–416 (1997). https://doi.org/10.1029/96JA02353
S.A. Haider, A. Bhardwaj, Radial distribution of production rates, loss rates and densities corresponding to ion masses $\leq 40$ amu in the inner coma of comet Halley: composition and chemistry. Icarus **177**, 196–216 (2005)
S.A. Haider, K.K. Mahajan, Lower and upper ionosphere of Mars. Space Sci. Rev. **182**, 19–84 (2014). https://doi.org/10.1007/s11214-014-0058-2
S.A. Haider, J. Masoom, Modeling of diffuse aurora due to precipitation of $H^+$-H and SEP electrons in the nighttime atmosphere of Mars: Monte Carlo simulation and MAVEN observation. J. Geophys. Res. **124**, 9566–9576 (2019). https://doi.org/10.1029/2019JA026688
S.A. Haider, R.P. Singhal, Analytical yield spectrum approach to electron energy degradation in Earth's atmosphere. J. Geophys. Res. **88**, 7185–7189 (1983). https://doi.org/10.1029/JA088iA09p07185
S.A. Haider, R.P. Singhal, Analytical approach to backscattering of low energy electrons. J. Geophys. Res. Space Phys. **91**, 13761–13763 (1986)
S.A. Haider, J. Kim, A.F. Nagy, C.N. Keller, M.I. Verigin, K.I. Gringauz, N.M. Shutte, K. Szego, P. Kiraly, Calculated ionization rates, ion densities and airglow emission rates due to precipitating electrons in the nightside ionosphere of Mars. J. Geophys. Res. **97**, 10637–10641 (1992)
S.A. Haider, S.P. Seth, E. Kallio, K.I. Oyama, Solar EUV and electron-proton-hydrogen atom-produced ionosphere on Mars: comparative studies of particle fluxes and ion production rates due to different processes. Icarus **159**, 18–30 (2002). https://doi.org/10.1006/icarus.2002.6919
S.A. Haider, S.P. Seth, V.R. Choksi, K.I. Oyama, Model of photoelectron impact ionization within the high latitude ionosphere at Mars: comparison of calculated and measured electron density. Icarus **185**, 102–112 (2006). https://doi.org/10.1016/j.icarus.2006.07.010

S.A. Haider, M.A. Abdu, I.S. Batista, J.H. Sobral, X. Luan, E. Kallio, W.C. Maguire, M.I. Verigin, V. Singh, D, E, and F layers in the daytime at high-latitude terminator ionosphere of Mars: comparison with Earth's ionosphere using COSMIC data. J. Geophys. Res. **114**, A03311 (2009). https://doi.org/10.1029/2008JA013709

S.A. Haider, S.P. Seth, D.A. Brain, D.L. Mitchell, T. Majeed, S.W. Bougher, Modeling photoelectron transport in the Martian ionosphere at Olympus Mons and Syrtis Major: MGS observations. J. Geophys. Res. **115**, A08310 (2010). https://doi.org/10.1029/2009JA014968

S.A. Haider, K.K. Mahajan, E. Kallio, Mars ionosphere: a review of experimental results and modeling studies. Rev. Geophys. **49**, RG4001 (2011). https://doi.org/10.1029/2011RG000357

S.A. Haider, S.M.P. McKenna-Lawlor, C.D. Fry, R. Jain, K.N. Joshipura, Effects of solar X-ray flares in the E region ionosphere of Mars: first model results. J. Geophys. Res. **117**, A05326 (2012). https://doi.org/10.1029/2011JA017436

S.A. Haider, B.M. Pandya, G.J. Molina-Cuberos, Nighttime ionosphere caused by meteoroid ablation and solar wind electron-proton-hydrogen impact: MEX observation and modelling. J. Geophys. Res. **115**, 1–9 (2013). https://doi.org/10.1002/jgra.50590

T.S. Halekas et al., MAVEN observations of solar wind hydrogen deposition in the atmosphere of Mars. Geophys. Res. Lett. **42**, 8901–8909 (2015). https://doi.org/10.1002/2015GL064693

W.B. Hanson, S. Sanatani, D.R. Zuccarao, The Martian ionosphere as observed by Viking retarding potential analyzer. J. Geophys. Res. **82**, 4351–4363 (1977). https://doi.org/10.1029/JS082i028p04351

Y. Harada, D.A. Gurnett, A.J. Kopf, J.S. Halekas, S. Ruhunusiri, G.A. DiBraccio, J. Espley, D.A. Brain, MARSIS observations of the Martian nightside ionosphere during the September 2017 solar event. Geophys. Res. Lett. **45**, 7960–7967 (2018). https://doi.org/10.1002/2018GL077622

D.P. Hinson, R.A. Simpson, J.D. Twicken, G.L. Tyler, F.M. Flasar, Initial results from radio occultation measurements with Mars Global Surveyor. J. Geophys. Res. **104**, 26,997–27,012 (1999). https://doi.org/10.1029/1999JE001069

A. Hughes, M. Chaffin, E. Mierkiewicz, J. Deighan, S. Jain, N. Schneider, M. Mayyasi, B. Jakosky, Proton aurora on Mars: a dayside phenomenon pervasive in southern summer. J. Geophys. Res. Space Phys. **124**, 10533–10548 (2019). https://doi.org/10.1029/2019JA027140

W.H. Ip, On a hot oxygen corona of Mars. Icarus **76**, 135–145 (1998). https://doi.org/10.1016/0019-1035(88)90146-7

W.H. Ip, ENA diagnostic of auroral activity at Mars. Planet. Space Sci. **63/64**, 83–86 (2012)

B.M. Jakosky et al., The Mars Atmosphere and Volatile EvolutioN (MAVEN) mission. Space Sci. Rev. **195**, 3–48 (2015)

B.M. Jakosky et al., Loss of the Martian atmosphere to space: present-day loss rates determined from MAVEN observations and integrated loss through time. Icarus **315**, 146–157 (2018). https://doi.org/10.1016/j.icarus.2018.05.030

M.A. Kahre, J.R. Murphy, C.E. Newman, R.J. Wilson, B.A. Cantor, M.T. Lemmon, M.J. Wolff, The Mars dust cycle, in *The Atmosphere and Climate of Mars*, vol. 18 (2017), p. 295

E. Kallio, S. Barabash, Atmospheric effects of precipitating energetic hydrogen atoms on the Martian atmosphere. J. Geophys. Res. **106**, 165–177 (2001)

E. Kallio, P. Janhunen, Atmospheric effects of proton precipitation in the Martian atmosphere and its connection to the Mars-solar wind interaction. J. Geophys. Res. **106**, 5617–5634 (2001)

E. Kallio, J.G. Luhma, S. Barabash, Charge exchange near Mars: the solar wind absorption and energetic neutral atom production. J. Geophys. Res. **102**, 22183–22197 (1997)

E. Kallio, K. Liu, R. Javinen, V. Pohjola, P. Janhunen, Oxygen ion escape at Mars in a hybrid model: high energy and low energy ions. Icarus **206**, 152–163 (2010). https://doi.org/10.1016/j.icarus.2009.05.015

L.D. Kaplan, G. Münch, H. Spinrad, An analysis of the spectrum of Mars. Astrophys. J. **139**, 1 (1964). https://doi.org/10.1086/147736

L.D. Kaplan, J. Connes, P. Connes, Carbon monoxide in the Martian atmosphere. Astrophys. J. **157**, L187 (1969)

J. Kar, Recent advances in planetary ionospheres. Space Sci. Rev. **77**, 193–266 (1996). https://doi.org/10.1007/BF00226224

G.M. Keating, S.W. Bougher, R.W. Zurek, R.H. Tolson, G.J. Cancro, S.N. Noll et al., The structure of the upper atmosphere of Mars: in situ accelerometer measurements from Mars Global Surveyor. Science **279**(5357), 1672–1676 (1998)

A.J. Kliore, D.L. Cain, G.S. Levy, V.R. Eshleman, G. Fjeldbo, F.O. Drake, Occultation experiment: results of the first direct measurement of Mars atmosphere and ionosphere. Science **149**, 1243–1248 (1965). https://doi.org/10.1126/science.149.3689

O. Korablev et al., The Atmospheric Chemistry Suite (ACS) of three spectrometers for the ExoMars 2016 trace gas orbiter. Space Sci. Rev. **214**, 1–62 (2018). https://doi.org/10.1007/s11214-017-0437-6

V.A. Krasnopolsky, *Photochemistry of the Atmospheres of Mars and Venus*. Physics and Chemistry in Space, vol. 13 (1986). https://doi.org/10.1007/978-3-642-70401-7

V.A. Krasnopolsky, Spectroscopic mapping of Mars CO mixing ratio: detection of north-south asymmetry. J. Geophys. Res. **108**(E2), 5010 (2003). https://doi.org/10.1029/2002JE001926

A.M. Krymskii, T.K. Breus, N.F. Ness, M.H. Acuña, J.E.P. Connerney, D.H. Crider, D.L. Mitchell, S.J. Bauer, Structure of the magnetic field fluxes connected with crustal magnetization and topside ionosphere at Mars. J. Geophys. Res. **107**, 1245 (2002). https://doi.org/10.1029/2001JA000239

G.P. Kuiper, *The Atmospheres of the Earth and Planets* (University of Chicago Press, Chicago, 1952)

F. Leblanc, O. Witasse, J. Winningham, D. Brain, J. Lilensten, P.-L. Blelly, R.A. Frahm, J.S. Halekas, J.L. Bertaux, Origins of the Martian aurora observed by Spectroscopy for Investigation of Characteristics of the Atmosphere of Mars (SPICAM) on board Mars Express. J. Geophys. Res. **111**, A09313 (2006). https://doi.org/10.1029/2006JA011763

F. Leblanc et al., Observations of aurora by SPICAM ultraviolet spectrograph on board Mars Express: simultaneous ASPERA-3 and MARSIS measurements. J. Geophys. Res. **113**, A08311 (2008)

S. Lebonnois, E. Quémerais, F. Montmessin, F. Lefèvre, S. Perrier, J.-L. Bertaux, F. Forget, Vertical distribution of ozone on Mars as measured by SPICAM/Mars Express using stellar occultations. J. Geophys. Res. **111**, E09S05 (2006). https://doi.org/10.1029/2005JE002643

S.A. Ledvina, Y.J. Ma, E. Kallio, Modeling and simulating flowing plasmas and related phenomena. Space Sci. Rev. **139**(1–4), 143–189 (2008)

C.O. Lee et al., MAVEN observations of the solar cycle 24 space weather conditions at Mars. J. Geophys. Res. **122**, 2768–2794 (2017). https://doi.org/10.1002/2016JA023495

C.O. Lee, B.M. Jakosky, J.G. Luhmann, D.A. Brain, M.L. Mays, D.M. Hassler, M. Holmström, D.E. Larson, D.L. Mitchell, C. Mazelle, J.S. Halekas, Observations and impacts of the 10 September 2017 solar events at Mars: an overview and synthesis of the initial results. Geophys. Res. Lett. **45**, 8871–8885 (2018). https://doi.org/10.1029/2018GL079162

M.T. Lemmon, M.J. Wolff, J.F. Bell III, M.D. Smith, B.A. Cantor, P.H. Smith, Dust aerosol, clouds, and the atmospheric optical depth record over 5 Mars years of the Mars Exploration Rover mission. Icarus **251**, 96–111 (2015). https://doi.org/10.1016/j.icarus.2014.03.029

M.W. Liemohn et al., Numerical modeling of magnetic topology near Marsauroral observations. Geophys. Res. Lett. **34**, L24202 (2007). https://doi.org/10.1029/2007GL031806

J. Lilensten, D. Bernard, M. Barthélémy, G. Gronoff, C. Simon Wedlund, A. Opitz, Prediction of blue, red and green aurorae at Mars. Planet. Space Sci. **115**, 48–56 (2015)

R.J. Lillis, M.O. Fillingim, D.A. Brain, Three-dimensional structure of the Martian nightside ionosphere: predicted rates of impact ionization from Mars Global Surveyor magnetometer and electron reflectometer measurements of precipitating electrons. J. Geophys. Res. **116**, A12317 (2011). https://doi.org/10.1029/2011JA016982

R.J. Lillis, S. Robbins, M. Manga, J.S. Halekas, H.V. Frey, Time history of the Martian dynamo from crater magnetic field analysis. J. Geophys. Res. **118**, 1488–1511 (2013). https://doi.org/10.1002/jgre.20105

G. Liu, S.L. England, R.J. Lillis, P. Withers, P.R. Mahaffy, D.E. Rowland, M. Elrod et al., Thermospheric expansion associated with dust increase in the lower atmosphere on Mars observed by MAVEN/NGIMS. Geophys. Res. Lett. **45**, 2901–2910 (2018)

J.G. Luhmann et al., Martian magnetic storms. J. Geophys. Res. **122**, 6185–6209 (2017). https://doi.org/10.1002/2016JA023513

J.G. Luhmann, M.L. Mays, Y. Li, C.O. Lee, H. Bain, D. Odstrcil, R.A. Mewaldt, C.M.S. Cohen, D. Larson, G. Petrie, Shock connectivity and the late cycle 24 solar energetic particle events in July and September 2017. Space Weather **16**, 557–568 (2018). https://doi.org/10.1029/2018SW001860

A.T.Y. Lui, P. Perreault, S.I. Akasofu, C.D. Anger, The diffuse aurora. Planet. Space Sci. **21**(5), 857–861 (1973). https://doi.org/10.1016/0032-0633(73)90102-5

R. Lundin et al., Solar wind-induced atmospheric erosion at Mars: first results from ASPERA-3 on Mars Express. Science **305**, 1933–1936 (2004). https://doi.org/10.1126/science.1101860

R. Lundin et al., Auroral plasma acceleration above Martian magnetic anomalies. Space Sci. Rev. **126**, 333–354 (2006)

R. Lundin, S. Barabash, E. Dubinin, D. Winningham, M. Yamauchi, Low-altitude acceleration of ionospheric ions at Mars. Geophys. Res. Lett. **38**, L08108 (2011). https://doi.org/10.1029/2011GL047064

Y.J. Ma, A.F. Nagy, V.I. Sokolov, K.C. Hansen, Three-dimensional, multi-species, high spatial resolution MHD studies of the solar wind interaction with Mars. J. Geophys. Res. **109**, A07211 (2004). https://doi.org/10.1029/2003JA010367

Y.J. Ma et al., Variations of the Martian plasma environment during the ICME passage on 8 March 2015: a time-dependent MHD study. J. Geophys. Res. **122**, 1714–1730 (2017). https://doi.org/10.1002/2016JA023402

P.R. Mahaffy et al., The neutral gas and ion mass spectrometer on the Mars atmosphere and volatile evolution mission. Space Sci. Rev. **195**, 49–73 (2015). https://doi.org/10.1007/s11214-014-0091-1
K.K. Mahajan, J. Kar, Planetary ionospheres. Space Sci. Rev. **47**, 303–397 (1988). https://doi.org/10.1007/BF00243558
K.K. Mahajan, N.K. Lodhi, S. Singh, Ionospheric effects of solar flares at Mars. Geophys. Res. Lett. **36**, L15207 (2009). https://doi.org/10.1029/2009GL039454
G.T. Marklund, Electric fields and plasma processes in the auroral downward current region, below, within, and above the acceleration region. Space Sci. Rev. **142**, 1–21 (2009). https://doi.org/10.1007/s11214-008-9373-9
G.A. Marzo, T.L. Roush, A. Blanco, S. Fonti, V. Orofino, Statistical exploration and volume reduction of planetary remote sensing spectral data. J. Geophys. Res. **113**, E12009 (2008). https://doi.org/10.1029/2008JE003219
K. Matsunaga, K. Seki, T. Hara, D.A. Brain, Asymmetric penetration of shocked solar wind down to 400 km altitudes at Mars. J. Geophys. Res. **120**, 6874–6883 (2015). https://doi.org/10.1002/2014JA020757
B. Mauk, F. Bagenal, Comparative auroral physics: Earth and other planets, in *Auroral Phenomenology and Magnetospheric Processes: Earth and Other Planets*. Geophys. Monogr. Ser. (2012). https://doi.org/10.1029/2011GM001192
M.B. McElroy, T.Y. Kong, Y.L. Yung, A.O. Nier, Composition and structure of the Martian upper atmosphere: analysis of results from Viking. Science **194**, 1295–1298 (1976). https://doi.org/10.1126/science.194.4271.1295
M. Mendillo, P. Withers, D. Hinson, H. Rishbeth, B. Reinisch, Effects of solar flares on the ionosphere of Mars. Science **311**, 1135–1138 (2006). https://doi.org/10.1126/science.1122099
A. Milillo, A. Mura, S. Orsini, S. Massetti, P.C. son Brandt, T. Sotirelis, R. D'Amicis, S. Barabash, R.A. Frahm, E. Kallio, A. Galli, P. Wurz, M. Holmstrom, E.C. Roelof, J.D. Winningham, P. Cerulli-Irelli, S. Livi, R. Lundin, M. Maggi, A. Morbidini, Statistical analysis of the observations of the MEX/ASPERA-3 NPI in the shadow. Planet. Space Sci. **57**, 1000–1007 (2009). https://doi.org/10.1016/j.pss.2008.09.016
E. Millour et al., A new Mars climate database v5.1, paper 1301 presented at the Fifth International Workshop on Mars Atmosphere: Modeling and Observations. Oxford, UK, Jan. 2014 (2014)
D.L. Mitchell et al., Oxygen Auger electrons observed in Mars ionosphere. Geophys. Res. Lett. **27**(13), 1871–1874 (2000). https://doi.org/10.1029/1999GL010754
D.L. Mitchell et al., Probing Mars' crustal magnetic field and ionosphere with the MGS electron reflectometer. J. Geophys. Res. **106**, 23419–23428 (2001). https://doi.org/10.1029/2000JE001435
D.L. Mitchell, R.J. Lillis, R.P. Lin, J.E.P. Connerney, M.H. Acuña, A global map of Mars' crustal magnetic field based on electron reflectometry. J. Geophys. Res. **112**, E01002 (2007). https://doi.org/10.1029/2005JE002564
G.J. Molina-Cuberos, H. Lichtenegger, K. Schwingenschuh, J.J. Lopez-Moreno, R. Rodrigo, Ion-neutral chemistry model of the lower ionosphere of Mars. J. Geophys. Res. **107**(E5), 5027 (2002). https://doi.org/10.1029/2000JE001447
F. Montmessin, F. Lefèvre, Transport-driven formation of a polar ozone layer on Mars. Nat. Geosci. **6**, 930–933 (2013). https://doi.org/10.1038/ngeo1957
F. Montmessin, E. Quémerais, J.L. Bertaux, O. Korablev, P. Rannou, S. Lebonnois, Stellar occultations at UV wavelengths by the SPICAM instrument: retrieval and analysis of Martian haze profiles. J. Geophys. Res. **111**, E09S09 (2006). https://doi.org/10.1029/2005JE002662
D.D. Morgan et al., Effects of a strong ICME on the Martian ionosphere as detected by Mars Express and Mars Odyssey. J. Geophys. Res. **119**, 5891–5908 (2014). https://doi.org/10.1002/2013JA019522
J. Mouginot, W. Kofman, A. Safaeinili, A. Herique, Correction of the ionospheric distortion on the MARSIS surface sounding echoes. Planet. Space Sci. **56**, 917–926 (2008)
M.J. Mumma, G.L. Villanueva, R.E. Novak, T. Hewagama, B.P. Bonev, M.A. DiSanti, A.M. Mandell, M.D. Smith, Strong release of methane on Mars in northern summer 2003. Science **323**, 1041–1045 (2009). https://doi.org/10.1126/science.1165243
A.F. Nagy et al., The plasma environment of Mars. Space Sci. Rev. **111**, 33–114 (2004). https://doi.org/10.1023/B:SPAC.0000032718.47512.92
F. Němec, D.D. Morgan, D.A. Gurnett, D.A. Brain, Areas of enhanced ionization in the deep nightside ionosphere of Mars. J. Geophys. Res. **116**, E06006 (2011). https://doi.org/10.1029/2011JE003804
E. Nielsen et al., Local plasma processes and enhanced electron densities in the lower ionosphere in magnetic cusp regions on Mars. Planet. Space Sci. **55**(14), 2164–2172 (2007). https://doi.org/10.1016/j.pss.2007.07.003
A.O. Nier, M.B. McElroy, Composition and structure of Mars upper atmosphere: results from the neutral mass spectrometer on Viking 1 and 2. J. Geophys. Res. **82**, 4341–4349 (1977). https://doi.org/10.1029/JS082i028p04341

B.M. Pandya, S.A. Haider, Numerical simulation of the effects of meteoroid ablation and solar EUV/X-ray radiation in the dayside ionosphere of Mars: MGS/MEX observations. J. Geophys. Res. **119**, 9228–9245 (2014). https://doi.org/10.1002/2014JA020063

T.D. Parkinson, D.M. Hunten, Spectroscopy and aeronomy of $O_2$ on Mars. J. Atmos. Sci. **29**, 1380 (1972)

K. Peter et al., The dayside ionospheres of Mars and Venus: comparing a one-dimensional photochemical model with MaRS (Mars Express) and VeRa (Venus Express) observations. Icarus **233**, 66–82 (2014). https://doi.org/10.1016/j.icarus.2014.01.028

G. Picardi et al., in *Mars Express: A European Mission to the Red Planet*, ed. by A. Wilson. ESA Rep., vol. SP-1240 (European Space Agency Publ., Division, Noordwijk, 2004), pp. 51–69

E. Quémerais, J.-L. Bertaux, O. Korablev, E. Dimarellis, C. Cot, B.R. Sandel, D. Fussen, Stellar occultations observed by SPICAM on Mars Express. J. Geophys. Res. **111**, E09S04 (2006). https://doi.org/10.1029/2005JE002604

R. Ramstad, M. Holmström, Y. Futaana, C.O. Lee, A. Rahmati, P. Dunn, R.J. Lillis, D. Larson, The September 2017 SEP event in context with the current solar cycle: Mars Express ASPERA-3/IMA and MAVEN/SEP observations. Geophys. Res. Lett. **45**, 7306–7311 (2018). https://doi.org/10.1029/2018GL077842

R. Ramstad, A. Brain, Y. Dong, J. Espley, J. Halekas, B. Jakosky, The global current systems of the Martian induced magnetosphere. Nat. Astron. **4**, 979–985 (2020). https://doi.org/10.1038/s41550-020-1099-y

L.H. Regoli et al., Statistical study of the energetic proton environment at Titan's orbit from the Cassini spacecraft. J. Geophys. Res. **123**, 4820–4834 (2018). https://doi.org/10.1029/2018JA025442

B. Ritter, J.-C. Gérard, B. Hubert, L. Rodrigues, F. Montmessin, Observations of the proton aurora on Mars with SPICAM onboard Mars Express. Geophys. Res. Lett. **45**, 612–619 (2018). https://doi.org/10.1002/2017GL076235

R. Rodrigo, E. Graciá-Álvarez, M.J. López-González, J.J. López-Moreno, A non-steady one-dimensional theoretical model of Mars' neutral atmospheric composition between 30 and 200 km. J. Geophys. Res. **95**, 14,795–14,810 (1990). https://doi.org/10.1029/JB095iB09p14795

A. Safaeinili, W. Kofman, J. Mouginot, Y. Gim, A. Herique et al., Estimation of the total electron content of the Martian ionosphere using radar sounder surface echoes. Geophys. Res. Lett. **34**, L23204 (2007)

S. Sakai, K. Seki, N. Terada, H. Shinagawa, R. Sakata, T. Tanaka, Y. Ebihara, Effects of the IMF direction on atmospheric escape from a Mars like planet under weak intrinsic magnetic field conditions. J. Geophys. Res. **126**, e28485 (2021). https://doi.org/10.1029/2020JA028485

B. Sánchez-Cano et al., Total electron content in the Martian atmosphere: a critical assessment of the Mars Express MARSIS data sets. J. Geophys. Res. **120**, 2166–2182 (2015). https://doi.org/10.1002/2014JA020630

B. Sánchez-Cano et al., Origin of the extended Mars radar blackout of September 2017. J. Geophys. Res. **124**, 4556–4568 (2019). https://doi.org/10.1029/2018JA026403

N.A. Savich, V.A. Samovol, The nighttime ionosphere of Mars from Mars 4 and Mars 5 dual frequency radio occultation measurements. Space Res. **16**, 1009–1010 (1976)

N.M. Schneider et al., Discovery of diffuse aurora on Mars. Science **350**, aad0313 (2015). https://doi.org/10.1126/science.aad0313

N.M. Schneider et al., Global aurora on Mars during the September 2017 space weather event. Geophys. Res. Lett. **45**, 7391–7398 (2018). https://doi.org/10.1029/2018GL077772

N.M. Schneider et al., Discrete aurora on Mars: insights into their distribution and activity from MAVEN/IUVS observations. J. Geophys. Res. Space Phys. **126**, e2021JA029428 (2021)

R.W. Schunk, A.F. Nagy, Ionospheres of the terrestrial planets. Rev. Geophys. **18**, 813–852 (1980). https://doi.org/10.1029/RG018i004p00813

R.W. Schunk, A.F. Nagy, *Ionospheres*, 2nd edn. (Cambridge University Press, New York, 2009)

A. Seiff, D.B. Kirk, Structure of the atmosphere of Mars in summer at mid-latitudes. J. Geophys. Res. **82**, 4364–4378 (1977). https://doi.org/10.1029/JS082i028p04364

S.P. Seth, S.A. Haider, K.I. Oyama, The photoelectron flux and nightglow emissions of 5577 and 6300 Å due to solar wind electron precipitation in Martian atmosphere. J. Geophys. Res. **107**(A10), 1324 (2002). https://doi.org/10.1029/2001JA000261

V.I. Shematovich, D.V. Bisikalo, J.-C. Gérard, A kinetic model of the formation of the hot oxygen geocorona: 1. Quiet geomagnetic conditions. J. Geophys. Res. **99**, 23,217–23,228 (1994). https://doi.org/10.1029/94JA01769

V.I. Shematovich, D.V. Bisikalo, J.-C. Gérard, C. Cox, S.W. Bougher, F. Leblanc, Monte Carlo model of electron transport for the calculation of Mars dayglow emissions. J. Geophys. Res. **113**, E02011 (2008). https://doi.org/10.1029/2007JE002938

V.I. Shematovich, D.V. Bisikalo, C. Diéval, S. Barabash, G. Stenberg, H. Nilsson, Y. Futaana, M. Holmstrom, J.-C. Gérard, Proton and hydrogen atom transport in the Martian upper atmosphere with an induced magnetic field. J. Geophys. Res. **116**, A11320 (2011). https://doi.org/10.1029/2011JA017007

V.I. Shematovich, D.V. Bisikalo, J.C. Gérard, B. Hubert, Kinetic Monte Carlo model for the precipitation of high-energy protons and hydrogen atoms into the atmosphere of Mars with taking into account the measured magnetic field. Astron. Rep. **63**(10), 835–845 (2019)

H. Shinagawa, T.E. Cravens, A one-dimensional multispecies magneto hydrodynamic model of the dayside ionosphere of Mars. J. Geophys. Res. **94**, 6506–6516 (1989). https://doi.org/10.1029/JA094iA06p06506

R.P. Singhal, A. Bhardwaj, Monte Carlo simulation of photoelectron energization in a parallel electric fields – electroglow on Uranus. J. Geophys. Res. **961**(A9), 156963–156972 (1991)

R.P. Singhal, S.A. Haider, Analytical yield spectrum approach to photoelectron fluxes in the Earth's atmosphere. J. Geophys. Res. **89**, 6847–6852 (1984). https://doi.org/10.1029/JA089iA08p06847

R.P. Singhal, C.H. Jackman, A.E.S. Green, Spatial aspects of low and medium energy electron degradation in $N_2$. J. Geophys. Res. **85**, 1246–1254 (1980). https://doi.org/10.1029/JA085iA03p01246

M. Smith, S. Bougher, T. Encrenaz, F. Forget, A. Kleinbohl, Thermal structure and composition, in *The Atmosphere and Climate of Mars*, ed. by R. Haberle, R. Clancy, F. Forget, M. Smith, R. Zurek (Cambridge University Press, Cambridge, 2017), pp. 42–75. https://doi.org/10.1017/9781139060172.004

Y. Soobiah et al., Observations of magnetic anomaly signatures in Mars Express ASPERA-3 ELS data. Icarus **182**(2), 396–405 (2006). https://doi.org/10.1016/j.icarus.2005.10.034

L. Soret, J.C. Gérard, L. Libert, V.I. Shematovich, D.V. Bisikalo, A. Stiepen, J.L. Bertaux, SPICAM observations and modeling of Mars aurorae. Icarus **264**, 398–406 (2016)

L. Soret et al., Discrete aurora on Mars: spectral properties, vertical profiles and electron energies. J. Geophys. Res. Space Phys. **126**, e2021JA029495 (2021)

H. Spinrad, G. Münch, L.D. Kaplan, Letter to the editor: the detection of water vapor on Mars. Astrophys. J. **137**, 1319 (1963). https://doi.org/10.1086/147613

S.W. Stone, R.V. Yelle, M. Benna, M.K. Elrod, P.R. Mahaffy, Thermal structure of the Martian upper atmosphere from MAAVEN/NGIMS. J. Geophys. Res., Planets **123**(11), 2842–2867 (2018)

S.W. Stone, R.V. Yelle, M. Benna, M.K. Elrod, Hydrogen escape from Mars driven by seasonal and dust storm transport of water. Science **370**(6518), 824 (2020)

D.J. Strickland, G.E. Thomas, P.R. Sparks, Mariner 6 and 7 Ultraviolet Spectrometer Experiment: analysis of the OI 1304 Å and 1356 Å emissions. J. Geophys. Res. **77**, 4052–4068 (1972). https://doi.org/10.1029/JA077i022p04052

P. Thirupathaiah, S.Y. Shah, S.A. Haider, Characteristics of solar X-ray flares and their effects on the ionosphere and human exploration to Mars: MGS radio science observations. Icarus **330**, 60–74 (2019). https://doi.org/10.1016/j.icarus.2019.04.015

D. Ulusen, D.A. Brain, D.L. Mitchell, Observation of conical electron distributions over Martian crustal magnetic fields. J. Geophys. Res. Space Phys. **116**, A07214 (2011). https://doi.org/10.1029/2010JA016217

A. Valeille, M.R. Combi, S.W. Bougher, V. Tenishev, A.F. Nagy, Three-dimensional study of Mars upper thermosphere/ionosphere and hot oxygen corona: 2. Solar cycle, seasonal variations, and evolution over history. J. Geophys. Res. **114**, E11006 (2009). https://doi.org/10.1029/2009JE003389

A.C. Vandaele et al., NOMAD, an integrated suite of three spectrometers for the ExoMars trace gas mission: technical description, science objectives and expected performance. Space Sci. Rev. **214**, 1–47 (2018). https://doi.org/10.1007/s11214-018-0517-2

A.C. Vandaele et al., Martian dust storm impact on atmospheric $H_2O$ and D/H observed by ExoMars Trace Gas Orbiter. Nature **568**, 521–525 (2019). https://doi.org/10.1038/s41586-019-1097-3

M.B. Vasiliev et al., Preliminary results of dual frequency radio occultation of the Martian ionosphere with the aid of Mars 5 spacecraft. Kosm. Issled. **13**, 48–51 (1975)

N. Venkateswara Rao, V. Leelavathi, P. Mohanamanasa, S.A. Haider, S.V.B. Rao, Enhanced ionization in magnetic anomaly regions of the Martian lower ionosphere associated with dust storms. J. Geophys. Res. **124**, 3007–3020 (2019). https://doi.org/10.1029/2018JA026283

S. Vennerstrom, Magnetic storms on Mars. Icarus **215**, 234–241 (2011). https://doi.org/10.1016/j.icarus.2011.06.030

M.I. Verigin, K.I. Gringauz, N.M. Shutte, S.A. Haider, K. Szego, P. Kiraly, A.F. Nagy, T.I. Gombosi, On the possible source of the ionization in the nighttime Martian ionosphere 1. Phobos 2 HARP electron spectrometer measurements. J. Geophys. Res. **96**, 19307–19313 (1991)

T. Weber, D. Brain, S. Xu, D. Mitchell, J. Espley, J. Halekas, C. Mazelle, R. Lillis, G. DiBraccio, B. Jakosky, The influence of interplanetary magnetic field direction on Martian crustal magnetic field topology. Geophys. Res. Lett. **47**, e87757 (2020). https://doi.org/10.1029/2020GL087757

C.R. Webster et al., Mars methane detection and variability at Gale crater. Science **347**, 415–417 (2015). https://doi.org/10.1126/science.1261713

R.C. Whitten, L. Colin, Ionosphere of Mars and Venus. Rev. Geophys. **12**, 155–192 (1974). https://doi.org/10.1029/RG012i002p00155

P. Withers, A review of observed variability in the dayside ionosphere of Mars. Adv. Space Res. **44**, 277–307 (2009)
P. Withers, R. Pratt, An observational study of the response of the upper atmosphere of Mars to lower atmospheric dust storms. Icarus **225**, 378–389 (2013). https://doi.org/10.1016/j.icarus.2013.02.032
P. Withers, M.O. Fillingim, R.J. Lillis, B. Häusler, D.P. Hinson, G.L. Tyler, M. Pätzold, K. Peter, S. Tellmann, O. Witasse, Observations of the nightside ionosphere of Mars by the Mars Express Radio Science Experiment (MaRS). J. Geophys. Res. **117**, A12307 (2012)
S. Xu, D. Mitchell, M. Liemohn, C. Dong, S. Bougher, M. Fillingim, R. Lillis, J. McFadden, C. Mazelle, J. Connerney, B. Jakosky, Deep nightside photoelectron observations by MAVEN SWEA: implications for Martian northern hemispheric magnetic topology and nightside ionosphere source. Geophys. Res. Lett. **43**, 8876–8884 (2016). https://doi.org/10.1002/2016GL070527
S. Xu, X. Fang, D.L. Mitchell, Y. Ma, J.G. Luhmann, G.A. DiBraccio, T. Weber, D. Brain, C. Mazelle, S.M. Curry, C.O. Lee, Investigation of Martian magnetic topology response to 2017 September ICME. Geophys. Res. Lett. **45**, 7337–7346 (2018). https://doi.org/10.1029/2018GL077708
S. Xu et al., Inverted V electron acceleration events concurring with localized auroral observations at Mars by MAVEN. Geophys. Res. Lett. **47**(9), e2020GL087414 (2020)
Ye. Yeroshenko, W. Riedler, K. Schwingenschuh, J.G. Luhmann, M. Ong, C.T. Russell, The magnetotail of Mars: Phobos observations. Geophys. Res. Lett. **GL017**, 885–888 (1990)
L.D.G. Young, A.T. Young, Interpretation of high-resolution spectra of Mars. IV. New calculations of the CO abundance. Icarus **30**, 75–79 (1977). https://doi.org/10.1016/0019-1035(77)90122-1
M.H.G. Zhang, J.G. Luhmann, A.J. Kliore, J. Kim, An observational study of the nightside ionosphere of Mars and Venus with radio occultation methods. J. Geophys. Res. **95**, 17,095–17,102 (1990). https://doi.org/10.1029/JA095iA10p17095
J. Zhao, F. Tian, Photochemical escape of oxygen from early Mars. Icarus **250**, 477–481 (2015). https://doi.org/10.1016/j.icarus.2014.12.032
R.W. Zurek, R.A. Tolson, S.W. Bougher, R.A. Lugo, D.T. Bairf, J.M. Bell, B.M. Jakosky, Mars thermosphere as seen in MAVEN accelerometer data. J. Geophys. Res. Space Phys. **122**(3), 3798–3814 (2017)